A FINITE ELEMENT STUDY OF THE MECHANICS OF MICRO-GROOVE MACHINING OF 4340 STEEL

BY

XIN CHEN

THESIS

Submitted in partial fulfillment of the requirements
for the degree of Master of Science in Mechanical Engineering
in the Graduate College of the
University of Illinois at Urbana-Champaign, 2015

Urbana, Illinois

Adviser:

Professor Shiv G. Kapoor

Abstract

Microgroove features have been widely used in hot embossing molds, micro-heat exchangers, optical lithography masks, micro-forming dies, engineered surface textures, etc. The challenge of achieving such feature is the control of the process parameters to minimize the side burr that often damages the microgroove. Besides, there is a limitation of the experimental study on gathering the cutting performance information such as temperature, stress, and chip formation for the purpose of process improvements. Therefore, a 3D Finite Element (FE) model was developed to study the microgroove cutting process. However, the frictional heat has not been considered in the previous FE models and could have big impact on predictions of the side burr height, chip thickness, temperature in the chip, and the cutting force experienced by the tool.

To better understand the process mechanics of micro-groove cutting, the 3D finite element model for microgroove machining of steel developed previously has been enhanced to include the friction heat generation. The side burr and chip formation were predicted and validated with experimental results in AISI 4340 steel, which showed that the model predicted side burr height within 6.7% and chip thickness within 3.3 % error. Various process mechanics including temperature distribution in the chip, cutting force predictions, and stress distribution in the workpiece were studied. It was found that coupling the thermal and mechanical effects, and including the friction heat improved the prediction of the cutting performance. It was also noticed that the cutting tool with a small edge radius and a larger rake angle experienced lower temperature, lower stresses, and smaller cutting forces on its rake face.

To Father and Mother

Acknowledgments

This research would not have been possible without the support of many people. I would like to express my sincere gratitude to my advisor, Professor Shiv G. Kapoor who helped make some sense of the confusion during my work and read my innumerable thesis revisions. Thanks to my parents Xiangyang Chen and Zhiqiong Li, and host parents Terry R. Fox and Karen W. Fox who have always been unconditionally supporting me to complete my dream. Finally, I would like to thank my friends, especially my best friend Madi Zholbaryssov who is a Phd candidate in the power group of ECE department for encouraging me to finish this work.

Table of Contents

List of Symbols

A	Yield strength coefficient
B	Strain hardening coefficient
C	Specific heat capacity
D	Strain rate coefficient
n	Strain hardening exponent
ε	Equivalent strain
$\dot{\varepsilon}$	Equivalent strain rate
$\dot{\varepsilon}_p$	Reference plastic strain rate
$\bar{\varepsilon}_D^{pl}$	Equivalent plastic strain
$\dot{\bar{\varepsilon}}^{pl}$	Equivalent plastic strain rate
$\bar{\sigma}$	Flow von mises stress
σ_m	Mean principle stress
$\sigma(t)$	Measured stress variable of time
$\hat{\theta}$	Dimensionless temperature
T	Current temperature
$\dot{T}$	Temperature change with respect to time
T_{melt}	Melting temperature
$T_{transition}$	Transition temperature

η	Stress triaxiality
ω_D	State variable
d_1-d_5	John-Cook damage material constants
Δt_{mesh} , $\Delta t_{thermal}$	Time estimation for mechanical and thermal effects
L_{min}	Dimension of the smallest element in the mesh
ρ	Density of material
ν	Possion ratio,
E	Modulus of elasticity
k	Thermal conductivity
t	Time
M^{NJ}	Lumped mass matrix
P^J	Applied load vector and
I^J	Internal force vector
F^J	Internal flux vector
u, $\dot{u}$, ü	Displacement, velocity, acceleration vectors,
N	Subscript, the degree of freedom
i	Subscript, increment number in an explicit dynamics step
τ_{fric}	Frictional shear stress

μ	Friction coefficient
F_c, F_f	Cutting force, feed force
f	Feed rate
P	Force resulting from localized phenomena close to the cutting edge
Q_N	Normal force
Q_T	Tangential force
Q_1	Frictional heat flux
Q_2	Contact heat flux
T_W	Workpiece contact temperature
T_T	Tool contact temperature
h	Heat transfer coefficient
T	Temperature
$\dot{q}_{(i)}{}'$	Ratio of the applied heat source and thermal conductivity
$\dot{f}_{(i)}$	Internal heat change
$\frac{\partial T}{\partial t}$	First partial differential of temperature with respect to time
$\frac{\partial^2 T}{\partial x^2}, \frac{\partial^2 T}{\partial y^2}, \frac{\partial^2 T}{\partial z^2}$	Second partial differential of temperature with respect to x, y, z

$\dot{q}_p$	Heat generation rate from plastic deformation
$\dot{q}_f$	Heat generation rate from friction
β	Inelastic heat fraction
A_o	Orignal cross sectional area of the bar
A	Cross sectional area after deformation
$\epsilon_T(t)$	Strain signal varible of time
J	Equivalent heat conversion factor
η_f	Fraction of dissipated heat due to friction
$\dot{\gamma}$	Shear strain rate
ε_C	Emissivity of workpiece
ε_T	Emissivity of tool
$\tau_{slide}, \tau_{stick}$	Frictional shear stresses in the sliding zone and sticking zone
$\tau_{fric-equi}$	Equivalent frictional shear stress
k_{chip}	Average shear flow stress
σ_n	Normal stress at tool-chip interface
l_p , l_c	Sticking region distance, and sliding region distance

α	Rake angle
G	End clearance angle
R	Tool edge radius
t_c	Cut chip thickness
∅	Shear plane angle
DC	Depth of cut

Chapter 1

Introduction

1.1 Background and Motivation

Micro-scale cutting process has become popular nowadays. The increasing need to create micro-scale features on micro-scale objects, micro-scale manipulations, etc. in many industrial and commercial sectors has been an important driver for change in the size of machines and cutting tools that are used to achieve these miniaturized features. One important micro-scale feature in product miniaturization technologies and which is also on high demand today is micro-grooves. The need of devices with micro-grooves comes from a diverse spectrum of fields such as micro-electronics, optics, automotive, photonics, thermal, bio-medical, etc [1]. For example, micro-groove features can be part of hot embossing molds, micro-forming dies, optical lithography masks, micro-fluidic devices, micro-optics, micro-heat exchangers, and engineered surface textures. Applications that in need of micro-groove cutting include long grooves with complex cross-sections and depths of a about a micron, high-density micro-heat exchangers that requires packed, long, high aspect ratio micro-grooves with widths that may be as small as a few hundred nanometers and with pitches less than a micron, and a series of intersecting curvilinear grooves with widths and depths of a few microns and that are used to build up complex surface patterns on metallic surfaces [2].

The micro-groove cutting process often becomes challenging because the features in the micro-scale are easily affected and even destroyed by the side burr formed after the cutting

process. Therefore, to have the ability to cut grooves in the size between a few hundred nanometers to a few microns wide, the ability to cut patterns of many grooves that are several millimeters long, and the ability to cut grooves with minimal burr formation/material distortion, the micro-groove cutting process needs to be studied in detail, especially the selection of process parameters that influence the machining performance. Even though the physical experiments can provide useful information about the machining performance of the micro-groove cutting process and the characteristics of the machined micro-grooves, there is a limit on how much information can be gathered from the experimental results on the underlying process mechanics for the purpose of process improvements. There are certain aspects of micro-groove cutting process such as chip formation, stress and temperature distribution, etc. that cannot be directly observed through empirical results. These factors can influence the outcome of the machined micro-grooves and the performance of the cutting tool tip. Therefore, it becomes crucial to study the micro-groove cutting through process modeling that can enhance the fundamental understanding and support in efficient process planning.

The types of machining models available for metal cutting modeling are analytical models, mechanistic models, and numerical models [2]. Analytical models are to describe the flow of material during cutting and the cutting forces generated using a series of specialized analytical expressions, which can vary significantly in complexity. Some researchers have approximated micro-groove cutting as an orthogonal cutting process and developed analytical models [61]. These models are generally limited to predicting surface generation under the cutting edge, while it is not able to provide the mechanisms at the side of an orthogonal cut or burr formation. These models also fail to provide information about the stresses and strains throughout the micro-cutting process [2]. Mechanistic models are suitable for easy computation

of cutting forces with means of a relationship between the cross-sectional area of a cut and the specific cutting energy of the material being cut. These models are capable of handling heterogeneous micro- structures. However, they do not provide detailed information about chip flow or the cutting and uncut surface of workpiece generated during machining [33].

For numerical models, there are three methods widely used for metal cutting process, which are molecular dynamic model (MD), finite difference method (FDM), and finite element method (FEM). MD model is able to explicitly model the interactions between substances from both the tool and workpiece during cutting. However, for cutting process involving volumes of workpiece material larger than a few thousand cubic nanometers, such models are computationally limited in the way that even with recent increases in computer power, workpiece sizes have been limited to rectangular volumes less than 20 nm on a side [34-36]. Therefore, even though these models are suitable for gaining insights into micro-scale effects, they are not quite suitable for predicting formation of micro-scale features. FDM employs inverse heat conduction to solve differential equation by approximating them with difference equations using Taylor series. It is widely used to predict the cutting temperature in machining by researchers [80, 81]. Because of the high temperatures usually involved in machining, not only the variations in material properties such as specific heat and thermal conductivity with temperature, but the softening effect resulted from high temperature induced may become significant. However, this factor has not been considered in FDM solutions [82]. FEM is able to represent the cutting processes in a way that is computationally feasible when cutting features with sizes of less than a micron and large. It can also provide detailed information of the cutting process, such as stresses, strains, temperatures, cutting forces, side burr formation, and chip formation of the workpiece [2]. Both 2D and 3D representation of the cutting process have been developed using FEM [5, 6,

10, 12, 18]. The 2D models have the plane strain approximation that allows them to predict chip formation and subsurface stresses provided that the width of the cut is much larger than the depth of cut. However, for micro-groove cutting process plain strain approximation is not adequate because the width of the cut grooves is 1.05-4.2 times the depth of cut [1, 2].

Bourne et al. [2], recently, developed a 3D model using FEA for micro-groove cutting process simulation to study the micro-groove cutting of a pure aluminum film coated on silicon using a rigid diamond tool tip with half symmetry and isotropic assumptions. The model is able to fairly accurately predict the side burr formation, exit burr formation and chip formation. It is also capable of simulating the cutting forces experienced by the tool, stress, and strain induced on the workpiece. However, the model developed by Bourne at al. did not include the heat generated during the micro-groove cutting process, which could have a significant impact on the stresses and cutting forces generated during machining [3, 6, 9, 12, 14, 13, 16]. Raghavendra [1] enhanced the 3D model of Bourne et al. [2] to study the micro-groove cutting of a steel workpiece using a rigid Cubic Boron Nitride (CBN) tool tip by including the plastic heat generated during the cutting process. However, the model did not include the heat generated by friction, especially, the heat generated due to sliding friction occur intensively at the tool-chip interface during the metal cutting process [11, 12, 17, 26, 55]. Moreover, owing to the friction, the large amount of energy generated heats up the secondary shear zone at the tool-chip interface. Due to the temperature-dependent elastic and elastic-plastic properties of the steel, the high temperature caused by friction is found to strongly influence the tool-chip contact length, the shear angle, and the cutting forces [18, 26].

1.2 Research Objectives, Scope, and Tasks

For the above reasons, the main objective of the research is to develop an enhanced FEA model that includes the heat generated by friction, and predict the machining performance in the steel micro-groove cutting process. Specific objectives of this research are:

(1) To gain an understanding of the thermo-mechanical aspect of micro-groove cutting that includes both inelastic and fictional heat generation;

(2) To validate the enhanced model by comparing the modeling results with the experimental results;

(3) To determine the appropriate cutting conditions such as, cutting speed, tool edge geometry, and tool rake angle in order to improve the machining performance of micro-groove cutting process.

In this study, a Cubic Boron Nitride (CBN) tool is used to machine micro-grooves in AISI 4340 steel. The grooves are a few micron wide, a few micron deep and between a few hundred microns to millimeters long and with high relative accuracy and depth consistency. The simulation trials are limited to studying the underlying cutting mechanics at the tool-chip interface of the workpiece. The tool is considered rigid. In addition, half-symmetry of the model is used. The material of the workpiece is considered homogeneous. Lastly, the heat transfer between the tool and workpiece is assumed to be an adiabatic process.

To achieve these objectives, the following tasks will be carried out.

(1) Study the fully coupled thermo-stress model of micro-groove cutting that includes both inelastic and frictional heat generation;

(2) Gain an understanding of the friction model at the tool-chip interface for modeling the

frictional heat;

(3) Include the frictional heat into the model by utilizing the frictional heat equation and determining the inelastic and frictional heat fractions, and frictional equivalent heat conversion factor for the tool-chip interface of micro-groove cutting;

(4) Define the contacting surfaces between the tool and the workpiece;

(5) Design suitable simulation experiments and run the simulations with enhanced model;

(6) Generate side burr formation, chip thickness, temperature, stress, cutting force data for the steady-state micro-groove cutting process using the enhanced model;

(7) Validate the model by comparing the burr formation and chip thickness data from the enhanced model with the cross-sectional 2D AFM plot and SEM images of the chip roots;

(8) Justify the importance of coupling thermal effect with mechanical effect for micro-groove cutting FE model by comparing temperature and cutting force results of coupled model with uncoupled model;

(9) Study the effect of friction heat on the temperature and cutting force results by comparing modeling outcomes obtained from friction heat enabled model with ones from friction heat disabled model;

(10) Study the effects of tool edge geometry and tool rake angle on the micro-groove cutting performance in terms of cutting force, von mises stress, and temperature;

(11) Select the appropriate tool edge geometry and tool rake angle to improve the machining performance of the micro-groove cutting process.

1.3 Thesis Overview

The organization of the thesis is as follows. Chapter 2 reviews the 3D modeling steps and approaches developed and used by Bourne [2] and Raghavendra [1] for their modeling such as 3D modeling assumption, half symmetry assumption, isotropic assumption, explicit integration scheme, Lagrangian/Adaptive Lagrangian Eulerian formulations, mesh element type selection, Johnson-Cook constitutive material flow stress model remeshing technique, sliding friction contact algorithm, adiabatic heat assumption, and plastic heat generation.

Chapter 3 discusses the enhancements made to the 3D FEA model developed by Raghavendra [1] in order to comprehensively study the heat generated in the micro-groove cutting process in steel. It begins with discribing the contact algorithm and fully coupled thermal-stress integration rule. The parameters that dominate the plastic heat and frictional heat generation are discussed next. Lastly, the required workpiece and tool properties are described in this chapter as well.

Chapter 4 talks about the results of the simulations that are analyzed and compared with experimental results for validation. Besides, the influence of cutting edge geometry, cutting speed and tool rake angle conditions on the outcome of the process mechanics is described including chip formation and development, cutting force predictions, stress and strain distribution, and tool-chip temperature gradients.

Chapter 5 provides a brief summary of the work described in this thesis and gives conclusions that are based on the work accomplished. The recommended areas of future work are briefly discussed to further develop the more advanced 3D modeling simulation.

Chapter 2

Literature Review

2.1 Introduction

This chapter provides an in-depth knowledge and reviews the existing literature available on micro-groove cutting, including micro-groove cutting process and numerical modeling and implementation approaches. Both 2D and 3D modeling in terms of flow stress and chip separation modes as well as remeshing formulation for 3D model implementation are summarized. Finally, a review of heat generation in metal cutting is also given.

2.2 Micro-groove Cutting Process

To form micro-grooves with less than 50 μm, which requires formation of extremely narrow and shallow curvilinear features, a new micro-groove cutting process, which is a low-speed, orthogonal cutting process has recently been developed [1, 2]. The micro-groove cutting is accomplished by dragging the tool tip on top of the workpiece. The flexible cutting tool used depends on the material of the workpiece where the groove is formed. For instance, for cutting 1018 low-carbon steel, CBN is used which is bonded to AFM sapphire cantilever, commercially available as shown in Fig. 2.1. More specifically, the sapphire beam with its high modulus is bonded to a sapphire substrate and the single CBN crystal is adhesively glued to the tip of the cantilever. Since applying cutting loads beyond the failure load would result in catastrophic

failure of the AFM sapphire cantilever, it is critical to maintain the applied cutting load at the tool tip within the failure values.

The process is able to (a) cut grooves in metals that are between a few hundred nanometers wide and a few microns wide, (b) cut patterns of many grooves that are each several millimeters long, (c) cut patterns of curvilinear grooves, (d) cut grooves with nearly arbitrary cross-sections, (e) cut grooves with minimal burr formation / material distortion, have good material removal rate, (f) cut fully-programmable patterns of grooves, (g) fabricate micro-grooves using relatively inexpensive equipment, (f) achieve relative tolerances of approximately 1% or better, and (g) cut grooves in flat or curved workpiece surfaces [2].

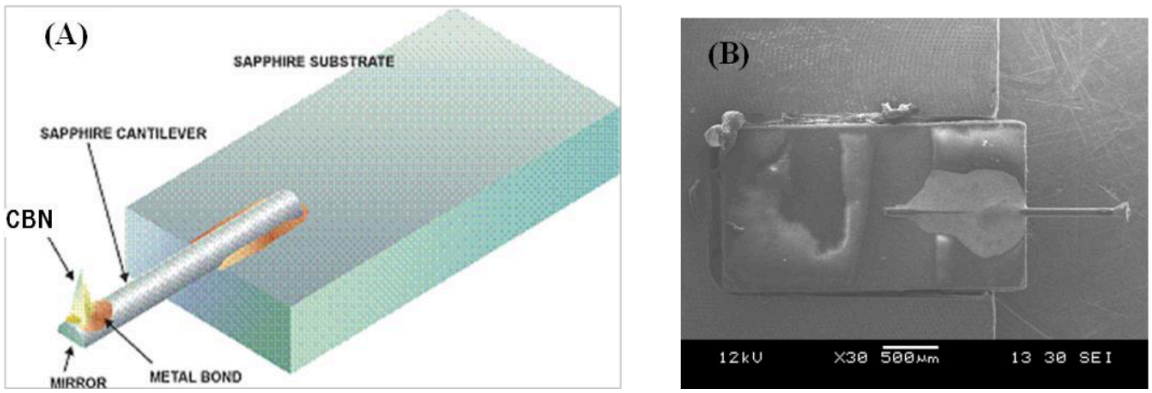

Fig. 2.1 AFM-sapphire Cantilever – (A) Schematic and (B) SEM image

Since micro-groove cutting process becomes challenging due to small features that can be destroyed by the side burr formed during the process, a better understanding of the mechanics of the cutting process and chip characteristics is required. The microgroove cutting is a complex process and to study the mechanics of cutting process through experiments is quite challenging. Researches have recently used process modeling to gain a better understanding of cutting process mechanics. Both analytical and numerical modeling approaches have been developed and

process characteristics such as side burr, chip morphology, etc have been studied.

2.3 Numerical Modeling Approach

The finite element method (FEM) based numerical model is the most suitable modeling approach for micro-groove cutting. In FEM modeling, the system geometry is represented as a set of elements, consisting of nodes with a finite number of degrees of freedom. These nodes form a grid called mesh. Certain material and structural properties are assigned to the mesh, which define how the structure will react to certain loading conditions. The FE method can also be used to modify an existing product or structure as well, so as to qualify the product or structure for a new service condition [29].

Finite element models have been used to study many cutting processes both at micro-scale and the macro-scale. For orthogonal cutting process, the FE models have been used to study the influence of changing the cutting speed, rake angle, and coefficient of friction on process characteristics such as shear angle, chip thickness, strain, strain rate, stress, temperature, chip burr, tool-chip contact length, and cutting force [18, 37, 38]. Researchers have also used finite element modeling to study fundamental aspects of the cutting process, such as the effect of using tools with large edge radii relative to the depth of cut [39, 40], size effect at the micro-scale by addressing the contributions of the decrease in cutting temperature in the secondary shear zone seen at the micro-scale and the presence of strain gradient hardening [39, 41], effect of tool-chip heat partition coefficient on temperature of the tool and chip [12], effect of rake angle on the cutting mechanism outcome results [14], and the effect of cutting through a workpiece with a heterogeneous micro-structure [42-44]. Finite element modeling has also been used to study

insights into the actual method of separation between a chip and workpiece during machining for example, ductile fracture ahead of the cutting edge of a tool [35, 40]. These models have been used to examine characteristics of chip formation and chip flow, for example segmented chip formation and chip breaking [45]. Finite element models have been used to examine finished workpiece characteristics in a way these characteristics are altered by modifying the cutting process, for example, residual stresses in the workpiece that affects part quality and deformation [39, 46]. The models have been used extensively to study side burr formation for orthogonal metal cutting [2], drilling [47, 48], and face milling [49].

There are different types of FEM tools available in industry. One is AdvantEdge FEM produced by Third Wave Systems, inc, [50, 30]. Another industrial software package is DEFORM produced by Scientific Forming Technologies Corporation. They both can handle 2D and 3D machining simulation; even though DEFORM is mainly developed for forming operations [51]. These software packages are used to perform calculation of cutting forces and torques, determine ways of increasing material removal rates, improve tool life, predict chip shape, shorten product design cycles, and reduce trial and error during manufacturing process experimental setup [50]. Cutting processes including milling, turning, broaching, sawing, drilling, boring, tapping, and groove cutting can be studied by using these tools [50].

Since metal cutting process is an inherently nonlinear dynamic process, the finite element solution methods suitable for such systems must be employed. Abaqus FEA has been popular to study metal cutting processes. It is capable of providing information such as stress, strain, temperature, chip formation, and side burr formation of micro-groove cutting mechanism. More importantly, in order to analyze the energy consumed in material separation leading to chip formation, the software that makes use of a fully-coupled thermo-mechanical finite element

model incorporating a predefined separation layer of elements and that will fail based on a ductile fracture criterion leading to chip formation is needed [6].

Two solution methods of Abaqus are used. These are referred to as implicit dynamic analysis and explicit dynamic analysis [16]. The implicit method is able to handle dynamic quantities during a current time increment based on values from a previous time increment and at the current time increment. Hence implicit, nonlinear equations must be solved at each time step, typically via some iterative solution method [16], which has been used by a few researchers for orthogonal cutting modeling [3, 18, 41]. However, implicit dynamic method has difficulty handing complex contact conditions, complex boundary conditions, and material failure. This problem can become challenging when it tries to achieve solution convergence and limit modeling options. However, many researchers used explicit dynamic analysis to model the metal cutting processes [4, 6, 7, 8, 9, 13, 47, 48, 50, 59, 60]. The explicit dynamics procedure calculates dynamic quantities during a current time step using only quantities already calculated in a previous time step using central-difference time integration rule [16]. This method is able to solve complex contact conditions, complex boundary conditions, large deformations, and material failure. But this method uses many very small time increments in order to insure a stable solution, which consumes extra computational time.

More specifically, since the Explicit dynamics procedure calculates results over a large number of small time increments using central-difference time integration rule, even a small change in the state of each element in the simulation is computed based on the beginning state of the elements under any load / boundary conditions applied during the every time increment [2]. Thus, this procedure is suitable for analysis of quick dynamic procedure with complex contact conditions under large deformations. At the same time, it does not have difficulty in converging

solutions, which might happen using direct-integration.

2.3.1 2D Model

Many researchers [11, 12, 18, 17, 40, 47 52, 53] have treated the process as 2D via the plane strain approximation, which allows for observations of chip formation and subsurface stresses provided that the width of the cut is much greater than the depth of cut. But it is only valid given that the width of the cut is much greater than the depth of cut [1-4]. Besides, this model assumes that all strain tensor components orientated out of the cutting plane are too small to be considered. An example of a typical 2D finite element model is shown in Fig. 2.2.

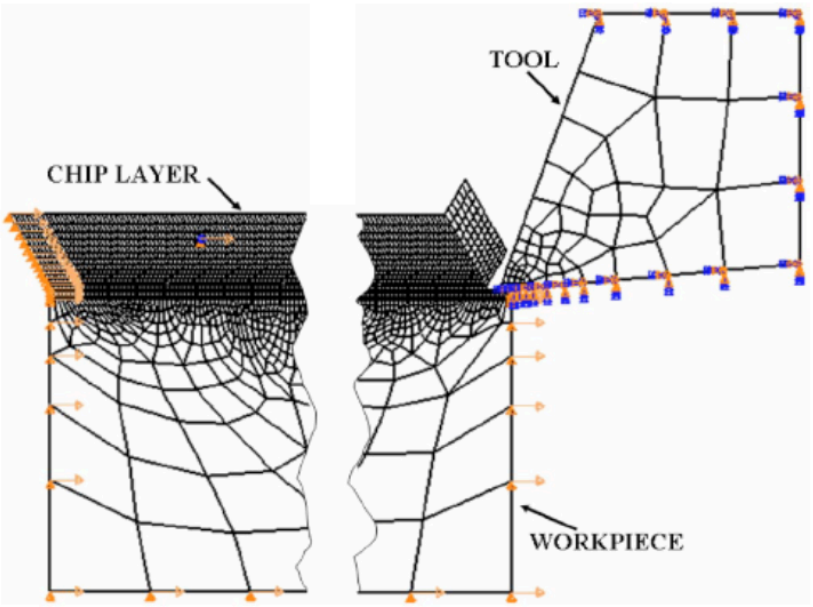

Fig. 2.2 Example of a typical 2D finite element model of orthogonal cutting [40]

Johnson-Cook Constitutive Material Flow Stress

The material flow stress is referred to instantaneous yield stress under loading. And it is related to strain, strain rate, temperature and microstructural effects of the material. The constitutive flow model for simulating the material cutting problem needs to able to accurately describe material behavior when it undergoes large strains, high strain rates, and high temperatures. According to Akbar [12] Johnson-Cook constitutive material flow stress model is the most convenient material model that also produces excellent results describing the material behavior and chip formation. Also it has been successfully used in high-speed machining region, and frequently used thermo-visco-plastic material model suitable for problems where strain rates vary over large range, and temperature changes, due to plastic deformation caused by thermal softening for steel [11, 13, 20, 21]. Johnson-Cook constitutive material flow stress model describes a particular type of Von Mises plasticity and the flow stress data during the simulations are obtained mainly using four methods such as high-speed compression tests, Split-Hopkinson's bar tests, practical machining tests and inverse analysis. The equation for the flow stress $\bar{\sigma}$ is given as,

$$\bar{\sigma} = [\mathrm{A} + \mathrm{B}\ (\varepsilon)^n]\ [1 + \mathrm{D}\ \ln(\frac{\dot{\varepsilon}}{\dot{\varepsilon}_p})]\ [1 - (\hat{\theta})^m], \tag{2.1 a}$$

$$\hat{\theta} = \begin{cases} 0 & for\ T < T_{transition} \\ \frac{T - T_{transition}}{T_{melt} - T_{transition}} & for\ T_{transition} \leq T \leq T_{melt} \\ 1 & for\ T > T_{melt} \end{cases} \tag{2.1 b}$$

where A is the yield strength, B is the strain hardening coefficient, n is the strain hardening exponent, ε is the equivalent plastic strain, D is the strain rate coefficient, $\dot{\varepsilon}$ is the equivalent plastic strain rate, $\dot{\varepsilon p}$ is the reference plastic strain rate, T is the current temperature, $T_{transition}$ is

the transition temperature when softening effect starts to affect the material property, and T_{melt} is the melting temperature.

Johnson-Cook Chip Separation Criteria

There are two commonly used criteria, a geometrical criterion and an equivalent plastic strain criterion, to separate the chip from the machined surface in finite element analysis. Some researchers have adopted the former separation criterion [22, 63]. The geometric criterion is convenient to use, but its physical meaning is not well established. Therefore, an equivalent plastic strain criterion is adopted in most of studies [17, 40, 47 52]. This has become popular and effective in modeling chip separation of metal cutting [11, 62, 64].

The failure at the chip entry step is achieved based on a ductile criterion condition. The formulation states that the equivalent plastic strain, denoted as $\bar{\varepsilon}_D^{pl}$, at the onset of damage is a function of stress triaxiality denoted as η, and the equivalent plastic strain rate denoted as $\dot{\bar{\varepsilon}}^{pl}$, given by following equation,

$$\bar{\varepsilon}_D^{pl} = f\left(\eta, \dot{\bar{\varepsilon}}^{pl}\right) \tag{2.2}$$

$$\eta = \frac{\sigma_m}{\bar{\sigma}}, \tag{2.3}$$

and η is a function of mean principle stress σ_m, and the Von Mises equivalent stress, denoted as $\bar{\sigma}$.

Stress triaxiality is an important factor in ductile crack formation [24]. As a matter of fact the equivalent plastic strain decreases when stress triaxiality increases [24, 25]. Stress triaxiality equaling to -1/3 was determined for steel [25]. However, the Johnson-Cook (JC) damage model

used in micro-groove cutting modeling does not follow this criterion. Therefore, user-defined values of equivalent plastic strain for fracture in the cut-off range of stress triaxiality for AISI 4340 can be found in Ng [21]. The damage evolution at the start of chip propagation is reflected from the values extracted from Fig. 2.3, where equivalent fracture strain at different strain rates (ER) and temperatures (C) for AISI 4340 can be found for the different stress triaxiality values.

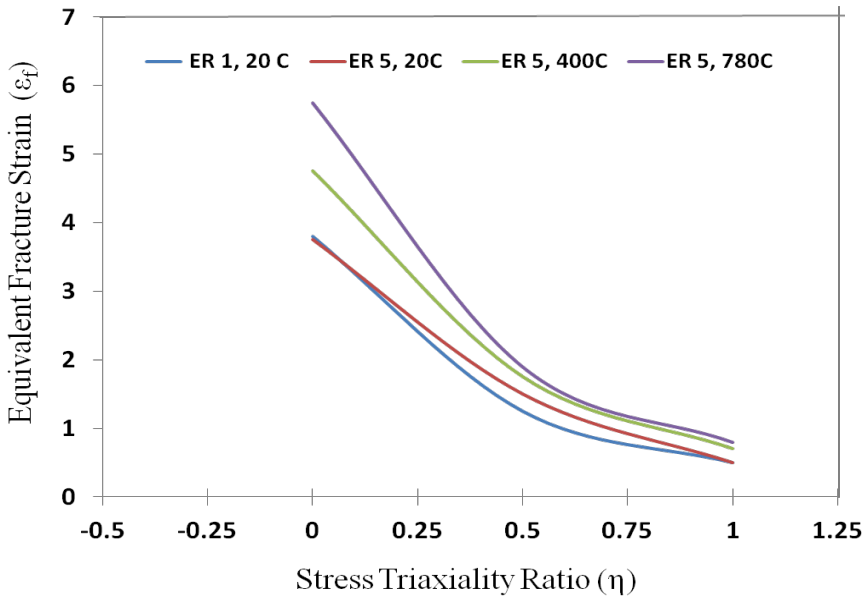

Fig. 2.3: Fracture strain variation for AISI 4340 for different stress triaxiality ratios

For the separation criteria, Crack propagation is achieved when shear fracture mechanism fails depending on a damage parameter evaluated at an integration point and the criterion for damage initiation is met, using following equation,

$$\omega_D = \int \frac{d\bar{\varepsilon}^{pl}}{\bar{\varepsilon}_D^{pl}\left(\eta, \dot{\bar{\varepsilon}}^{pl}\right)} = 1 \qquad (2.4)$$

where ω_D is a state variable. At each increment during the analysis the incremental increase in ω_D is great or equal to zero.

The value of $\bar{\varepsilon}_D^{pl}$ during each step is derived using the Johnson–Cook (JC) damage model, given by Eq. (2.5) [20],

$$\bar{\varepsilon}_D^{pl}\left(\eta,\dot{\bar{\varepsilon}}\right)=\left[d_1+d_2e^{\left(-d_3\eta\right)}\right]\left[1+d_4\ln\left(\frac{\dot{\bar{\varepsilon}}^{pl}}{\dot{\varepsilon}_0}\right)\right]\left(1+d_5\hat{\theta}\right), \quad (2.5)$$

where d_1-d_5 are material constants, η is the stress triaxiality, $\hat{\theta}$ is a dimensionalless temperature value defined in Eq. 2.6,

$$\hat{\theta}=\begin{cases}0 & for\ T<T_{transition}\\ \frac{T-T_{transition}}{T_{melt}-T_{transition}} & for\ T_{transition}\le T\le T_{melt},\\ 1 & for\ T>T_{melt}\end{cases} \quad (2.6)$$

where T is the current temperature, $T_{transition}$ is the transition temperature equal or below the temperature when there is no temperature dependence on the expression of the damage strain $\bar{\varepsilon}_D^{pl}$. , and T_{melt} is the melting temperature. Both Bourne [2] and Raghavendra [1] adopted the equivalent plastic strain criterion into their micro-groove cutting models.

2.3.2 3D Model

2D plain strain assumption is invalid when the width of the cut is smaller than the depth of the cut. In the micro-groove cutting process discussed in this research, a tool as wide as 1.05 μm is used to cut grooves as deep as approximately 0.25 to 1.0 μm under orthogonal cutting [5]. Therefore, the width of the grooves is about 1.05 - 4.2 times as large as the depth of the cut, invalidating the plane strain assumption. Furthermore, it is desired that 3D stress-strain fields

need to be considered in the micro-groove cutting process and the model is able to capture the 3D mechanism such as chip separation during the micro-groove cutting process. Moreover, the side burrs that need to be evaluated in the simulation can only be observed using a 3D image [1, 2]. And since 3D stress and strain fields are involved in this micro-groove cutting process, they can only be studied through a 3D model. Also, the work material mode should account for the elastic-plastic and thermal behavior of the material performance, which complies with the complexities of actual micro-groove cutting process.

For the micro-groove cutting mechanism, the temperature-dependent properties of the workpiece material, and associated heat generation and partition scheme need to be inducted into the 3D model [1]. Hence, a coupled adiabatic heating condition is considered for observing the thermal results from the model. The heat induced by friction and plastic deformation diffuses quick enough that the tool and workpiece are independent during the heat transfer process and the adiabatic assumption will be used in this modeling simulation. In order to implement the coupled thermo-mechanical method, Raghavendra [1] and Keith [2] both used 3D modeling method in their simulations.

Model Assumption

Raghavendra [1] and Bourne [2] used symmetry boundary condition in their micro-groove cutting 3D modeling. The model consists of 6 parts including tool, cut part, uncut part, and three support parts. The workpiece is modeled by assembling five different subparts, as shown in Fig. 2.4. Each component is meshed with different mesh side and assigned with contact algorithm. Moreover, the entire process is broken down into five time steps for characterizing the different boundary conditions, such as initial step, cut entry step, cut established step, cut exit

step and cut clear step, corresponding to establishment of initial conditions, initial entry of the tool into the workpiece, steady state cutting, exit of the tool from the workpiece, and moving the tool past the workpiece, respectively. The summary of the steps breakdown and boundary conditions is given below,

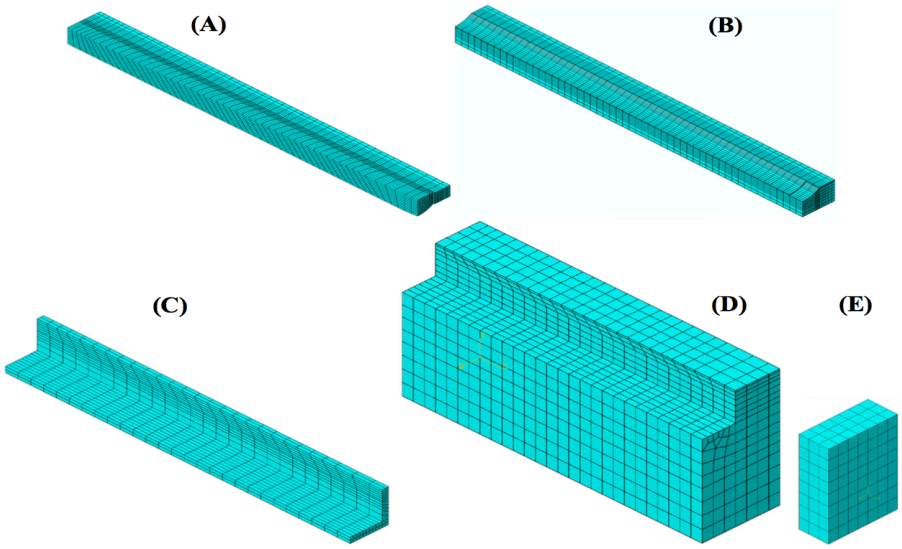

Fig. 2.4 Workpieces subcomponents, (A) cut-part; (B) uncut-part; (C) support part 1; (D) support part 2; (E) support part 3 [2]

Table. 2.1 Time steps and corresponding boundary conditions [2]

Time Step	Initial	Cut Entry	Cut Est.	Cut Exit	Cut Clear
Duration (msec)	0.0	0.242	1.32	0.6	0.25
Fixed X Entry B.C.	Nodes fixed in x-dir				
Fixed Z Crack B.C.	Nodes fixed in z-dir		Inactive		
Pinned Sides B.C.	Nodes fixed in all directions				
Pinned End B.C.	Nodes fixed in all directions				
Pinned Exit B.C. 1	Nodes fixed in all directions			Inactive	
Pinned Exit B.C. 2	Nodes fixed in all directions			Inactive	
Symmetry B.C.	Symmetry about xy-plane				
Tool Vel B.C.	Inactive	-5 mm/sec in x-dir			
Chip Guide Vel B.C.	Inactive	-5 mm/sec in x-dir		Inactive	

Due to the complex breakdown of the workpiece and steps, large computational time is needed for the software to execute the simulation. Thus, in order to get the simulation more efficient and reduce the computational time, a boundary condition/assumption of half-symmetry is employed throughout the steps as indicated in the Table 2.1. With this precudure the worpiece and tool are modeled with only half of the targeted side and consequently symmetry boundary condition to the parts are applied, as shown in the Fig. 2.5.

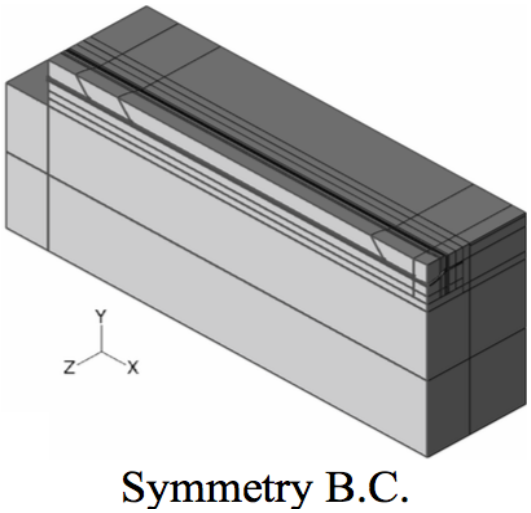

Fig. 2.5 Workpiece symmetry boundary condition [2]

Raghavendra used isotropic assumption for micro-groove cutting model [1]. According to Raghavendra [1], the microstructure of AISI 4340 has the martensitic grain structure on the ferrite matrix post its heat treatment, as shown in the Fig. 2.6. First of all, the average grain size is measured to be approximately 20 μm, which is greater than the length of cut 10 μm performed in the 3D FEA simulation. Thus, the assumption that the material of the plastically deformable workpiece is isotropic and homogenous for this simulation is reasonable. In other words, micro-structural effects of steel are neglected.

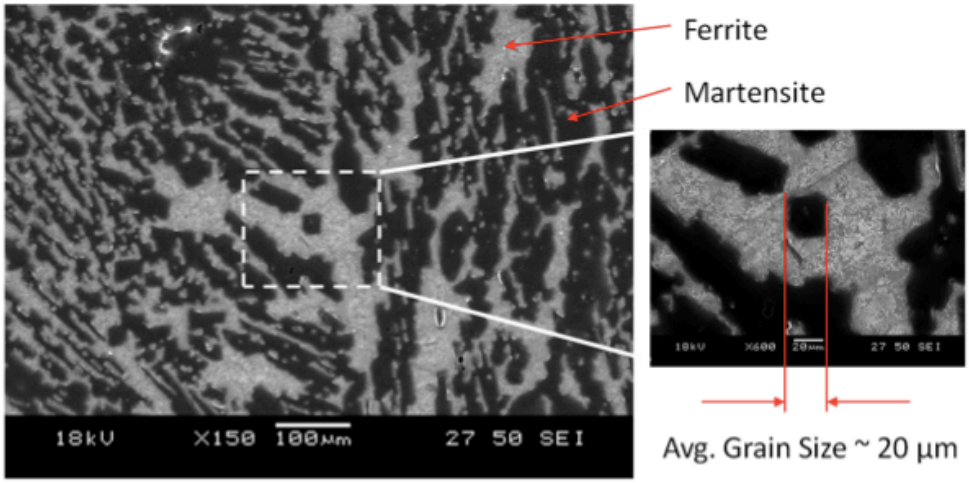

Fig. 2.6 Grain structure of AISI 4340 steel [1]

Element Remeshing Formulation

There are three different FEA remeshing formulations frequently used for modeling cutting process, which are the Lagrangian, the Eulerian, or the adaptive Lagrangian-Eulerian (ALE). When Eulerian formulation is being used, material flows into and out of the elements rather than having configuration of the finite element mesh change. According to Abaqus manual [16], an Eulerian mesh domain is used to model material flowing through the mesh and typically has two Eulerian boundary regions, one inflow and one outflow, connected by Lagrangian and/or sliding boundary regions. The correct combination of mesh constraints and material boundary conditions applied to an Eulerain boundary region depends on whether the region acts as an inflow or an outflow boundary. The region types and mesh constraints assigned to the boundary regions that are connected to the Eulerian boundary regions must be chosen to simulate the correct physical behavior as well. This formulation is particularly suitable for modeling steady-state machining using a small number of elements [2].

For micro-groove cutting process discussed here, prior knowledge about the shape of the chip must be acquired from some other source in order to properly select the mesh shape. Transient events such as exit burr formation also cannot be handled by this method [10]. When using the Lagrangian formulation, elements that make up the finite element mesh corresponding to a piece of material never leave the element. In other words, deformation of the workpiece mesh is based on the deformation of the underlying material. This formulation can be used to simulate transient dynamic events such as the entrance of a tool into a workpiece, chip formation, and exit of a tool from a workpiece. However, care has to be taken to avoid excessively distorted elements. Many researchers have used this formulation when modeling metal cutting [3, 6, 7, 9, 18, 37, 41].

The ALE formulation is a hybrid of the Lagrangian and Eulerian formulations. It combines the features of pure Lagrangian analysis and pure Eulerian analysis. This type of adaptive meshing is often referred to as ALE analysis [16]. It is a tool that makes it possible to maintain a high-quality mesh throughout an analysis, even when large deformation or loss of material occurs, by allowing the mesh to move independently of the material. The ALE adaptive meshing does not alter the topology such as elements and connectivity, of the mesh, which implies some limitations on the ability of this method to maintain a high-quality mesh upon extreme deformation. The ALE adaptive is intended to model large-deformation problems. It does not attempt to minimize discretization errors in small-deformation analyses. There are a few beneficial features in ALE. It can often maintain a high-quality mesh under severe material deformation by allowing the mesh to move independently of the underlying materials and maintain a topologically similar mesh throughout the analysis. It can be used as a continuous adaptive meshing tool for transient analysis problems undergoing large deformations such as

dynamic impact, penetration, and forging problems. It can also be used as a solution technique to model steady-state process and as a tool to analyze the transient phase in a steady-state process. More importantly, it is suitable for explicit dynamics such as adiabatic thermal analysis and fully coupled thermal-stress procedures. The ALE remeshing technique for a pure Lagrangian method is shown in Fig. 2.7, which does not change the elements and connectivity of the constructed mesh geometry. Lastly, a kinematic penalty contact scheme is used for remeshing when the cutting step is established along with default frequency and remeshing sweeps per increment.

The Abaqus software uses an adaptive algorithm to determine the incremental scheme and is fully automatic. A mass-scaling factor is used for getting reasonable number of time increments in order to observe the micro-groove cutting simulation process. Raghavendra used 500 as the mass-scaling factor in his model. The exact estimate of suitable time increments that fits into the 3D FEA model can be found in [2].

Due to the fact that the process is a dynamics event and produces large deformations within small time increments, it can encounter massive mesh distortion during the cutting modeling simulation. Thus, it is necessary to choose a suitable remeshing procedure to maintain the stability of the mesh throughout the simulation. An Arbitrary adaptive Lagrangian–Eulerian (ALE) remeshing technique with pure Lagrangian formulation is implemented by Raghavendra [1] because it is capable of dealing with the mesh distortion and maintaining the mesh topology due to large distortion during the simulation. However, the 3D model developed by Bourne et al. used the Lagrangian-based formulation for process mechanics of micro-groove cutting process since thermal effects are ignored in his analysis.

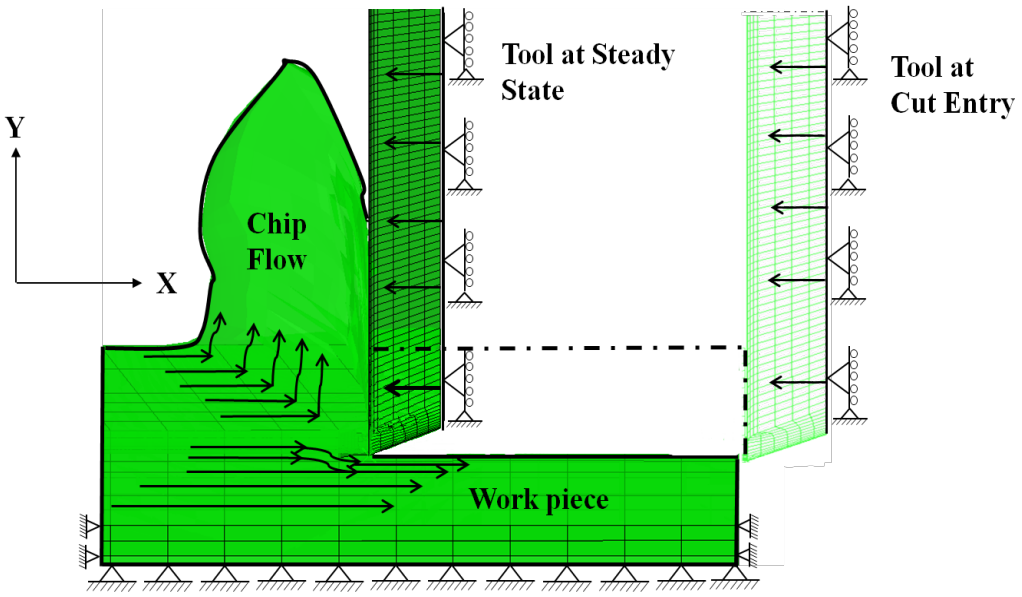

Figure 2.7: Finite element model formulation

Both 2D and 3D [1, 2, 12, 54] modeling approaches are commonly used for metal cutting models. The 2D approach, also called plain strain approach is a simpler method that saves time and work in the modeling. However, the most relevant criticisms involve material characterization for strain, strain rate, material hardness (in the case of hard turning) and temperature conditions typical of machining, friction data at the tool/part interface, chip formation and heat transfer conditions [54].

2.3.3 Model Implementation

This subsection provides insight of 3D model implementation such as explicit integration scheme, element selection, contact algorithm, micro-groove cutting model geometry.

Explicit Integration Scheme

Using the general purpose Abaqus finite element software, solutions can be acquired

through an implicit dynamic analysis procedure (Abaqus/Standard) or through an explicit dynamics procedure (Abaqus/Explicit). The explicit dynamics procedure evaluates a large number of small time increments where a central-difference time integration rule is used. During each increment a tiny change in the state of each element in the model is calculated based on the state of the elements at the start of the increment and any load / boundary conditions applied during the increment. This procedure is suitable for analysis of short dynamic events, complex contact conditions, large deformations, and does not suffer from convergence problems that can arise when using direct-integration. Abaqus/Explicit was selected for use in Micro-groove cutting model by Bourne [2].

The explicit dynamics procedure requires the time for a signal e.g. stress wave that propagate through any element in the mesh to be less than the time increment used, otherwise the model will be unstable and result in error. This requirement can result in the need for dividing the time into very tiny time increments, which can render simulations computationally infeasible for short periods of time. Therefore, it is desirable to use as large of a time increment as possible, which will not cause the model to become unstable [2].

An estimate of the largest stable time increment imposed by the purely mechanical response of a model is given by Equations (2.7) – (2.10),

$$\Delta t_{mesh} \approx \frac{L_{min}}{C_d}, \tag{2.7}$$

where Δt_{mech} is the time estimate, L_{min} is the dimension of the smallest element in the mesh, and C_d is given as following,

$$C_d = \sqrt{\frac{\tilde{\lambda}+2\tilde{\mu}}{\rho}}, \tag{2.8}$$

where ρ is the density of material, $\tilde{\lambda}$ and $\tilde{\mu}$ are provided below,

$$\tilde{\lambda} = \frac{E\,\nu}{(1+\nu)(1-2\nu)} \tag{2.9}$$

$$\tilde{\mu} = \frac{E}{2(1+\nu)}, \tag{2.10}$$

where ν is passion ratio, E is the modulus of elasticity [16]. When thermal effects play roles in the analysis, the following equation is used,

$$\Delta t_{\text{thermal}} \approx \frac{{L_{min}}^2}{2\alpha}, \tag{2.11}$$

where $\Delta t_{\text{thermal}}$ is the time estimated for thermal effect, and α is given as,

$$\alpha = \frac{k}{\rho C}, \tag{2.12}$$

where k is the thermal conductivity, and C is the specific heat [16].

It has been referred in [1] that the implicit model may have problem of converging due to the modeling complexities. The Explicit analysis provides better physical comprehension of the chip formation and a more accurate representation of the complexity of the domain boundaries and material failure [2]. More specifically, the Explicit dynamics procedure has the capability of evaluating a large number of small time increments using a central-difference time integration rule and lumped element mass matrices that calculates displacement and velocities based on the quantities at the beginning of an increment [19]. The equations governing the motion of the body are integrated using the following equations:

$$\ddot{u}_i^N = (M^{NJ})\left(P_i^J - I_i^J\right) \tag{2.13}$$

$$\dot{u}^N_{(i+1/2)} = \dot{u}^N_{(i-1/2)} + \frac{\Delta t_{(i+1)} + \Delta t_{(i)}}{2} \ddot{u}^N_{(i),} \tag{2.14}$$

$$u^N_{(i+1)} = u^N_{(i)} + \Delta t_{(i+1)} . u^N_{(i-1/2)} , \tag{2.15}$$

where time t is used to advance the velocity solution to time t + Δt/2 and the displacement solution to time t + Δt/2, M^{NJ} is the lumped mass matrix, P^J is the applied load vector and I^J is the internal force vector, u, $\dot{u}$ and ü are the displacement, velocity, and acceleration vectors, u^N is the degree of freedom, either a displacement or rotational component and the subscript i refers to the increment number in an explicit dynamics step. The central difference integration is explicit so that the kinematic state may be advanced by known values of $\dot{u}^{(i-½)}$ and $\ddot{u}^{(i)}$ from the previous increment.

Element Selection & Modeling Scheme

There are many types of elements used for simulating the metal cutting process. Plain strain elements (CPE4RT) were used by Subbiah [6] to model the workpiece and the tool. These are four-noded quadrilateral elements with reduced integration and hourglass control. Mabrouki, Kishawy, Akbar and Sulaiman [11, 52, 12, 53] also used this element type for the workpiece to account for the coupled-temperature-displacement calculation, but two node rigid elements (R2D2) for the tool. But this type of selection is suitable for plain strain elements. Llanos used reduced integration and hourglass control eight-node hexahedric elements with trilinear displacement and temperature calculation (C3D8RT) [13]. Akbar used a four-node tetrahedral heat transfer element DC3D4 available in Abaqus Standard [26]. According to Umbrello, the workpiece was initially meshed by means of 2500 iso-parametric quadrilateral elements while

the tool is modeled as rigid available in SFTC-Deform-2D 9.0 [54]. The workpiece material used by Raghavendra for the experimental work consisted of a 3.1 μm thick film of thermally evaporated aluminum deposited on a flat silicon substrate. The thermal softening during machining is not very significant for the micro-scale [1]. An eight-node linear hexahedric element (C3D8R) with "relax stiffness" hourglass treatment and reduced integration is used for modeling the workpiece in order to observe the adiabatic heating effects and study the large deformations during the cutting process. But the tool is modeled using a 3D rigid (R3D4) non-deformable element, since the tool is much harder than the workpiece and the material properties of tool during the cutting process is not used in this study.

Thermal softening and stress-triaxiality effects were not considered due to the high thermal conductivity of the steel (workpiece), small uncut chip thickness and low cutting speeds in the cutting process, which is also used by Kopalinsky [15]. In the simulation, the tool was modeled with rigid 3D planar elements (R3D4) with 0 ° rake angle, a 20° end clearance angle, a 5° side clearance angle, and a perfectly sharp cutting edge [1]. The tool is assumed to be perfectly rigid and experienced no deformations during the cutting process since CBN is much stronger and harder than steel. In order to increase the material density of simulation and reduce the large number of time increments during simulation, a mass-scaling factor of 5000 was used. The overall model geometry for workpiece and tool is developed on half-symmetry to save computational time [1, 2]. The overall mesh, the rigid tool surface mesh and the initial crack with an opening angle are shown in Fig. 2.8. The initial crack is used to initiate the chip formation.

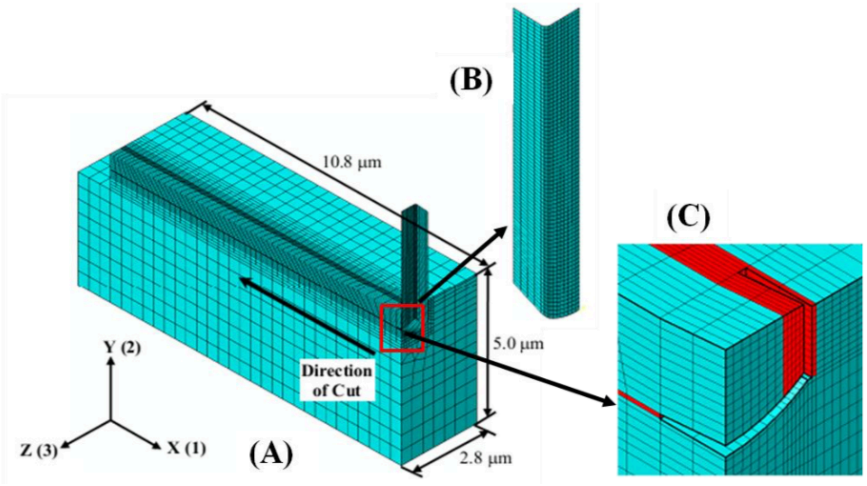

Fig. 2.8 (A) Overall Mesh Geometry of 3D Model, (B) Tool surface, (C) Crack Initiation for chip formation [2]

Contact algorithm & Frictional Parameters Attainment

In machining, the interaction between the cutting tool and the chip is a complex contact problem. The contact phenomena can be characterized by sticking and sliding [12, 26]. The iterations between the tool and the chip were analyzed by considering contact behavior, which transmits normal and frictional stresses to the interfacial region [12]. In the sliding region, the contact pressure is low and the relative motion occurs between the tool and the cut workpiece, and the predicted frictional shear stress τ_{fric}, is below a set limit, τ_{crit} estimated as the ratio of the measured feed force (when rake angle is equal to zero) to the seized area of the contact on the tool rake face [12, 26]. In the sticking region, there is high contact pressure on the rake face of the tool tip as shown in Fig. 2.9 and predicted frictional shear stress exceeds the limit and is given by the limit itself [1]. Frictional effect is modeled using extended coulomb frictional model, used by many researchers including Raghavendra [1, 2, 11-14, 17, 18]. Equations are expressed as following,

$$\tau_{fric} \equiv \begin{cases} \mu p_{contact} & \text{if} \quad \mu p_{contact} < \tau_{crit} \quad \left(\text{sliding region, } l_p > 0\right) \\ \tau_{crit} & \text{if} \quad \mu p_{contact} \geq \tau_{crit} \quad \left(\text{sticking region, } l_p < l_c\right) \end{cases} \tag{2.16}$$

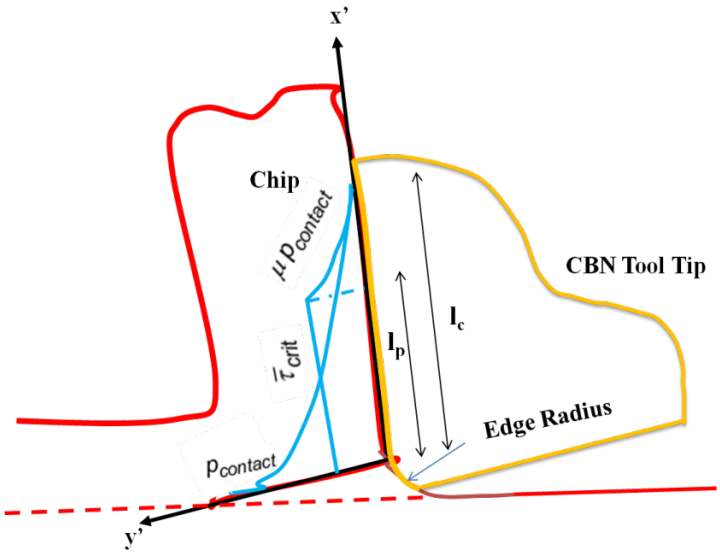

Figure 2.9: Contact model for tool-chip interface [1]

Akbar [12] estimated friction coefficient μ along the tool-chip interface for each cutting condition based on the experimental measurement of cutting force during the cutting process as,

$$\mu = \frac{F_f \cos\alpha + F_c \sin\alpha}{F_c \cos\alpha - F_f \sin\alpha}, \tag{2.17}$$

where F_c and F_f are the measured forces in the cutting velocity and feed directions respectively, and α is the rake angle.

Abdelmonein [56] mentioned that rubbing effects are important and have a very high influence especially over the feed force. Thus, the friction coefficient obtained is a mix of friction effects and those rubbing effects. Due to this phenomenon, Merchant's [57] approach used by several authors to identify a constant friction coefficient (μ) as function of the feed force

(F_f), cutting force (F_c), and rake angle (α) is not accurate. The following expression allows obtaining the average constant friction coefficient (μ) after Merchant's approach:

$$\mu = \tan[\arctan\left(\frac{Ff}{Fc}\right) + \alpha\ ]. \tag{2.18}$$

In this expression, the rake angle α allows obtaining friction coefficient over the rake surface.

In order to better identify a Coulomb friction coefficient at the tool–chip interface, Albrecht's [58] work's analysis has been used. This method allows measuring of tool–chip friction coefficient over the rake surface, eliminating cutting edge effects. According to the orthogonal cutting scheme, Fig. 2.10 shows the force decomposition proposed by Albrecht. The resultant R sum of the feed force (F_f) and cutting force (F_c) can be considered as well as the sum of two other components P and Q. The component P would represent the force resulting from localized phenomena close to the cutting edge (rubbing, forcing back), that is, the non-linear zone in the F_f–F_c curve. On the other hand, the component Q represents the force applied on the rake face, that is, the linear zone in the F_f–F_c curve. Albrecht's method suggests not considering the P component to assess the friction coefficient (μ), which will be determined using only the Q component. For instance, in Fig. 2.10b the resultant R, sum of the feed force (F_f) and cutting force (F_c) for a feed rate $f = f_7$, can be split in the force P and the force $Q = Q_7$. The force Q_7 (corresponding to f_7), which acts only over the rake surface, can be split into normal (Q_N) and tangential (Q_T) contributions, thus defining a tool–chip contact friction after Albrecht's method μ_A:

$$\mu_A = \left(\frac{Q_T}{Q_N}\right) \tag{2.19}$$

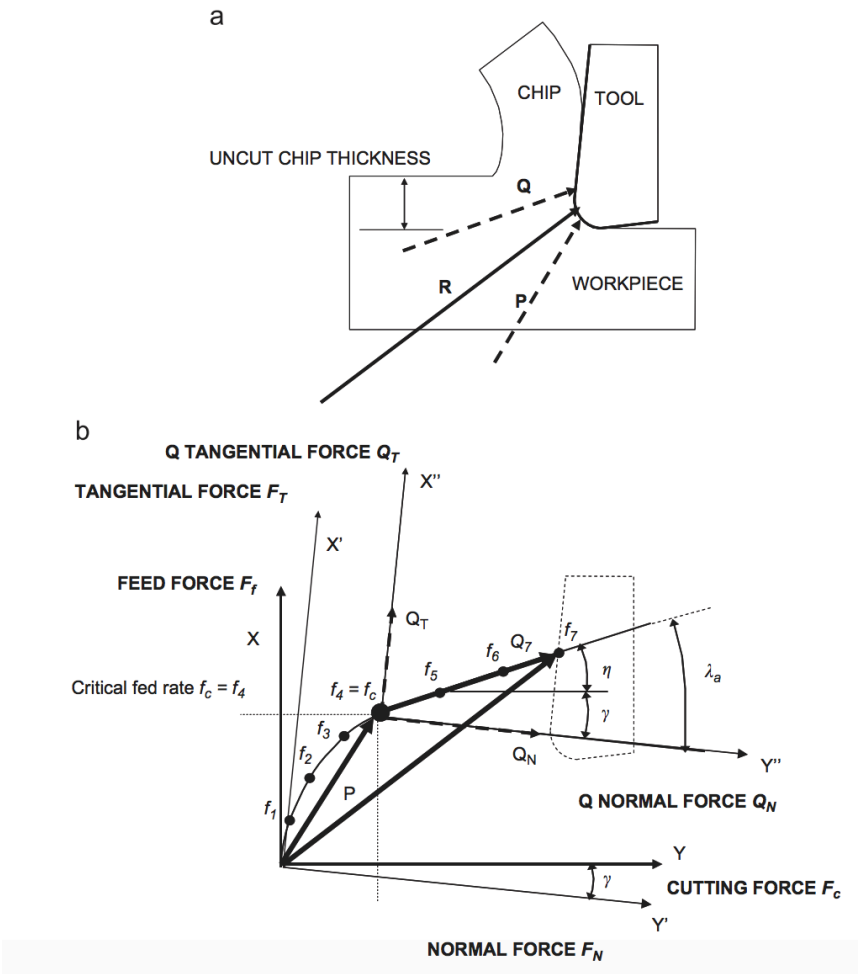

Fig. 2.10 (a) Forces decomposition in the Albrecht's model. (b) Plot F_f–F_c for different feed rates in order to obtain friction coefficient after Albrecht's method [58].

Raghavendra used the method that assumes the pressure on the rake face of the tool tip during cutting machining process to be very high so that the frictional shear stress is beyond the maximum shear strength of the material at the tool-chip interface. For this study, the threshold for shear frictional stress is set as 549MPa [1] and coefficient of friction value μ is set to 0.5 [1].

Model Geometry

The 3D micro-groove cutting model is developed by Bourne [2] and more detailed

information about the model geometry can be found in his thesis. The workpiece portion of the model consists of five parts that are meshed separately than joined using surface-based mesh tie constraints, which perform interpolation over interfaces where mating nodes do not line up perfectly. The five parts are identified as the cut work (Fig. 2.4A), uncut work (Fig. 2.4B), support work 1 (Fig. 2.4C), support work 2 (Fig 2.4D), and end support (Fig. 2.4E). Note that all of the workpiece elements are assigned aluminum material properties except elements in the Direction of Cut bottom 2 μm of support work 2 and end support parts, which are assigned silicon material properties, where the [100] crystalline direction is coincident with the y-axis as it is defined in Fig. 7.7. Additionally, two sets of aluminum material properties are used, one the does not allow for element failure and deletion and one that does, in order to handle separation of the chip from the workpiece.

The tool to be modeled was rounded at bottom with a radius of 893 nm. Additionally, some rounding with a radius of 60 nm was present on edges of the tool formed via a focused ion beam. This means that a completely correct model of the tool would have a rounded cutting edge and rounded non-cutting edges. However, if a rounded cutting edge is used, a very dense mesh would be required in the vicinity of the cutting edge, which would increase computer time significantly. Also, in order for separation of the chip to occur there would have to be a region of elements in line with the cutting edge capable of failure, which would cause the contact problem that motivated the use of a line of fallible elements below the chip to return. The tool model shown in the figure has a 0 degree rake angle, a 20 degree end clearance angle, a 5 degree side clearance angle, and a perfectly sharp cutting edge. Also, as shown in Fig. 2.11B, the tool has a rounded bottom with a radius of 893 nm. As shown in Fig. 2.11C, the side edge of the tool also has a radius of 60 nm.

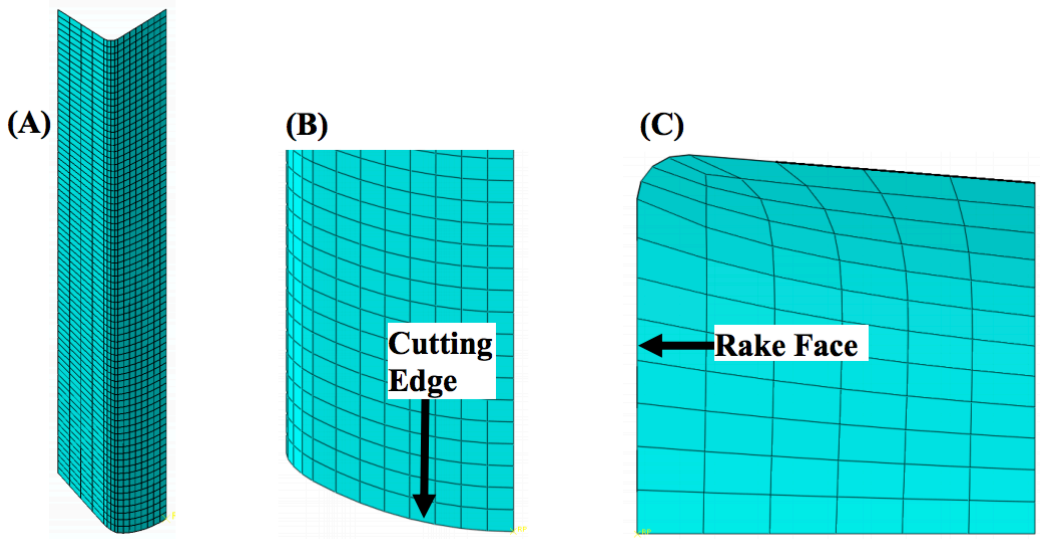

Fig. 2.11 (A) Tool mesh 3D view, (B) rake face view, (C) and top down view [2]

2.4 Heat Generation Model

Heat generated in metal cutting can have a significant effect on chip formation, tool wear and the quality of the finished surface [18]. Thus, choosing the right formulations to model the heat effect is one of the main keys.

Due to the properties of metal and the high temperature induced during the cutting process, the material properties often change as the temperature is raised. Thus, the coupled thermo-mechanical assumption is employed in the heat generation mode of metal machining simulation, which is used many researchers such as Raghavendra, Mabrouki, Akbar, Sulaiman, Chandrakanth and Shi [1, 11, 12, 14, 17, 18]. Referring to the Abaqus user's manual [16], a fully

coupled thermal-stress analysis is needed when the stress analysis is dependent on the temperature distribution and the temperature distribution depends on the stress solution. For example, metalworking problems may include significant heating due to inelastic deformation of the material, which, in turn, changes the material properties. In addition, contact conditions exist in some problems where the heat conducted between surfaces may depend strongly on the separation of the surfaces or the pressure transmitted across the surfaces. For such cases the thermal and mechanical solutions must be obtained simultaneously rather than sequentially. Coupled temperature-displacement elements are provided for this purpose in Abaqus/Explicit.

In Abaqus/Explicit the heat transfer equations are integrated using the explicit forward-difference time integration rule,

$$T^{N}_{(i+1)} = T^{N}_{(i)} + \Delta t_{(i+1)}\, \dot{T}^{N}_{(i)}, \tag{2.20}$$

where T^{N} is the temperature at node N and the subscript i refers to the increment number in an explicit dynamic step. The forward-difference integration is explicit in the sense that no equations need to be solved when a lumped capacitance matrix is used. The current temperatures are obtained using known values of $\dot{T}^{N}_{(i)}$ from the previous increment. The values of $\dot{T}^{N}_{(i)}$ are computed at the beginning of the increment by,

$$\dot{T}^{N}_{(i)} = (\alpha^{NJ})^{-1}\, (P^{J}_{(i)} - F^{J}_{(i)}), \tag{2.21}$$

where α^{NJ} is the lumped capacitance matrix, P^{J} is the applied nodal source vector, and F^{J} is the internal flux vector. The mechanical solution response is obtained using the explicit central-difference integration rule with a lumped mass matrix. Since both the forward-difference and central-difference integrations are explicit, the heat transfer and mechanical solutions are

obtained simultaneously by an explicit coupling. Therefore, no iterations or tangent stiffness matrices are required.

The consideration of convection effect and adiabatic heat transfer assumption are widely popular for metal cutting modeling. According to Umbrello [54], two aspects have to be carefully taken into account as far as heat flow prediction is concerned towards convection effect, the evaluation of the global heat transfer coefficient at the tool-chip interface, which is a variable that evaluates the heat transfer between tool and workpiece, as shown in Fig. 2.12. Particularly, the total amount of heat generated Q consists of two quotas, one of which is friction heat Q_1 and the other one is heat flux generated by the temperature difference of tool and workpiece Q_2, according to Fig. 2.13. Considering the temperature of tool tip, it is nearly independent of heat transfer coefficient, but Q_2 is calculated based on heat transfer coefficient. The other research that considered heat transfer coefficient for metal cutting simulation is Llanos [13]. He also included radiation into one of the factors for heat transfer. According to thermal boundary condition figure summarized by him (Fig. 2.14), convection and radiation happened at the outter surfaces of tool, chip formed and top surface of workpiece.

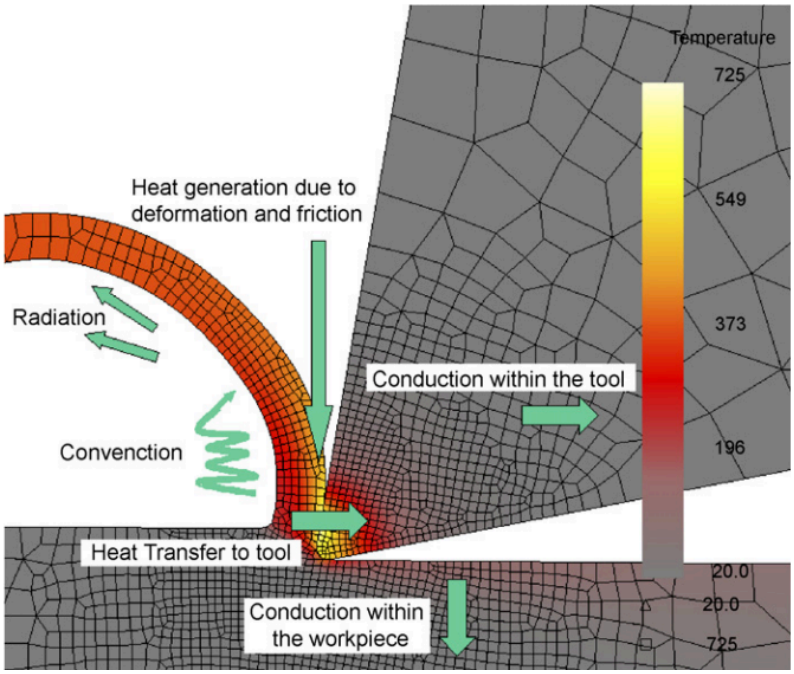

Fig. 2.12 Heat propagation in the bodies and toward the environment [54]

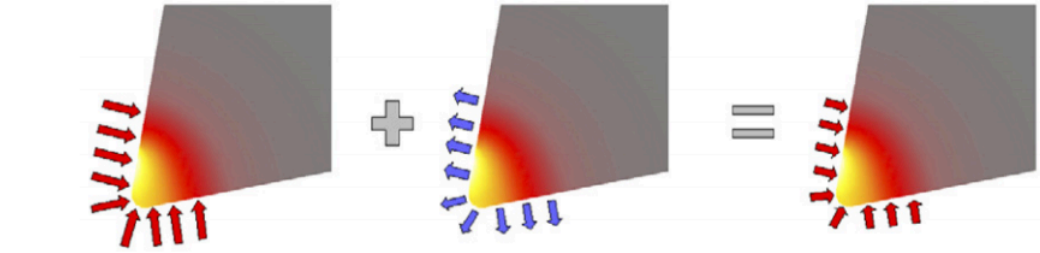

$Q_1 = J \times \lambda \times \tau_f \times v_s$

$Q_2 = h \times (T_W - T_T)$

$Q = Q_1 + Q_2$

Q_1 = Friction heat flux
λ = Heat partition factor
J = Energy conversion factor
τ_f = Shear stress at the interface
v_s = Sliding velocity

Q_2 = Contact heat flux
h = Global heat transfer coefficient at the interface
T_W = Workpiece contact temperature
T_T = Tool contact temperature

Q = Total heat flux applied to the contact elements at the tool-chip interfaces

Fig. 2.13 Heat generation at tool-workpiece interface [54]

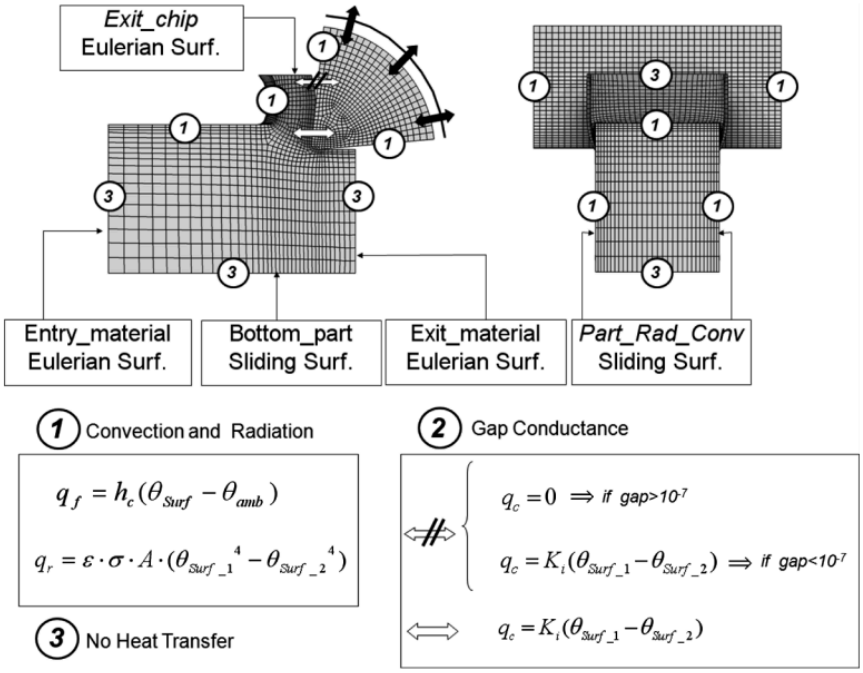

Fig. 2.14 Thermal Boundary Conditions [13]

The adiabatic assumption is adopted generally beside convection effect for the heat generation model of metal cutting process [1, 6, 11, 12, 17, 18, 26]. In metal cutting, the heat generated from the workpiece and tool does not have enough time to diffuse away, which means that there is no thermal interaction between the tool and the workpiece such as convection. An adiabatic stress analysis is used in cases where mechanical deformation causes heating but the event is so rapid that this heat has no time to diffuse through the material—for example, a very high-speed forming process [16]. It can be conducted as part of a dynamic analysis or as part of a static analysis if parts of the model are elastic only—no change in temperature occurs in the elastic regions; and it requires that a material's density, specific heat, and inelastic heat fraction (fraction of inelastic dissipation rate that appears as heat flux) be specified. It is typically used to simulate the high speed machining processes involving large amounts of inelastic strain, where

the heating of the material caused by its deformation is an important effect due to the temperature-dependent properties of material. The temperature increase is calculated directly at the material integration points based on the adiabatic thermal energy increases caused by inelastic deformation, which means temperature is not a degree of freedom any more in the problem. Conduction is disabled in the adiabatic analysis.

2.5 Gap in the Knowledge

Heat generation in metal cutting comes from plastic deformation occurring between the chip and uncut part of the workpiece, and friction induced between the rake face of the tool and chip, and the flank face of the tool and uncut workpiece [11, 12, 26, 17, 18]. Raghavendra [1] modified the micro-groove cutting of a steel workpiece using a rigid Cubic Boron Nitride (CBN) tool tip by including the plastic heat generated during the cutting process. However, the model did not include the heat generated by friction, especially, the heat generated due to sliding friction occur intensively at the tool-chip interface during the metal cutting process [11, 12, 17, 26, 55]. Further, Raghavendra implemented adiabatic assumption and plastic deformation heat mode in his modeling. However, his assumption of being 90% heat from the plastic deformation is not reasonable, resulting in the incorrect temperature profiles for the micro-groove cutting process. Thus, there is a need to enhance heat model that takes into account both friction heat as well as plastic deformation.

2.6 Chapter Summary

To summarize, this chapter reviews the literature of what methodologies other researchers have used for the FEA modeling of metal cutting. To obtain desired insights of the micro-groove cutting process, Abaqus/Explicit of finite element analysis used by Bourne [2] is discussed in detail. Due to the invalid plain strain assumption, 3D modeling is necessary for micro-groove cutting according to Bourne [2]. Besides, in order to save the computational time half-symmetry geometry is used. Moreover, remeshing techniques such as Lagrangian, Eulerian and Adaptive Lagrangian-Eulerian are widely implemented in the metal cutting simulation. To simulate the contact algorithm, general contact and extended coulomb frictional model are implemented in the software. Lastly, for heat generation, adiabatic coupled thermo-mechanical algorithm is appropriate and two sources of heat generation, namely heat generation from plastic deformation and friction heat are considered.

Chapter 3

Heat Generation Model

3.1 Introduction

In micro-groove cutting of a steel workpiece using a rigid Cubic Boron Nitride (CBN) tool tip, the heat generated during the cutting process includes heat from plastic deformation as well as friction, especially, the heat generated due to sliding friction at the tool-chip interface [11, 12, 17, 26, 55]. Raghavendra [1] recently developed a thermo-mechanical model that only considers heat generated from the plastic deformation. However, due to the temperature-dependent elastic and elastic-plastic properties of the steel, the high temperature caused by friction is found to strongly influence the tool-chip contact length, the shear angle, and the cutting forces [18, 26]. The objective of this chapter is to develop an enhanced 3D finite element analysis model to predict the machining performance of the micro-groove cutting in steel by including the heat generation from friction in the coupled thermo-mechanical model.

3.2 3D FEA Model Enhancements

3.2.1 Summary of the Enhancements to the Existing 3D FEA Model

In this research, the focus is on the enhancement of the 3D model for micro-groove cutting process developed by Raghavendra [1] that studies the micro-groove cutting in steel

using CBN tool tip. The model makes use of Abaqus/Explicit dynamic process, overall geometry, material properties of steel 4340, half symmetry boundary condition, adaptive Lagrangian-Eulerian remshing formulation, and Johnson-Cook chip separation criteria. Most of the features are kept the same in developing the improved model. The improvements are in heat generation mode where the heat generated due to friction is considered in addition to heat generated for inelastic deformation.

A complete finite element method flow chart for the micro-groove cutting modeling is shown in Fig. 3.1. To develop the fully thermo-mechanical analysis, the coupled thermo-mechanical model formulations shown as the looping-back link from temperature to the stress in the flow chart, is discussed first. A discussion on the heat induced by friction as well as heat caused by plastic deformation is given next, specifically, the inelastic, frictional heat fractions, and frictional equivalent heat conversion factor for the tool-chip interface are determined. Following the discussion on heat generation, the friction contact modeling that computes the frictional shear stress at the tool-chip interface is addressed (see the connecting block between the chip-flow and the heat generation in the flow chart). Finally, the model implementation issues dealing with the representation of tool-workpiece surface contact and mesh partitioning are given.

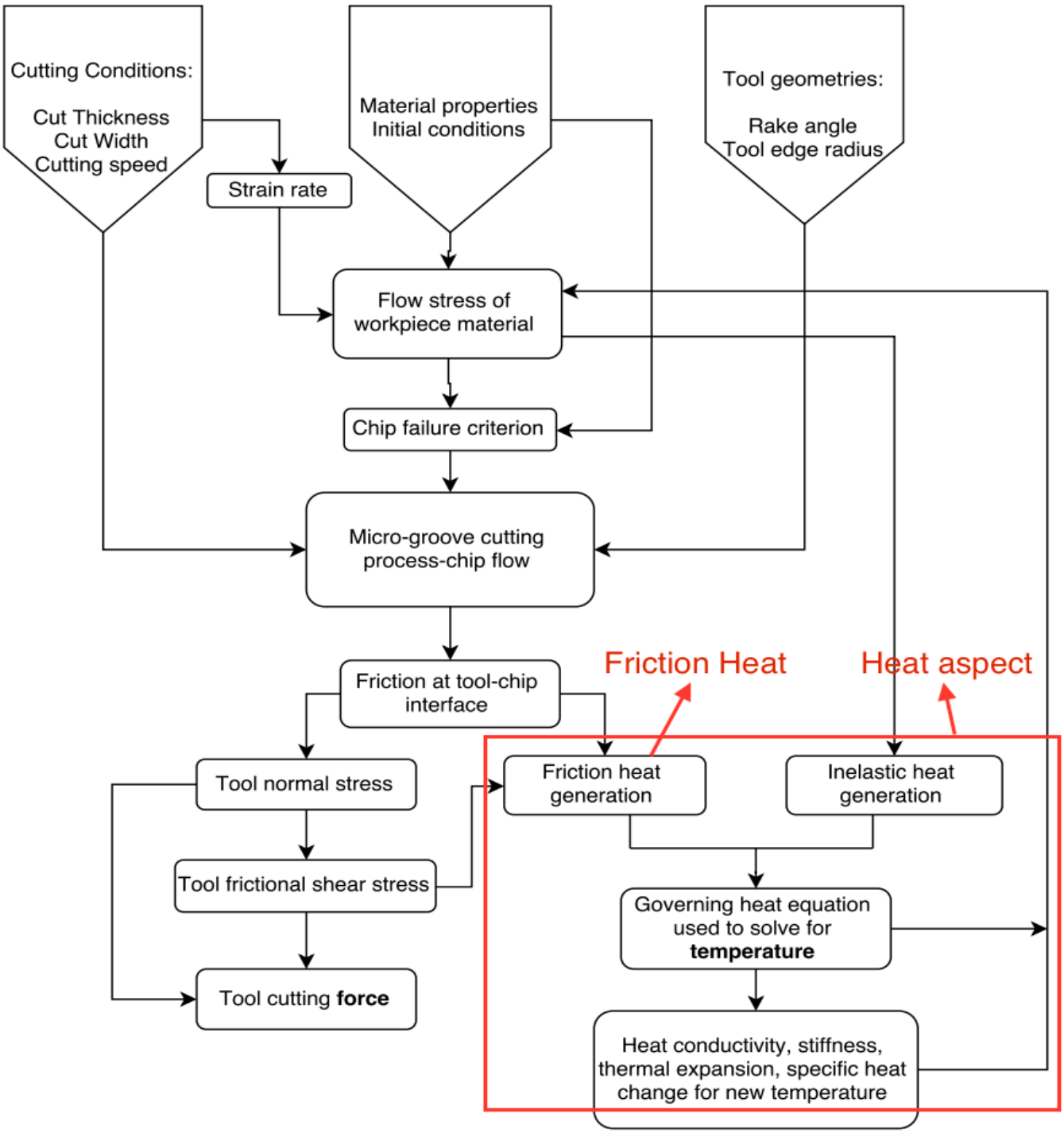

Fig. 3.1 Modeling of micro-groove cutting process using the FEM based process simulation technique

3.2.2 Fully Coupled Thermal-mechanical Model Formulation

As discussed by Bourne [2] and Raghavendra [1], in addition to 3D stress and strain fields, half-symmetry boundary condition, rigid tool, and isotropic material in micro-groove cutting process, the adiabatic assumption is chosen to address heat generation between the tool and the workpiece. The heat generation due to local energy dissipation occurs so quickly that it doesn't have the time to diffuse away and local heating will occur in the active primary and secondary deformation zones. This approach simplifies computation and reduces the required computing time.

The high temperature of the chip and the tool in machining can result in a significant effect on chip formation, tool wear and the quality of the finished surface. The temperature rise is essentially caused by the heat generated in the primary and secondary zones during metal cutting. The heat that flows along the chip and workpiece through conduction dominates the heat transfer due to the adiabatic assumption made here. Further, due to the relatively poor conductivity of the steel, the heat spreads out slowly and the vast temperature rise is concentrated at the tool-chip interface. Therefore, it is necessary to consider the thermo-mechanical coupling for micro-groove cutting model that also takes into account the temperature-dependent mechanical properties [16].

Before introducing the thermo-mechanical formulation, the flow chart shown in Fig. 3.1 is discussed first. The mechanical flow stress $\bar{\sigma}$ is computed based on material property related parameters (A, B, D, m), strain ε, strain rate $\dot{\varepsilon}$, and the T temperature by Equation 3.1. Ambient temperature is used as the initial temperature.

$$\bar{\sigma} = [A + B\ (\varepsilon)^n]\ [1 + D\ \ln(\frac{\dot{\varepsilon}}{\dot{\varepsilon}_p})]\ [1 - (\hat{\theta}(T))^m]. \quad (3.1)$$

The chip failure and chip flow model are executed for simulating the chip formation. The friction at the tool-chip interface is obtained based on the flow stress formation. In this research, a friction heat generation module is added to compute the heat generation caused by the friction at the tool-chip interface. At the same time, the inelastic heat is obtained based on the flow stress. Having obtained both heat sources, heat equation is used to solve the current temperature. Lastly, the new temperature data feeds back to Equation 3.1 to get an updated data of the flow stress. Furthermore, the temperature-dependent material properties are also updated simultaneously.

The temperature $T_{(i+1)}$ at time i+1 is calculated for temperature T_i at time i and the temperature rate $\frac{\partial T}{\partial t}_{(i)}$. The equation governing is given as,

$$T_{(i+1)} = T_{(i)} + \Delta t\ \frac{\partial T}{\partial t}_{(i)}, \quad (3.2)$$

where the temperature rate at time i is computed by,

$$\frac{\partial T}{\partial t}_{(i)} = \alpha\ (\dot{q}_{(i)}{}' + \dot{f}_{(i)}). \quad (3.3)$$

In Eq. (3.3), α is the thermal diffusivity, $\dot{q}_{(i)}{}'$ is the ratio of the applied heat source and thermal conductivity k, and $\dot{f}_{(i)}$ is the internal heat change.

The regions of heat generation during micro-groove cutting process are shown in Fig. 3.2 [1]. Due to the adiabatic assumption, only heat generated from plastic deformation and sliding frictional effects in the primary shear zone and in the secondary shear zone are considered [2, 18,

23, 26]. In the primary deformation zone, heat comes from mostly inelastic work. The local heating and thermal softening effects of 4340 steel workpiece allow greater deformation. In the secondary deformation zone, heat generated is due to work done in deforming the chip (inelastic work) and in overcoming the sliding friction at the tool-chip interface zone. Lastly, the heat generated in the tertiary deformation zone comes from the work done in overcoming friction, which occurs at the rubbing contact between the tool tip and top part of the uncut workpiece.

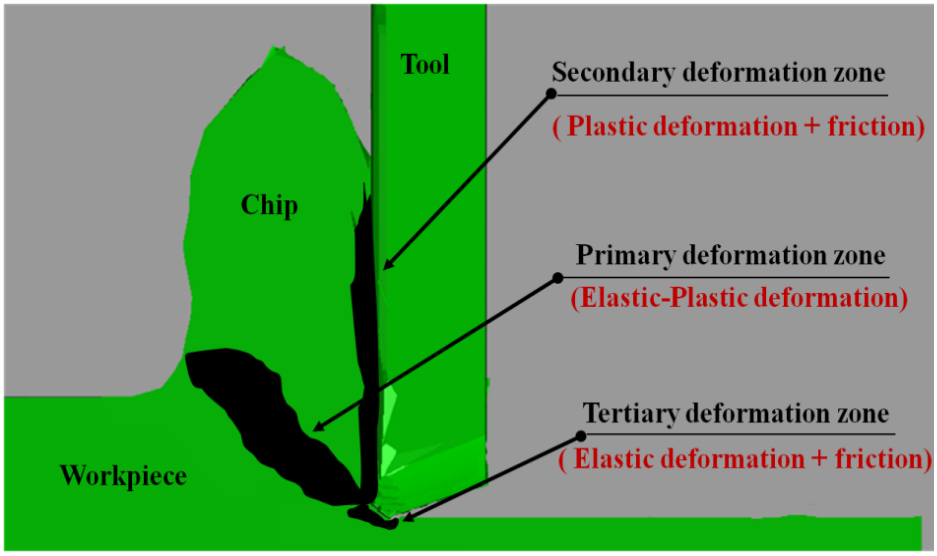

Fig. 3.2 Heat generation during micro-groove cutting [1]

In Equation 3.3 the internal heat change, $\dot{f}_{(i)}$ can be expressed as the second spatial derivatives (thermal conductions). The thermal diffusivity α can be expressed as a ratio of thermal conductivity k and the product between mass density ρ and specific heat capacity C. Therefore, Equation 3.3 becomes

$$\frac{\partial T}{\partial t}_{(i)} = \frac{k}{\rho\, C}\left[\left(\frac{\partial^2 T}{\partial x^2} + \frac{\partial^2 T}{\partial y^2} + \frac{\partial^2 T}{\partial z^2}\right)_{(i)} + \frac{\dot{q}_{(i)}}{k}\right]. \tag{3.4}$$

After rearranging the equation, the overall governing heat equation for the micro-groove cutting process is given below,

$$k\left(\frac{\partial^2 T}{\partial x^2}+\frac{\partial^2 T}{\partial y^2}+\frac{\partial^2 T}{\partial z^2}\right)_{(i)}+\dot{q}_{(i)}=\rho\ C\ \frac{\partial T}{\partial t}_{(i)}\ . \tag{3.5}$$

In order to solve for the temperature, the applied heat source $\dot{q}_{(i)}$ needs to be computed, which will be discussed in the following section.

3.2.3 Heat Induced by Plastic Deformation and Friction

The total heat generated in the primary and secondary zones $\dot{q}_{(i)}$ in Eq. 3.5 contains both plastic heat $\dot{q}_p$ and friction heat $\dot{q}_f$. The heat generation rate $\dot{q}_p$ due to inelastic work is given below [16],

$$\dot{q_P}=\beta\ \bar{\sigma}\ \dot{\varepsilon}_p, \tag{3.6}$$

where β is the inelastic heat fraction, $\bar{\sigma}$ is effective mises flow stress and $\dot{\varepsilon}_p$ is effective plastic strain rate.

The inelastic heat fraction (IHF) β, also known as the Taylor-Quinney coefficient, measures the fraction of the pleastic work that is converted to heat. IHF is determined using both theoretical and experiemental approaches by many researchers, including Quinney and Taylor [73], Mason [74], Pottier [75], and Knysh [76]. Mason [74] recently examined the IHF value for

AISI 4340 by using high-speed infrared detectors and the Kolsky bar. With the adiabatic assumption, the IHF can be expressed as,

$$\beta = \frac{\rho\, C\, \dot{T}}{\sigma(t)\, \dot{\epsilon}} = \frac{\rho\, C\, \dot{T}}{\dot{W}_p} \tag{3.7}$$

$$\sigma(\mathrm{t}) = \mathrm{E}\, \frac{A_o}{A}\, \epsilon_T(t), \tag{3.8}$$

where $\dot{T}$ is the temperature rate, σ(t) is the stress, $\dot{\epsilon}$ is the strain rate and the product of $\sigma(\mathrm{t})$ and $\dot{\epsilon}$ can be written as $\dot{W}_p$, E is the young's modulus, $\mathrm{A_o}$ is the orignal cross sectional area of the bar, A is the cross sectional area of the bar after being deformed, and $\epsilon_T(t)$ is the strain signal recorded by the strain gauges attached to the bar. Thus, the fraction has dependency of material properties, strain, and strain rate [73-76]. As it is shown in the Fig. 3.3, for AISI 4340 the IHF value resides at 0.8 as the strain approaches the steady state. Thus, $\beta = 0.8$ is used, in this study.

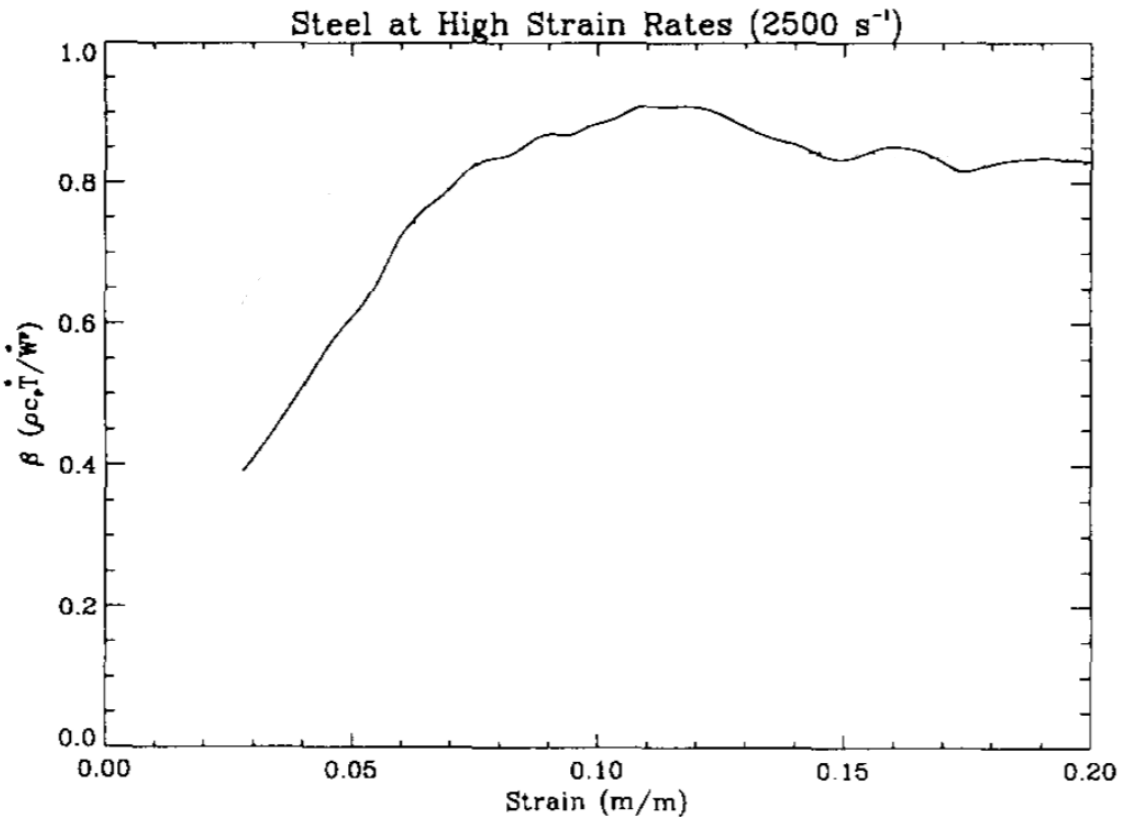

Fig. 3.3 The work rate to heat rate conversion fraction for AISI 4340 [74]

The heat generation on the chip due to friction, $\dot{q}_f$ is given below [16],

$$\dot{q_f} = \mathrm{J}\, \eta_f\, \tau_{fric}\, \dot{\gamma}, \tag{3.9}$$

where J is equivalent heat conversion factor that provides the percentage of frictional heat transferred to the chip, η_f is the fraction of dissipated heat due to friction, τ_{fric} is the frictional shear stress provided by the extended coulomb's friction model and $\dot{\gamma}$ is the shear strain rate.

Chen and Li [77] have studied the friction heat fraction η_f for the metal sliding process. They investigated the thermal aspects of friction processes, with the emphasis on frictional heating and its relation to energy conversion by extending the a micro-scale dynamic model

(MSDM), originally proposed by Li *et al*. [78], followed by Elalam *et al*. [79]. As shown in Fig. 3.4, during the sliding process, only a portion of the total mechanical work or the friction energy is converted to heat (thermal energy) and the remainder is dissipated into plastic deformation (strain energy), micro-cracks, and a change in surface roughness (fracture energy) [77]. Because micro-groove cutting is considered as a low-load and low-cutting speed process, the surface roughness does not change significantly, complying with the assumption of ignoring the surface roughness energy proposed by Chen and Li [77]. Moreover, at low sliding speeds and low loads, both the kinetic impingement between sliding surfaces in contact and the site–site bond deformation are small, with little plastic deformation. As a result, most of the mechanical work could change to heat and hence the η_f value is chosen as 0.9 for the current study.

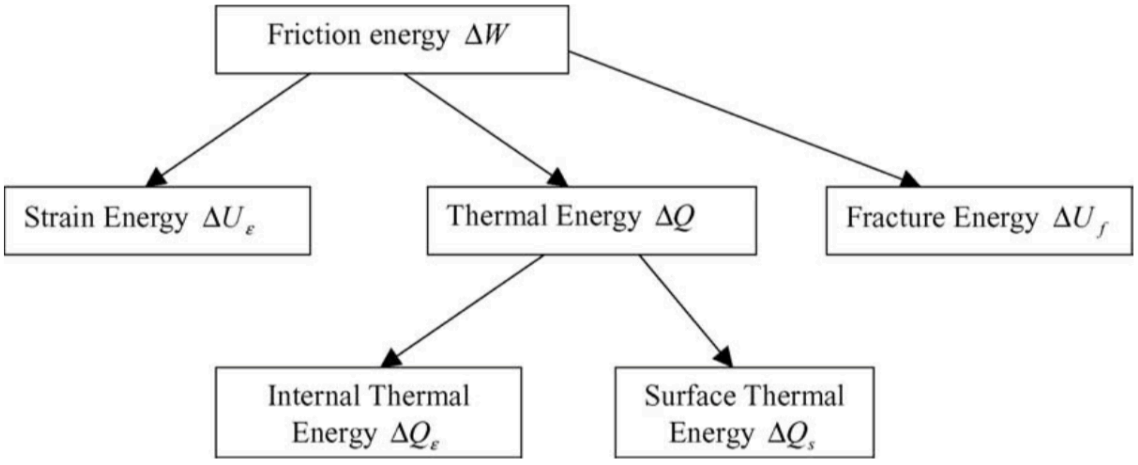

Fig. 3.4 Components of the friction energy or the consumed mechanical work during sliding [77]

Equivalent heat conversion factor J is determined by the emissivity of the workpiece ε_C and tool ε_T. Also the emissivity of the material is a variable of thermal conductivity k, density ρ, and specific heat capacity C, is given as [69].

$$J = \frac{\varepsilon_C}{\varepsilon_C + \varepsilon_T} \tag{3.10}$$

$$\varepsilon = (k * \rho * C)^{0.5} \tag{3.11}$$

Since the specific heat capacity C and thermal conductivity k of the workpiece and tool are both temperature-dependent variables, the emissivity ε could change upon the rise of temperature. However, specific heat capacity has a weaker temperature dependence at high temperatures for solid material such as steel and CBN [70]. In addition, thermal conductivity of metals is approximately proportional to the absolute temperature times electrical conductivity. In metals the electrical conductivity decreases with increasing temperature and thus the product of the two, the thermal conductivity, decreases in a small amount. In alloys the change in electrical conductivity is usually small and thus thermal conductivity increases with temperature, but still in a small amount [71, 72]. Considering the above reasons, and for simplification the J value can be assumed to remain constant with rise of temperature, and can be computed with material properties of tool and workpiece at room temperature. Thus, J is chosen to be 0.5, which means that the heat partition between the tool and the workpiece is equal for the micro-groove steel cutting. This is also in agreement with other researchers as shown in Table-3.1.

Table 3.1 Heat conversion factors J used in FEM models in steel cutting

Author and reference	Workpiece material	Cutting tool material	Heat partition to tool	FE software
Arrazola e al. [55]	AISI 4140	P10	0.5	Abaqus
Reginaldo et al. [65]	AISI 4340	PCBN	0.5	-
Shet and Deng [17]	AISI 4340	-	0.5	Abaqus
Shet and Deng [18]	AISI 4340	-	0.5	Abaqus
Shi and Liu [66]	AISI 52100	PCBN	0.5	Abaqus
Kai and Melkote [67]	AI5083-H116	Diamonds	0.5	Abaqus
Shi and Liu [68]	Hy-100	TPG 322 Inserts	0.5	Abaqus

3.2.4 Friction Contact Modeling

The frictional shear stress τ_{fric} as discussed in Equation (3.9) results from the normal stress between the contacting surfaces. Thus, to simulate the friction behavior, it is desirable to include both normal and frictional shear stresses in the model. According to Zorev [84], the normal stress is at the peak value at the tool-tip and gradually decreases to zero at the point where the chip separates from the rake face as shown in Fig. 3.5. The red curve represents the normal stress while the purple curve stands for the frictional shear stress. The normal stress drops

from a peak value at the point closest to the workpiece at the tool-chip interface to zero at the point where chip is just about to leave the tool rake face, while the frictional shear stress stays constant first then drops to zero. Over the portion of the tool-chip contacting area near the cutting edge (high normal stress), the sticking friction occurs, whereas for the remainder of the contacting area (low normal stress), the sliding friction occurs. As discussed in [83], at low normal stresses, the friction stress follows the Coulomb law equation, while it follows shear friction factor relation at high normal stresses, as shown below.

$$\tau_{slide} = \mu * \sigma_n \tag{3.12}$$

$$\tau_{stick} = \mathrm{k}_{\mathrm{chip}}, \tag{3.13}$$

where τ_{slide} and τ_{stick} are the frictional shear stresses in the sliding zone and sticking zone respectively, $\mathrm{k}_{\mathrm{chip}}$ is the average shear flow stress of the work material at the tool-chip interface. μ is the friction coefficient, and σ_n is the normal stress.

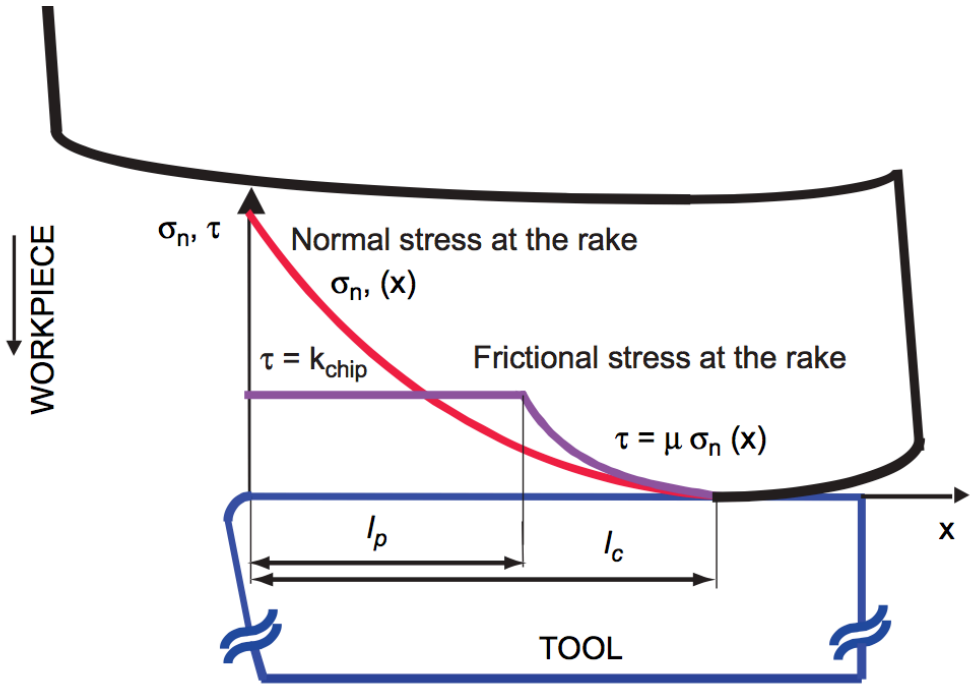

Fig. 3.5 Normal and frictional stress distributions on the tool rake face [83]

Thus, based on Zorev's development [84], the relationship between normal stress and frictional shear stress can be expressed as,

$$\begin{cases} \tau_{fric}(\mathrm{x}) = \tau_{stick} & \text{and when } \mu * \sigma_n(\mathrm{x}) \geq \tau_{stick}, 0 < \mathrm{x} < \mathrm{lp} \\ \tau_{fric}(\mathrm{x}) = \mu\, \sigma_n(\mathrm{x}) & \text{and when } \mu * \sigma_n(\mathrm{x}) < \tau_{stick}, \ \mathrm{lp} < \mathrm{x} < \mathrm{lc} \end{cases}, \tag{3.14}$$

where l_p is the sticking region distance, and l_c is the sliding region distance. The location of the separation of these two regions is often estimated from examining the marks left on worn tool rake face. Coefficient of friction μ can be obtained through cutting force F_c, thrust force F_t, and rake angle α, as

$$\mu = \frac{F_t + F_c \tan\alpha}{F_c - F_t \tan\alpha}. \tag{3.15}$$

Since for a three-dimensional simulation there are two orthogonal components of shear stress, τ_{fric1} and τ_{fric2}, along the interface between the two bodies and these components act in the local tangent directions for the contact surfaces or contact elements, the two components are combined into an "equivalent shear stress," $\tau_{fric-equi}$, where $\tau_{fric-equi} = \sqrt{{\tau_{fric1}}^2 + {\tau_{fric2}}^2}$.

Ozel and Altan [86] recently presented a methodology to determine the friction at the tool-chip interface by utilizing steel cutting experiments. The average shear flow stress (k_{chip}) was determined using computed average strain, strain-rate, and temperature in secondary deformation zone, while the friction coefficient (μ) was estimated by minimizing the difference between predicted and measured thrust forces from the experiments. The average shear flow stress and the coefficient of friction value determined from their experiment as 549 MPa and 0.5 respectively, are used in this research.

3.3 Model Implementation

In order to implement the friction contact model, the contacting surfaces between the tool and the workpiece need to be specified. Further, the mesh partitioning needs to be refined to deal with a meshing failure that may happen when a rounded tool is used.

3.3.1 Frictional Contacting Surfaces

In the frictional contact mode, the interacting surfaces need to be assigned in order to

simulate the frictional behavior. The frictional contacts are assigned between the rake face of the cutting tool and lower surface of the chip; and between the flank face of the cutting tool and upper surface of the workpiece, shown in Fig. 3.6.

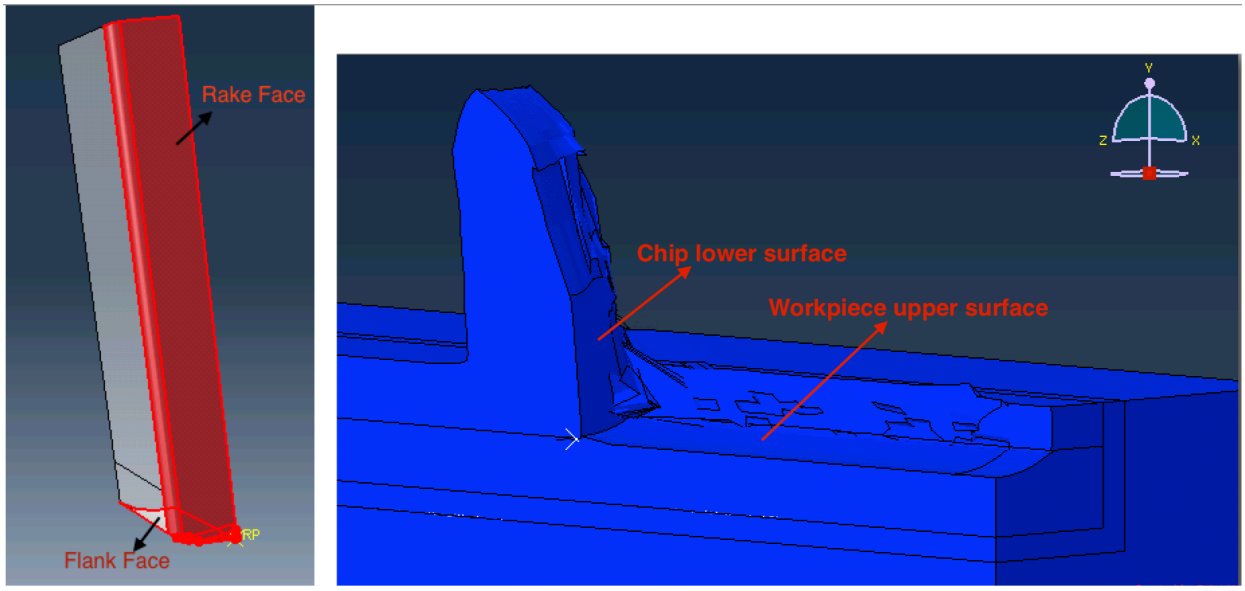

Fig. 3.6 (a) Tool; (b) workpiece

3.3.2 Mesh Changes

The influence of the radius of tool cutting edge on the friction heat and cutting force during the micro-groove cutting process is important for understanding the cutting mechanism. In this research, the tool is modeled using hexahedral element and without partitioning the tool, the meshed elements generated become non-hexahedral element at the junction of the flank face and the rounded edge (see Fig. 3.7), which causes a meshing failure. Thus, the tool is partitioned by dividing the rounded edge into two small sections, shown in Fig. 3.8. Fig. 3.9 shows the improved meshing.

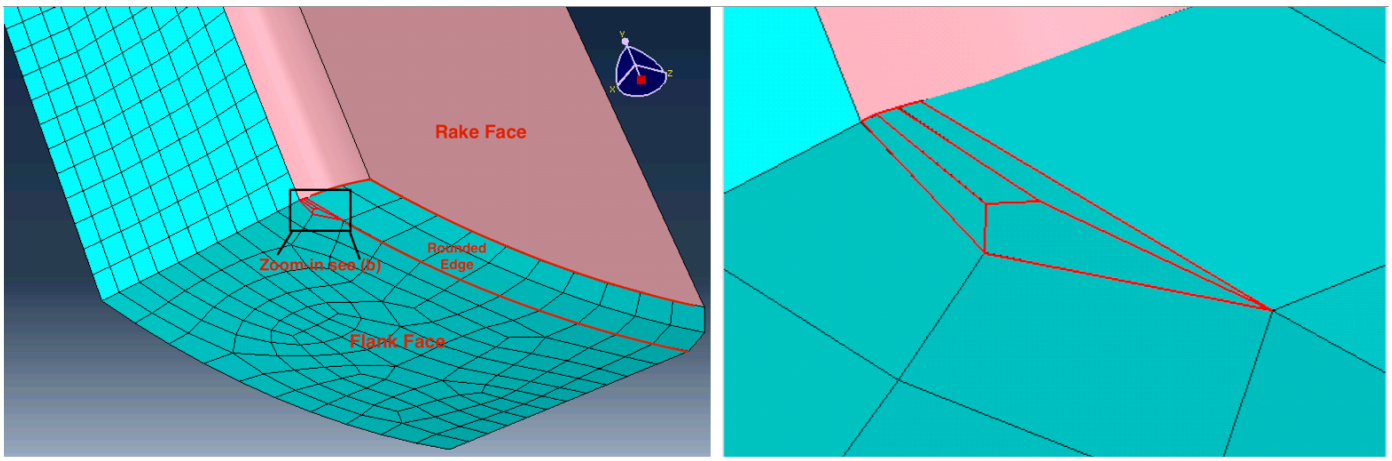

Fig. 3.7 Unpartitioned rounded tool detailed view

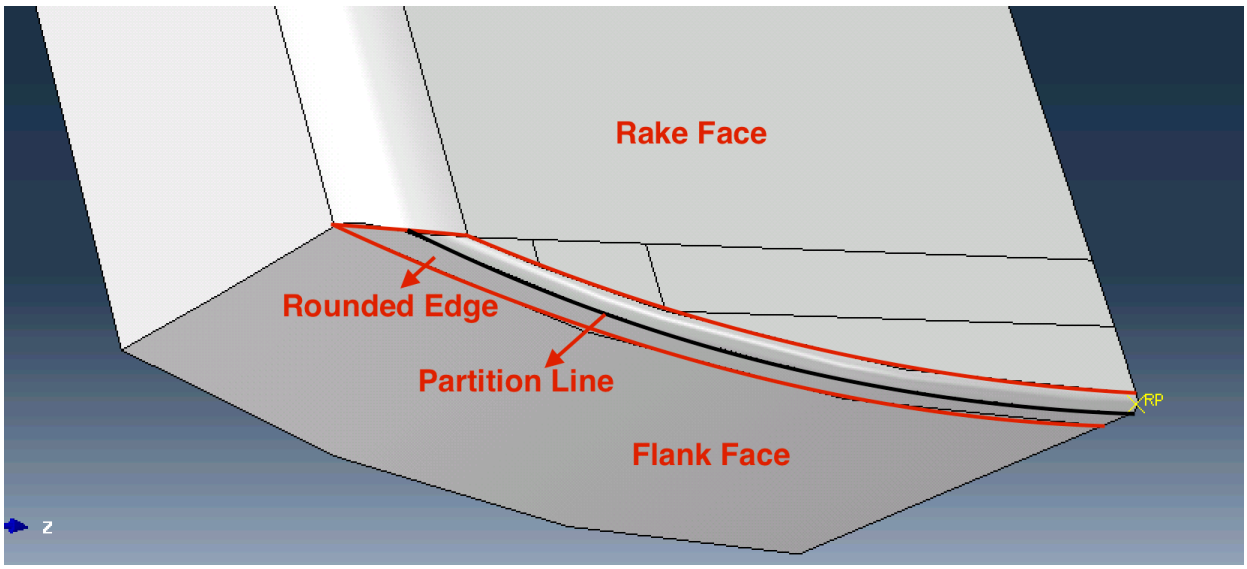

Fig. 3.8 Tool Partitioning

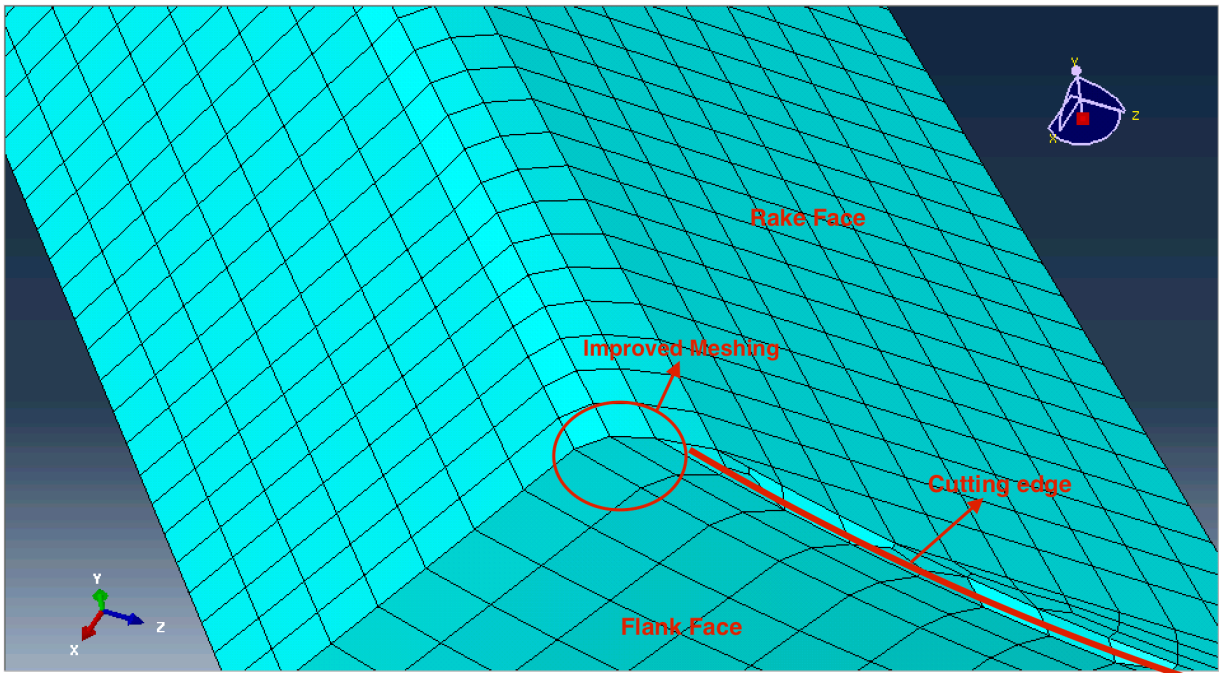

Fig. 3.9 Partitioned rounded tool detailed view

3.4 Summary

This chapter covers the enhancements to the heat generation model for the micro-groove steel cutting using CBN. The adiabatic assumption is made in the enhanced heat model since the heat diffuses quickly in the workpiece. The fully coupled thermo-stress and friction contact algorithm are used to formulate the heat model. The inelastic heat fraction, frictional heat fraction, and frictional heat conversion factor are chosen to be 0.8, 0.9, and 0.5, respectively. The contacting surfaces between the tool and the workipece are specified to show the frictional behavior. A mesh refining procedure is introduced to deal with the mesh failure due to the rounded tool edge.

Chapter 4

Model Validation and Simulation Results

4.1 Introduction

The goal of this chapter is to first validate the enhanced model, and then use the model to study the effects of various process parameters including cutting speed, rake angle, and tool edge radius on the microgroove machining performance measures including temperature, cutting force and von mises stress. The specific tasks that will be carried out to satisfy the stated goal are given below.

(12) Design the suitable simulation experiments for the purpose of model validation and to study the effect of process parameters on the machining performance;

(13) Validate the model by comparing burr formation and chip thickness data obtained from the enhanced model with the cross-sectional 2D AFM plot and SEM images of the chip roots;

(14) Study the effect of friction heat by comparing modeling outcomes in terms of temperature and cutting force obtained from the friction heat-enabled model with the ones from friction heat-disabled model;

(15) Show the importance of coupled thermo-mechanical model for the micro-groove cutting by comparing temperature and cutting force results of the coupled model with the model that does not consider coupling between the thermal and mechanical components;

(16) Study the effects of cutting speed, tool edge geometry, and tool rake angle on the micro-groove cutting performance in terms of cutting force, von mises stress, and temperature;

4.2 Design of Simulation Experiments

The simulation experiments are organized into three phases. In the first phase, the two depths of cut (0.5 μm and 0.96 μm) are considered at two levels of cutting speed (100mm/min and 300mm/min) for a fixed cutting tool edge radius and rake angle, as shown in Table 4.1. In order to validate the model, the parameters such as groove image, side burr height, and chip thickness obtained from the simulation are compared with the experimental results obtained earlier by Raghavendra [1].

Table 4.1 Simulation Experiments: Phase 1-Validation

Rake Angle (deg)	Cutting Speed (mm/min)	Cut Depth (nm)	Cutting Edge Geometry (nm)
0	300	500	R0
		960	
	100	500	
		960	

In the second phase, simulation experiments are designed to study the significance of coupling the mechanical and thermal effects and including the friction heat in the enhanced model. The coupled and uncoupled models that include frictional heat effect are used to simulate the machining responses for the cutting conditions of cutting speed of 300 mm/min, sharp cutting edge, and 0 degree rake angle, as well as for cutting speed of 300 mm/min, 60 nm radius cutting edge, and -5 degree rake angle, respectively and are shown in Table 4.2. The comparison between the coupled model with and without friction heat is also made by conducting the model simulation for the cutting conditions with the combination of cutting speeds 100 mm/min and 300 mm/min, tool edge radii 0 nm and 60 nm (R60), tool rake angles -5 degrees and 10 degrees,

respectively. These simulation experiments are performed with a depth of cut of 500 nm.

Table. 4.2. Simulation Experiments: Phase 2-Thermo-coulping and friction heat effects

	Test No.	Friction Heat	Coupling	Rake Angle (deg)	Cutting Speed (mm/min)	Cutting Edge Geometry (nm)
Coupled Mechanical and Thermal Effects	1	Yes	No	0	300	R0
	2			-5		R60
	3		Yes	0		R0
	4			-5		R60
Friction Heat Effects	5	No	Yes	-5	100	R0
	6					R60
	7			10		R0
	8					R60
	9			-5	300	R0
	10					R60
	11			10		R0
	12					R60
	13	Yes		-5	100	R0
	14					R60
	15			10		R0
	16					R60
	17			-5	300	R0
	18					R60
	19			10		R0
	20					R60

Table 4.3 gives a list of simulation experiments that are designed to study the effects of cutting speeds, cutting edge radii, and tool rake angles using the enhanced coupled model that also considers friction heat on the machining response including temperature, cutting force, and stress. In these experiments, a depth of cut of 500 nm is used.

Table 4.3 Simulation Experiments: Phase 3

Cutting speed (mm/min)	Tool rake angle (degree)	Tool Geometry (nm)
300	-5	R0
		R60
	10	R0
		R60
100	-5	R0
		R60
	10	R0
		R60

Figure 4.1 shows a schematic of a tool with rounded edge, with tool edge radius 'R'. The rake angle is defined as the angle made between the rake face and the vertical reference line, as shown in the Figs. 4.2 and 4.3.

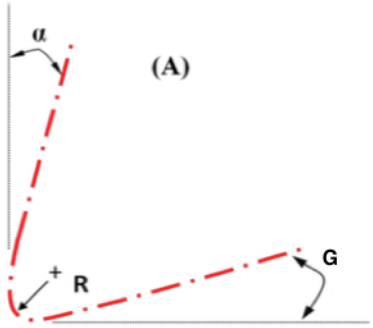

Fig. 4.1 Geometry of rounded tool cutting edge (α, rake angle and G, end clearance angle, are maintain the same)

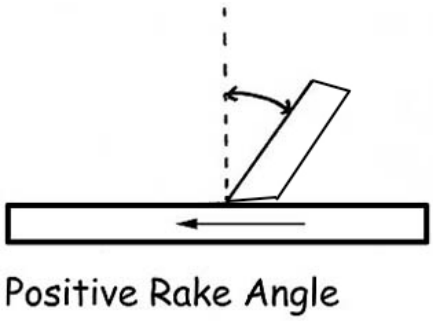

Fig. 4.2 Positive rake angle schematic

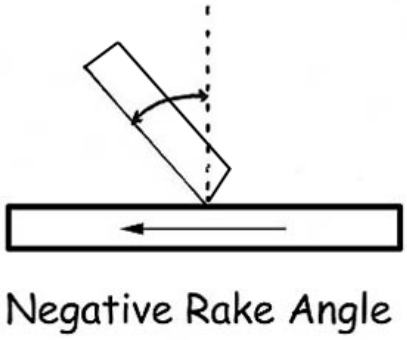

Fig. 4.3 Negative rake angle schematic

The other geometries of the cutting tool are maintained unchanged throughout the simulation, such as bottom radius of 945 nm (see Fig. 4.4I) and side non-cutting edge radius of 60 nm, to account for the features produced as a result of FIB-machining during the actual cutting process by Raghavendra [1]. The rake face and cutting edge profiles of the tools are shown in Figs. 4.4 and 4.5. The width of the cutting tool tip is measured to be 1.25 μm [1].

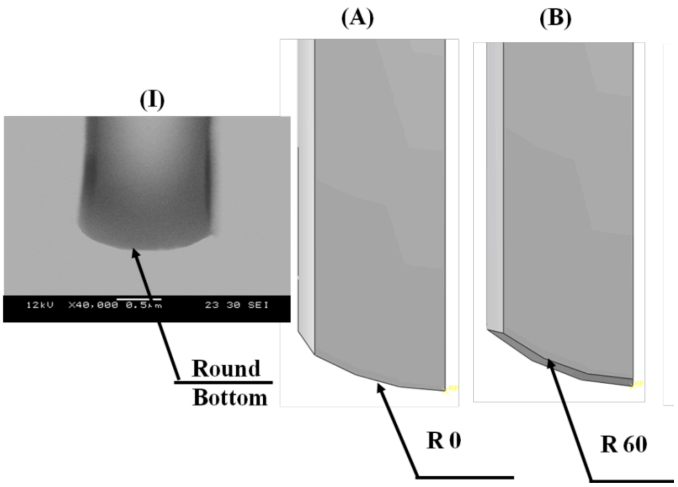

Fig. 4.4 Rake face profile of various CBN tool tip geometries: (I) FIB-machined; (A) Sharp Tool with infinite edge radius (R0); (B) Round tool with 60nm edge radius [1];

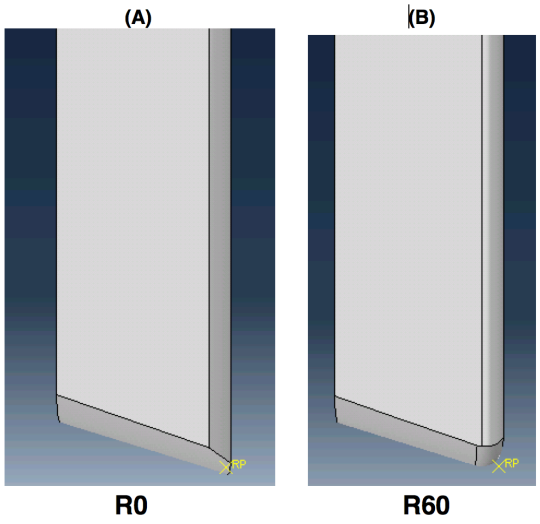

Fig. 4.5 Side profile of various CBN tool tip geometries: (II) FIB-machined; (A) Sharp Tool (R0); (B) Round tool with 60nm edge radius;

4.3 Model Inputs

The enhanced model uses a number of mechanical and thermal properties for the workpiece. This section lists these properties that are obtained from previous studies [18, 20, 22]. The constants of the JC constitutive model for AISI 4340 are provided in Table 4.4. The constants for JC ductile fracture mode are given in Table 4.5. The mechanical, elastic and thermal properties of AISI 4340 are summarized in Table 4.6.

Table 4.4: JC constitutive model parameters of AISI 4340 [20]

Parameters	Values
Yield stress, A	792 MPa
Strain hardening coefficient, B	510 MPa
Strain rate factor, D	0.014
Strain exponent, ε	0.26
Temperature exponent, m	1.03
Reference plastic strain rate, $\dot{\varepsilon o}$	$1s^{-1}$
Current Temperature, T	20 °C

Table 4.5: Johnson and Cook Damage law parameters [20]

Parameters	Values
Initial failure strain, d_1	0.05
Exponential factor, d_2	3.44
Triaxiality factor, d_3	2.12
Strain rate factor, d_4	0.002
Temperature factor, d_5	0.61
Transition Temperature	1520 °C

Table 4.6: Mechanical and thermal properties of AISI 4340 [18, 22]

Property	**AISI 4340**	
Modulus of Elasticity 'E', GPa	Temp (°C)	Values
	20	207
	150	190
	250	70
	350	35
Poisson Ratio 'υ'	0.3	
Density, 'ρ', (kg/m^3)	7830	
Heat treatment	Austentized	
Hardness	30 HRc	
Thermal Conductivity, 'k', (W/m °C)	100	42.7
	200	42.3
	400	37.7
	600	33.1
Property	AISI 4340	
Melting Temperature (°C)	1520	
Linear coefficient of thermal	100	12.4
expansion, (µm/m °C)	300	13.6
	500	14.3
Specific Heat, 'C', (W/m °C)	100	473
	300	519
	500	561

4.4 Steady-state Attainment Analysis

During the microgroove cutting process, as the tool motion is initiated, the cutting force experienced by the tool increases from zero and reaches to a steady state value after certain time period, referred to a steady-state condition. In this study, the machine responses that are obtained after the process reaches the steady-state condition are used for comparison. Hence, the simulations are conducted to estimate the steady state condition during the micro-groove cutting process. In this research, the cutting process is assumed to reach the steady state when the tool-chip contact length remains constant.

Various simulations are run at depth of cut of 500 nm and cutting speed of 300 mm/min with a tool rake angle of 0^{o} to illustrate the evolution of continuous chip formation in micro-groove metal cutting. Figure 4.6 shows four plots of the chip flow geometry at different instances of the cutting process.

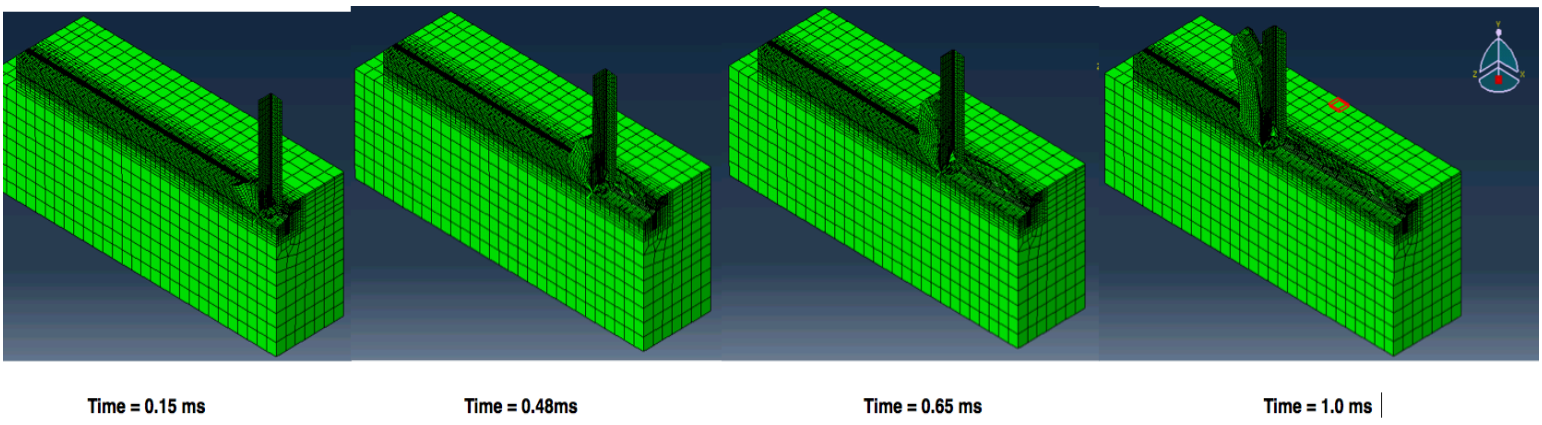

Fig. 4.6 Chip formation process for a depth of cut of 0.5 μm and speed of 300 mm/min

As shown in Fig. 4.6, a chip separates from the workpiece, flows up the rake face, and eventually separates from the rake face. It is noticed that tool-chip contact length remains

unchanged after 0.48 ms and the cutting process is said to reach the steady state. For the cutting condition with 300 mm/min cutting speed, the cutting process reaches steady state between 0.46 ms and 0.51 ms, while for cutting speed of 100 mm/min, the steady state is reached between 1.40 ms and 1.55 ms, respectively.

4.5 Model Validation

This section predicts the simulation results by using the enhanced model and comparing the modeling results with those obtained from Raghavendra's [1] experiments including micro-groove cross-sectional cut image, side burr height, and chip thickness. Four sets of simulation are run using the conditions listed in Table 4.1.

The experimental cross-sectional 2D AFM deformed figures obtained from Raghavendra [1] are superimposed on the cross-sectional deformed figure obtained for simulation using the enhanced thermo-mechanical model at steady-state condition. Figures 4.7 and 4.8 show the superimposition image of 2D AFM line profile of the experimental micro-groove cross-section and model simulated micro-groove cutting cross-section for depth of cut of 0.5 μm, machined with 100 and 300 mm/min, respectively. Figures 4.9 and 4.10 illustrate the superimposition images for 100 mm/min and 300 mm/min, respectively machined with depth of cut of 0.96 μm. As noticed that the left side of the experimental cross-sections obtained from AFM does not line up perfectly, due to tilt-based distortion caused by the high-aspect ratio AFM probes. Moreover, the cross-sectional image from simulation is symmetrical due to the half-symmetry assumption, so the right sides of the side burr match up poorly for simulating and experiment images. Lastly,

the side burr height seems to increase, as the depth of cut gets deeper, as shown in these figures.

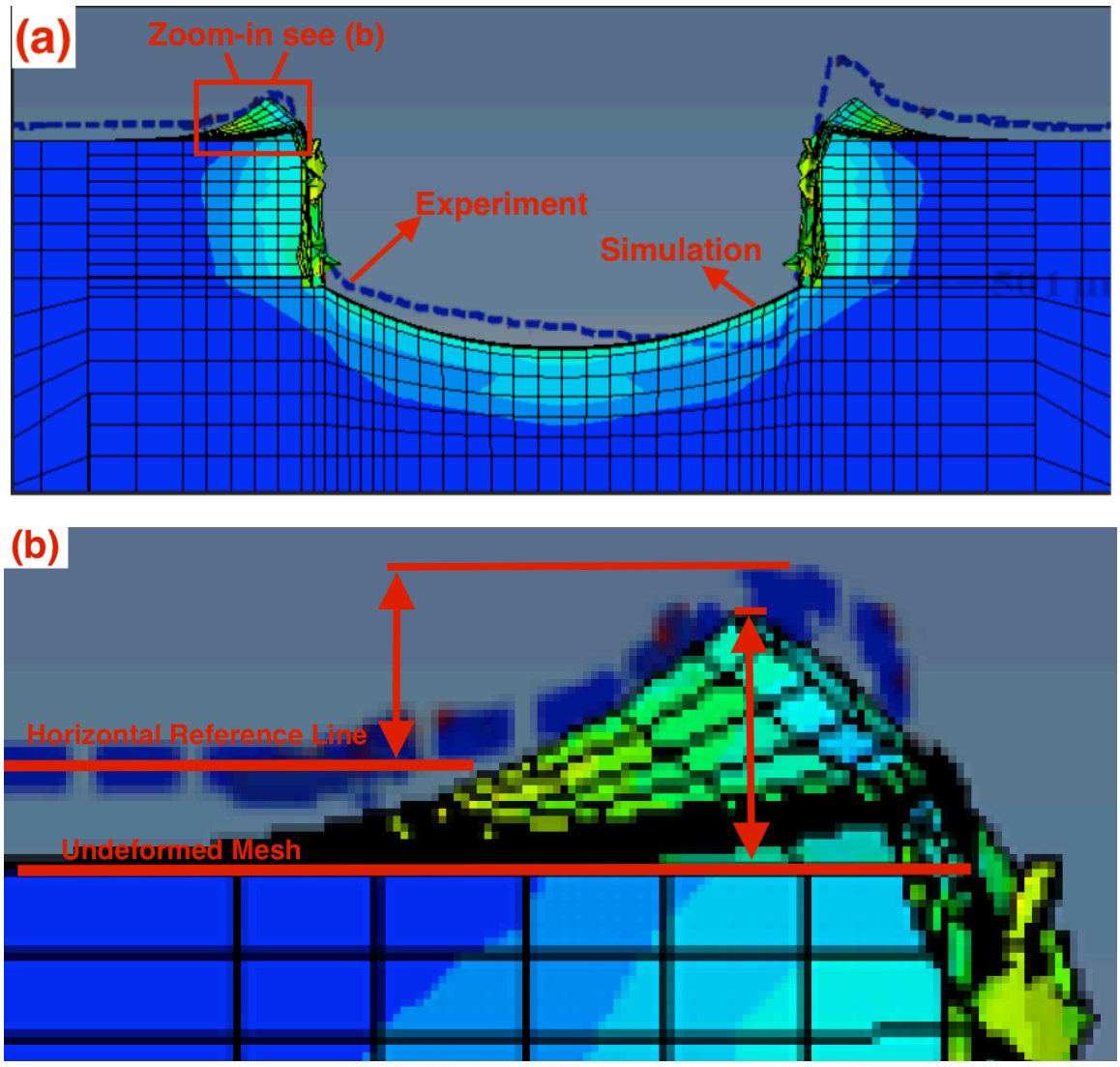

Fig. 4.7 (a) Experimental and simulated micro-groove cross-sections at depth of cut of 0.5µm and cutting speed of 100 mm /min **(b)** Zoom-in

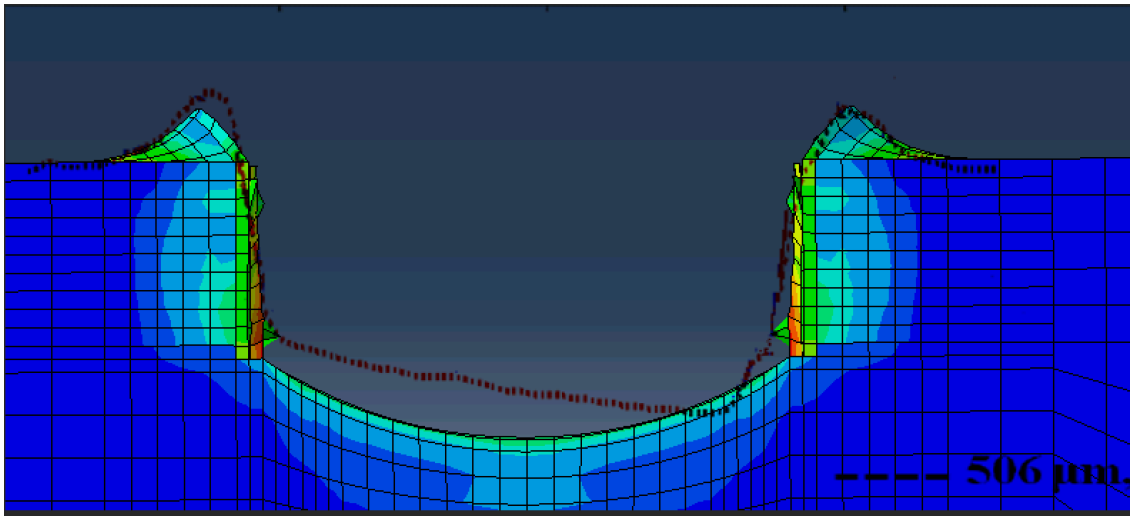

Fig. 4.8 Experimental and simulated micro-groove cross-sections at depth of cut of 0.5µm and cutting speed of 300 mm /min

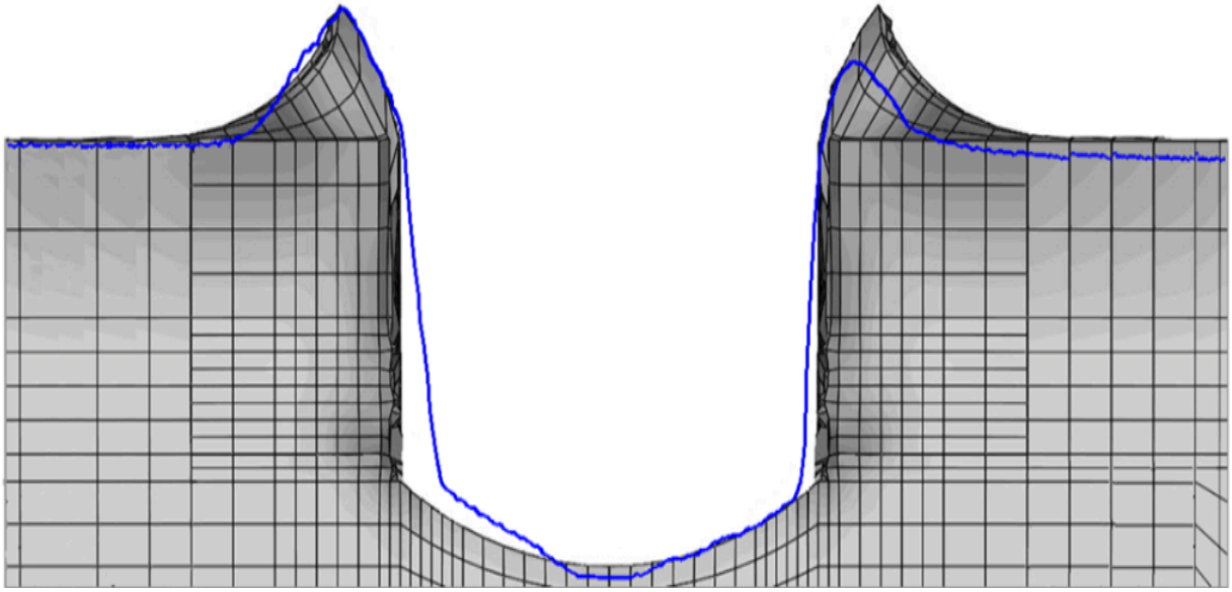

Fig. 4.9 Experimental and simulated micro-groove cross-sections at depth of cut of 0.96µm and cutting speed of 100 mm /min

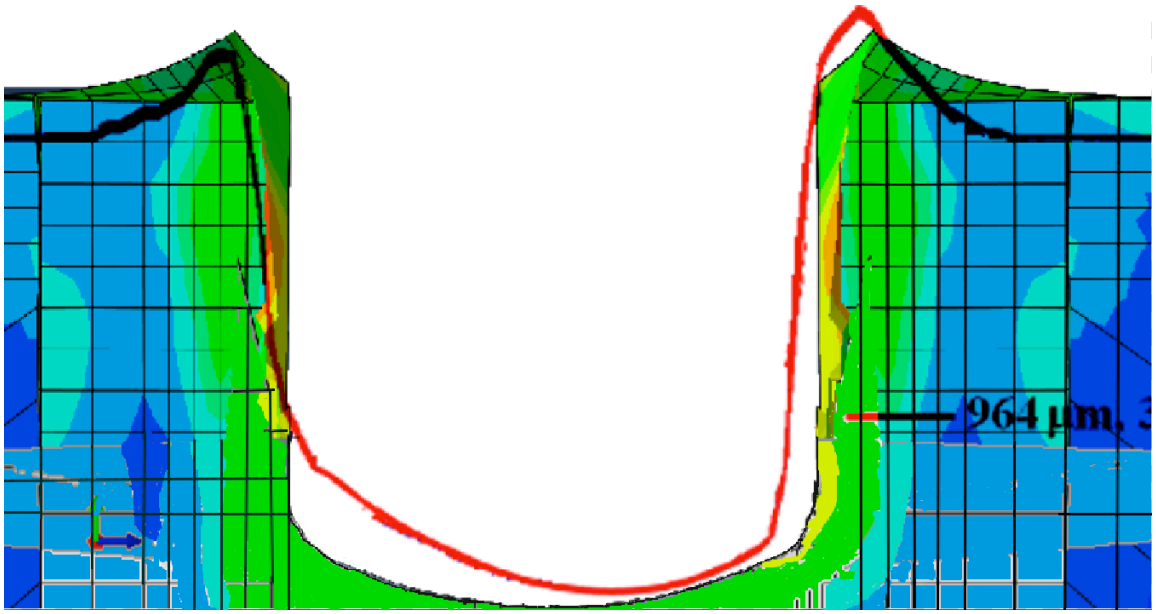

Fig. 4.10 Experimental and simulated micro-groove cross-sections at depth of cut of 0.96µm and cutting speed of 300 mm /min

As shown in the Fig. 4.7 (b), the experimental side burr height is measured as the vertical displacement of highest point on the 2D AFM curve from the horizontal reference line that represents the undeformed surface. Similarly, the simulation burr height is measured from the undeformed mesh at the bottom in the first half of the cross-section, and the other side is obtained by mirroring the image.

The deformed chip thickness values obtained from the simulation are also compared with the experimental values for depths of cut of 0.5 µm and 0.96 µm, cutting speed of 100 mm/min and 300 mm/min, respectively. The schematic of simulated deformed chip looking from the x-y plane at the center of the tool-chip interface is shown in Fig. 4.11, where the chip thickness is denoted as t_c. The experimental chip thickness values are obtained from the SEM images of the chip roots, performed by Raghavendra [1].

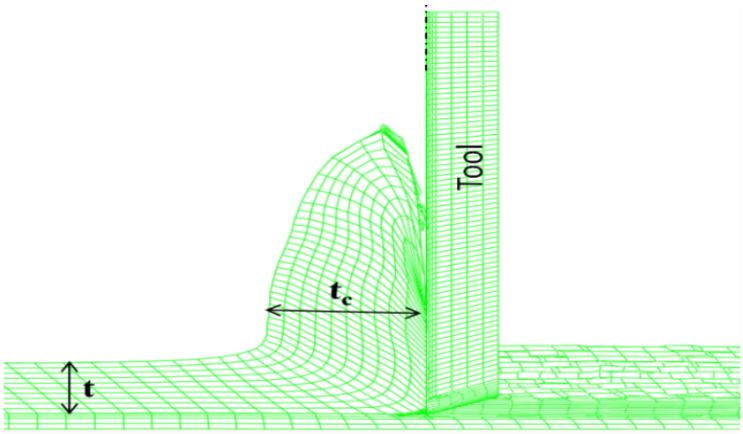

Fig. 4.11 Schematic of deformed chip formation: t_c-deformed chip thickness, t-undeformed chip thickness [1]

Table 4.7 summarizes the simulated and experimental groove characteristics such as chip thickness and side burr height for the depths of cut of 0.5 μm and 0.96 μm, machined with 100 mm/min and 300 mm/min, respectively. It is noted that the depths of cut obtained from the experiments are slightly different from the ones in the simulation due to the machining variation in the experiment. Figure 4.12 physically shows the simulated and experimental chip thickness values. All the simulated values seem to be fairly close to experimental values, except for depth of cut of 0.5 μm and cutting speed of 300 mm/min. As it is shown in the Table 4.7, the chip thickness and side burr height errors between the simulation and experimental values for all the conditions fall under 3.5% and 7% respectively, except for the cutting condition of depth of cut 0.5 μm and cutting speed 300 mm/min. The chip thickness and side burr height values from simulation are particularly closer to the experimental data at the smaller depth of cut and lower cutting speed. However, the chip thickness tends to decrease with increased cutting speed and tends to increase with increased depth of cut. It is also seen from Table 4.7 that the chip thickness values obtained from the simulation are slightly larger than those obtained from

experiment. This is because of the uncertainties associated with the assumed plastic flow and existing variations in the coefficient of friction between the tool-chip interface in the simulations.

Table 4.7 Simulation and experimental deformed chip thickness and side burr height

Exp. Depth of Cut (nm)	Sim. Depth of Cut (nm)	Cutting Speed (mm/min)	Characteristic	Exp. Value	Sim. Value	Enhanced Error	Raghavendra's Error
501	500	100	**Chip Thickness (µm)**	0.95	0.9681	1.87%	18.23%
964	960	100		1.4	1.436	2.51%	6.79%
506	500	300		0.76	0.99	23.23%	36.56%
978	960	300		1.3	1.344	3.27%	4.27%
501	500	100	**Side Burr Height (nm)**	87.108	93.37	6.70%	9.26%
964	960	100		205.18	202.5	1.32%	7.42%
506	500	300		77.91	90.24	15.83%	12.46%
978	960	300		188.199	198.2	5.31%	3.49%

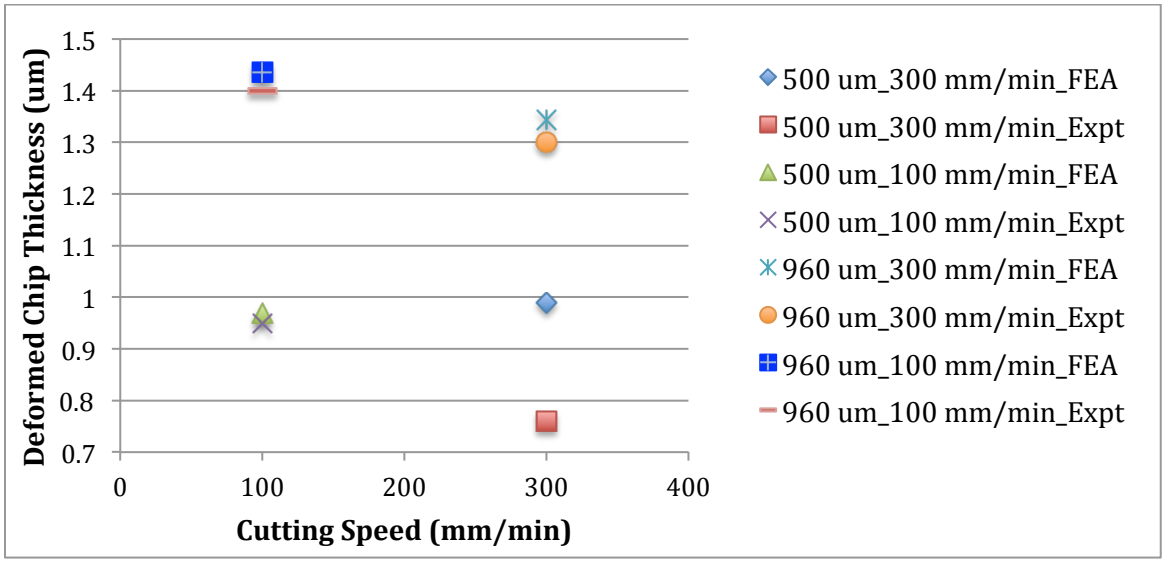

Fig. 4.12 Scattered plot for chip thickness

It is noted in Table 4.7 that the experimental chip thickness data for the different cutting speeds at depth of cut 500 nm varies from 0.96 µm to 0.76 µm while the simulation does not show much variation. The simulation results makes sense because the change in cutting speed

has no effect on the chip thickness t_c formed during the metal cutting, as t_c only depends on friction coefficient μ, rake angle α, and depth of cut DC, as given below [87]:

$$t_c = \frac{DC}{sin\emptyset} \cos(\emptyset - \alpha), \tag{4.1}$$

where shear plane angle $\emptyset$ is given as:

$$\emptyset = 45 + \frac{\alpha}{2} - \frac{tan^{-1}\mu}{2}. \tag{4.2}$$

It is to be noted from Table 4.7 that the error percentage for chip thickness and side burr height for depth of cut 500 nm at cutting speed of 300 mm/min are unexpectedly large, ie, 23% and 15% respectively. More experimental data for these cutting conditions need to be collected in order to understand the discrepancy between the two results.

4.6 Frictional Heat Effect

The goal of this study is to understand the effect of friction heat on the von mises stress, temperature, and cutting force generated during microgroove cutting. Simulation outcomes from the friction heat-enabled model at cutting speed of 100 mm/min and 300 mm/min, rake angles of -5 degrees and 10 degrees, and cutting edge radii of R0 and R60 in total eight cutting conditions, are compared with those obtained from the friction heat-disabled model. Figures 4.13 and 4.15 show the temperature distribution on the workpiece from friction heat-enabled model and heat-disabled model, for the sharp tool machining at 300 mm/min, rake angle 10 degrees, and 60 nm rounded tool at 300 mm/min, rake angle -5 degrees, respectively. Figures 4.14 and 4.16 provide the comparison

of von mises stress distribution on the workpiece between friction heat-enabled model and heat-disabled model for the same cutting condition.

As noticed from the Figs. 4.13 and 4.15, the high temperature (red area) appears at the secondary zone by the tool-chip interface for both models. However, for the model considering the friction heat, the temperature in the secondary zone is higher (red area is larger) and the high temperature band (circled in red in the figures) at the primary zone becomes smaller in the direction towards the shear plane as compared to the model that does not include friction heat. The maximum temeprature found on the tool-chip interface is also found to be larger in the case of friction-enabled model. The reason is that the additional heat generated by the friction at the secondary zone extends the high temperature zone (red area in the figures), while compressing the temperature zone at the primary zone. It is shown in Figs. 4.14 and 4.16 that high stress zone is located in the primary zone for both models. However, with lower temperature caused by neglecting the frictional heat, the softening effect becomes less pronounced and thus von mises stress rises by a small amount and the high stress area tends to expand (circled in red in the figures).

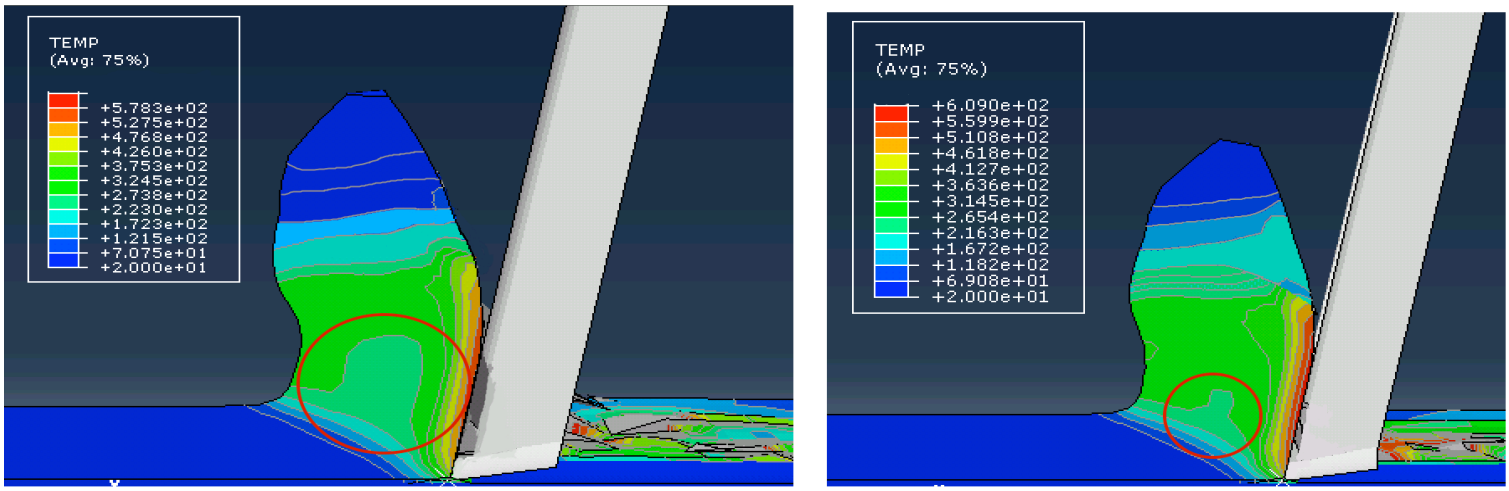

(a) Friction Heat-**Disabled** (b) Friction Heat-**Enabled**

Fig. 4.13 Temperature distribution comparison for sharp tool maching at 300 mm/min, rake angle 10 degrees bewtween friction heat (a) Disabled Model (b) Enabled Model

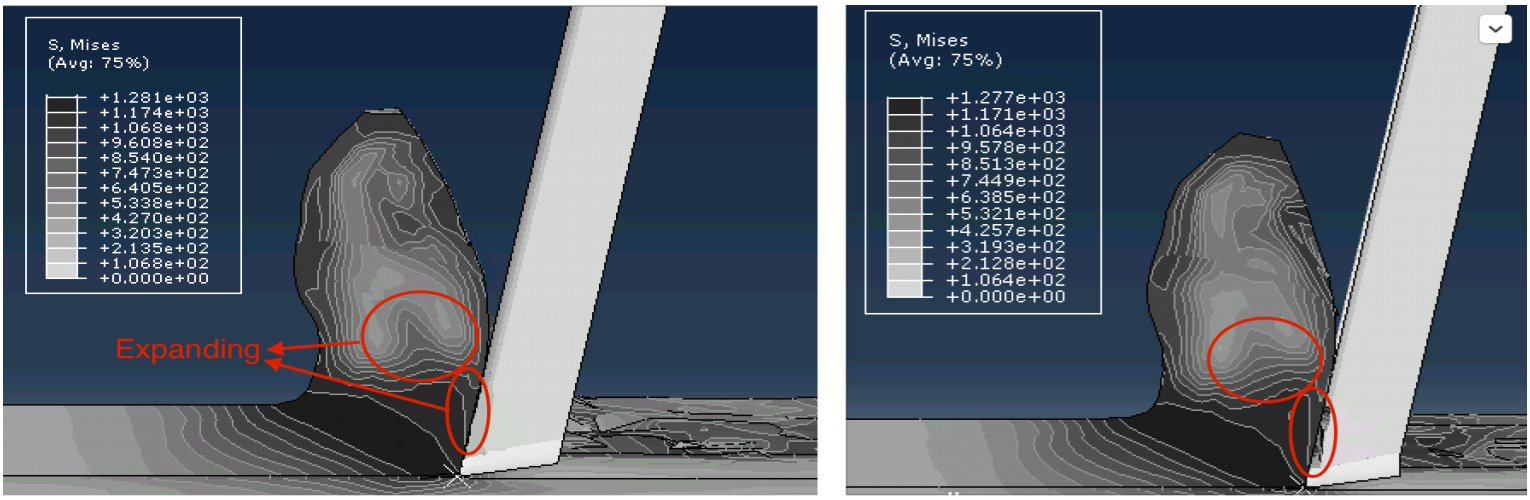

(a) Friction-**Disabled** (b) Friction-**Enabled**

Fig. 4.14 Von mises stress distribution comparison for sharp tool maching at 300 mm/min, rake angle 10 degrees bewtween (a) Friction heat-**disabled** Model (b) Friction heat-**enabled** Model

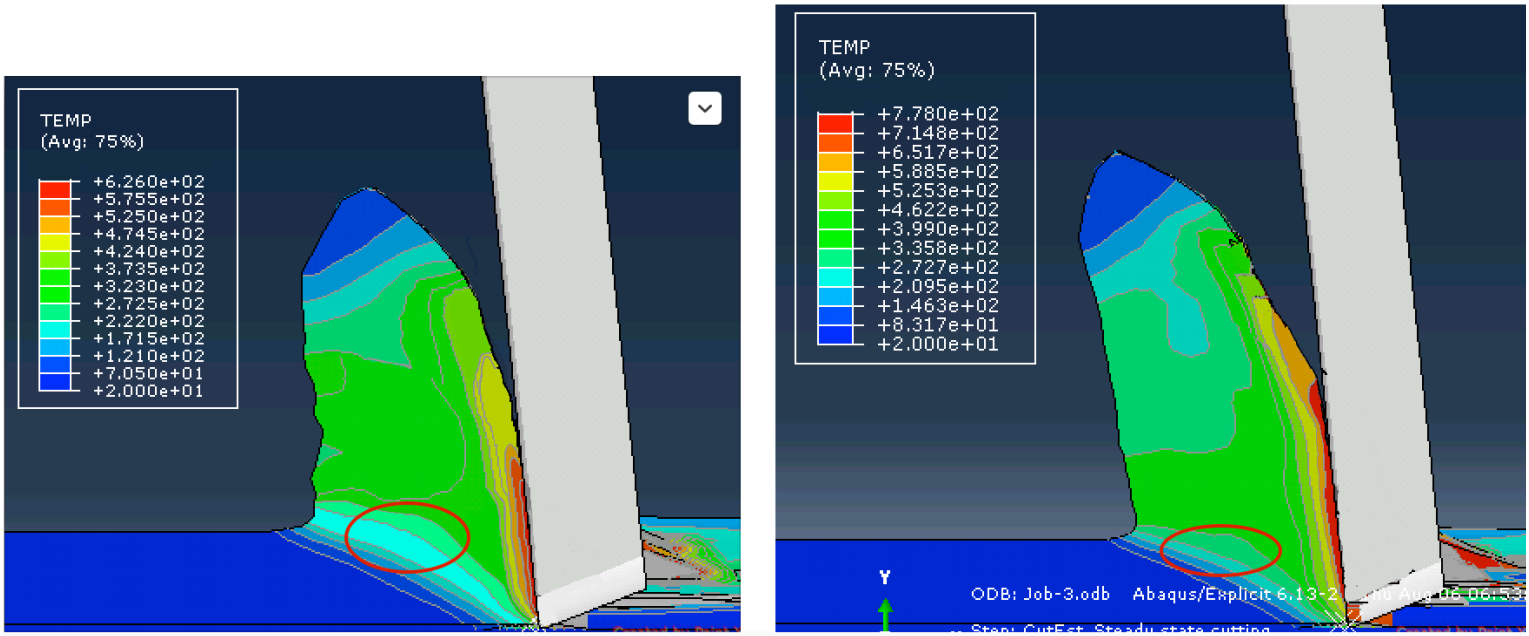

(a) Friction Heat-**Disabled** (b) Friction Heat-**Enabled**

Fig. 4.15 Temperature distribution comparison for 60nm rounded tool maching at 300 mm/min, rake angle -5 degrees bewtween (a) Friction heat-**disabled** Model (b) Friction heat-**enabled** Model

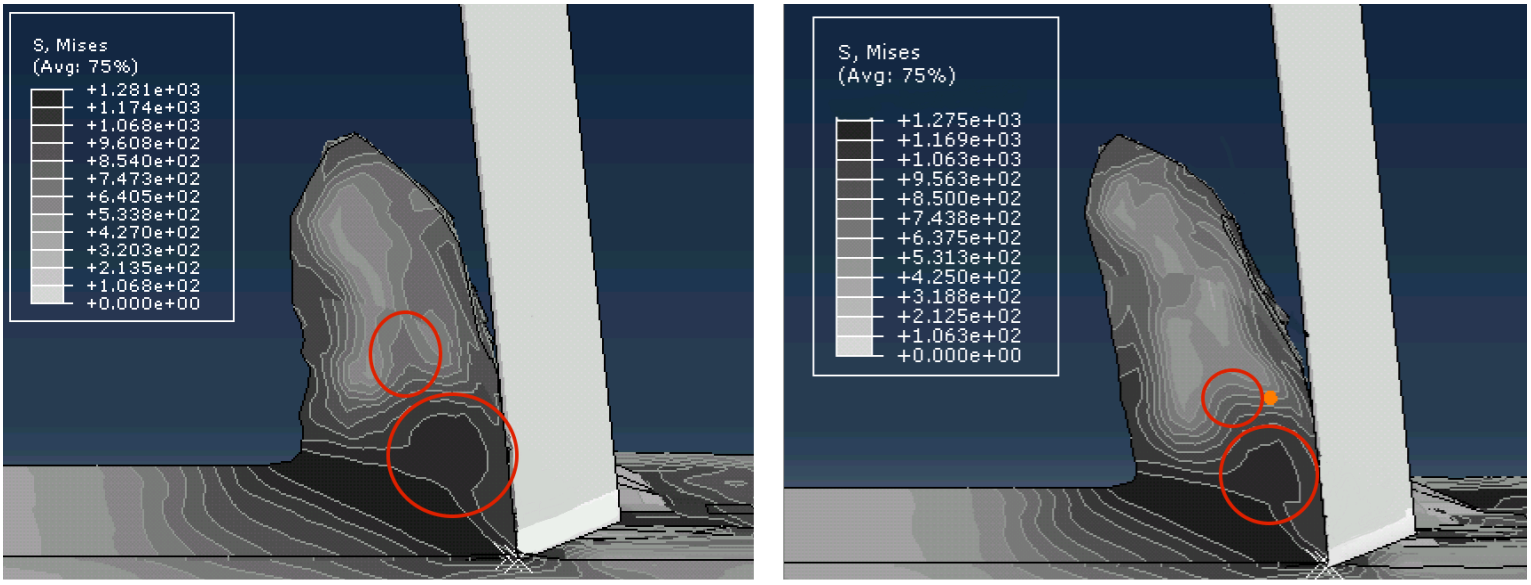

(a) Friction Heat-**Disabled** (b) Friction Heat-**Enabled**

Fig. 4.16 Von mises stress distribution comparison for 60nm rounded tool maching at 300 mm/min, rake angle -5 degrees bewtween (a) Friction heat-**disabled** Model (b) Friction heat-**enabled** Model

The maximum von mises stress, maximum temperature, and steady state cutting force values from the friction heat-enabled and heat-disabled models are shown in the Table 4.8, and the percentage differences between the two models for the three outcomes are shown in the Table 4.9. Von mises stress values from the two models are found to be closer to each other, and the average percentage difference is 0.65%. This is because the von mises stress is dependent upon the material property and the property has a small variation for the small change in temperature. Maximum temperature induced on the chip for the friction heat-enabled model is 16% higher (indicated by the positive sign) on average than the maximum temperature for the heat-disabled model, while the cutting force experienced by the tool on average for the heat-enabled model is 11.35% lower (indicated by the negative sign) than the heat-disabled model. The reason is that the frictional rubbing effect at the tool-chip interface results in large amount of frictional heat, which causes the temperature to rise and the material becomes easier to cut due to the rise in temprature in the primary zone. Thus, disabling friction heat in the model underpredicts the temperature and overpredicts the cutting force.

Table 4.8 Max. temperature, stress, and cutting force values for heat friction enabled and disabled models

Cutting Speed (mm/min)	100				300			
Rake angle (deg)	10	-5	10	-5	10	-5	10	-5
Tool Geometry	R0	R0	R60	R60	R0	R0	R60	R60
Friction Heat-Enabled Results								
Von mises stress (Mpa)	1280	1273	1278	1278	1277	1278	1275	1280
Temperature (C)	590	754	601	768	609	766	613	778
Cutting Force (mN)	0.62	0.76	0.68	0.81	0.59	0.74	0.66	0.78
Friction Heat-Disabled Results								
Von mises stress (Mpa)	1286	1288	1288	1281	1281	1286	1289	1286
Temperature (C)	571	574	572	575	574	580	573	579
Cutting Force (mN)	0.64	0.83	0.74	0.95	0.62	0.82	0.75	0.93

Table 4.9 Percentage difference between heat friction enabled and disabled models

Cutting Speed (mm/min)	100				300				
Rake angle (deg)	10	-5	10	-5	10	-5	10	-5	
Tool Geometry	R0	R0	R60	R60	R0	R0	R60	R60	
% Difference									**Average**
Von mises stress (Mpa)	-0.47	-1.17	-0.78	-0.23	-0.31	-0.63	-1.10	-0.47	-0.65
Temperature (C)	2.77	26.28	4.23	28.18	5.11	27.16	5.84	29.06	16.08
Cutting Force (mN)	-2.84	-9.93	-8.51	-19.86	-4.26	-11.35	-12.77	-21.28	-11.35

The importance of including the friction heat in the model can be further justified by analyzing the chip thickness and side burr height information given in Table 4.10. Using the cutting conditions listed in the Table 4.1, the percentage error (between simulation and experiment) comparison is provided in the table between the friction heat-enabled model and the heat-disabled model performed by Raghavendra [1]. The enhanced model performs better on predicting the chip thickness, as the results that chip thickness percentage errors obtained from enhanced model are on average 8.5% smaller than the errors from Raghavendra's model. The prediction on the side burr height is also improved, as the percentage errors are on average 4.5% lower than the ones from Raghavendra.

Table. 4.10 Comparison between Enhanced and Unenhanced Models for Chip Thickness and Side Burr Height Error Percentages

Sim. Depth of Cut (nm)	Cutting Speed (mm/min)	Characteristic	Enhanced Model Error	Raghavendra's Model Error	Average % Error Difference between Enhanced and Raghavendra's model
500	100	**Chip Thickness**	1.87%	18.23%	-8.5%
960	100		2.51%	6.79%	
500	300		23.23%	36.56%	
960	300		3.27%	4.27%	
500	100	**Side Burr Height**	6.70%	9.26%	-4.5%
960	100		1.32%	7.42%	
500	300		15.83%	12.46%	
960	300		5.31%	3.49%	

4.7 Thermo-mechanical Coupling Effect

As mentioned in Chapter 1, the FEM-based approach can be used to model both thermal and mechanical effects of metal cutting process. The coupling between the thermal model and flow stress model can be accomplished by feeding back the temperature (heat) information to the flow stress model as shown in Fig. 3.1. In this research, this eccentially means that the temperature and mechanical data are exchanged every time a single loop is executed. The details of the coupling algorithm is explained below.

The heat generated from plastic deformation is given by,

$$\dot{q_P} = \eta_P \, \bar{\sigma} \, \dot{\varepsilon}_p, \tag{4.1}$$

which is proportional to $\bar{\sigma}$ von mises flow stress. The flow stress is expressed by Johnson-Cook constitutive flow stress model, and is related to temperature T as,

$$\bar{\sigma} = [\mathrm{A} + \mathrm{B}\ (\varepsilon)^n]\ [1 + \mathrm{D}\ \ln(\tfrac{\dot{\varepsilon}}{\dot{\varepsilon}_p})]\ [1 - (\hat{\theta})^m], \tag{4.2a}$$

$$\hat{\theta} = \begin{cases} 0 & for\ T < T_{transition} \\ \frac{T - T_{transition}}{T_{melt} - T_{transition}} & for\ T_{transition} \le T \le T_{melt} \\ 1 & for\ T > T_{melt} \end{cases} \tag{4.2b}$$

where A is the yield strength, B is the strain hardening coefficient, n is the strain hardening exponent, ε is the equivalent plastic strain, D is the strain rate coefficient, $\dot{\varepsilon}$ is the equivalent plastic strain rate, $\dot{\varepsilon p}$ is the reference plastic strain rate, T is the current temperature, $T_{transition}$ is the transition temperature when softening effect starts to affect the material property, and T_{melt} is the melting temperature.

The flow stress equation implies that when the temprature gets higher, the stress required to deform the material becomes smaller. This is known as thermal softening effect. If the thermal effect is decoupled from the mechanical aspect, ie, if $\hat{\theta}$ is assumed to be zero, there is no softing

effect of the material. It is obivious that stress σ would become larger than the value calculated with the thermal effect when the temperature is above the transition temperature of the material. Thus, according to Equation 4.1, heat energy generated from plastic deformation becomes larger, resulting in a higher temperture in the workpiece.

The temperature variation with and without coupling for two sets of machining conditions are shown in the Fig. 4.17 and 4.18. For the machining condition of cutting speed 300 mm/min, sharp tool edge, and rake angle 0 degree, maximum temperature induced at the tool-chip interface with decoupled model is higher (965 ^{o}C) than the temperature with the coupled model (708 ^{o}C). Similarly, when the cutting condiction is changed to cutting speed of 300 mm/min, cutting edge radius of 60 nm, and rake angle of -5 degrees, temprature obtained from decoupled model is much higher than the temperature from coupled model, ie, 778 ^{0}C vs. 1025 ^{0}C, shown in Figure 4.18. This clearly suggests that the material properties are not updated when the coupling is not modeled and the temperature increases. Table 4.10 summarizes the maximum temperature, von mises stress, and cutting force obtained from the two cutting conditions.

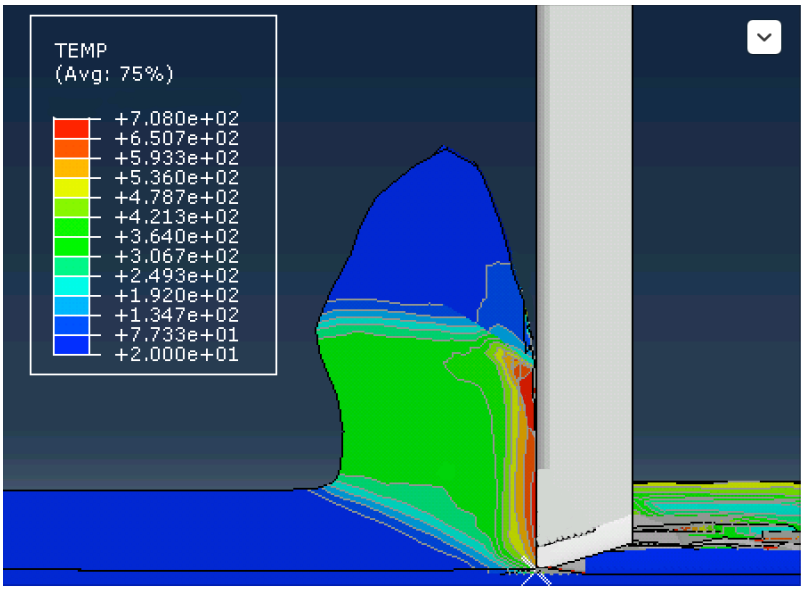

(A) Coupled Temperature Distribution

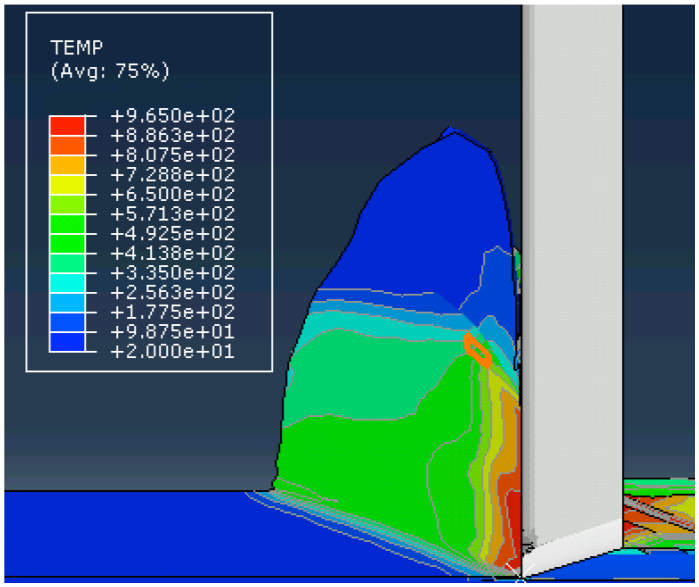

(B) Uncoupled Temperature Distribution

Fig. 4.17 Temperature distribution comparison for cutting conditions of 300 mm/min, R0, and Rake 0 degree (A) Coupled (B) Uncoupled

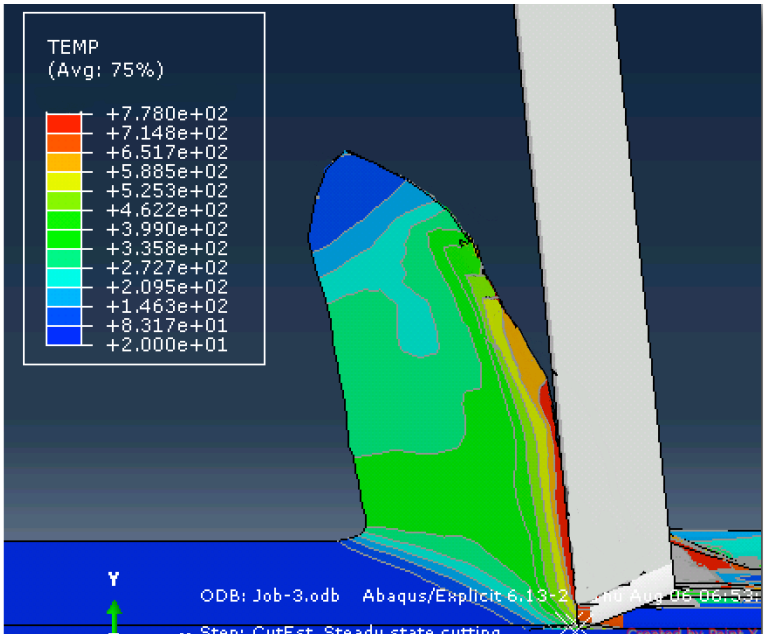

(A) Coupled Temperature Distribution

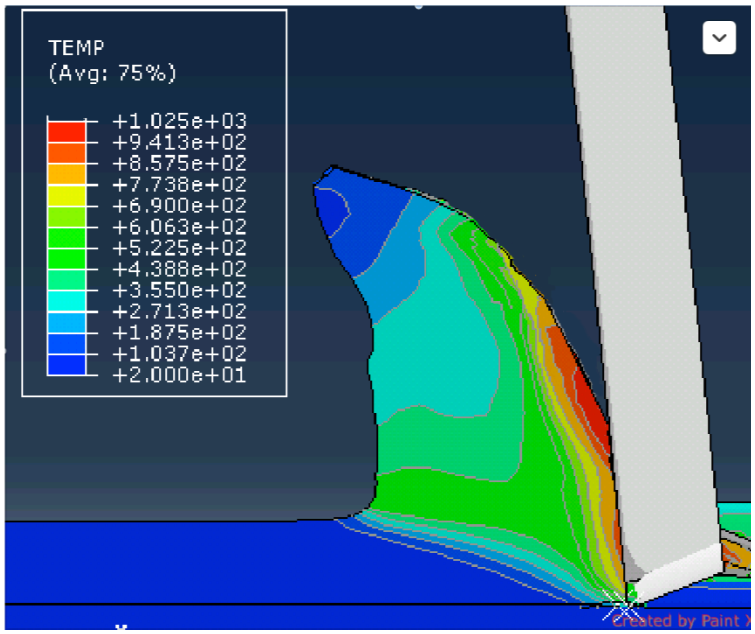

(B) Uncoupled Temperature Distribution

Fig. 4.18 Temperature distribution comparison for cutting conditions of 300 mm/min, R60, and Rake -5 degree (A) Coupled (B) Uncoupled

The stress and cutting force also become higher when the thermal effect is decoupled in the model, as it is indicated in the Table 4.10. The reason is that when the material properties are not updated based on the change in temperature, it causes an increase in the difficulty to cut the material. The table also provides the temperature, stress, and cutting force percentage differences between the thermo-mechanical uncoupled and coupled models for the two different cutting conditions. It shows that decoupling thermal effects from mechanical effect has similar influence on the temperature, stress, and cutting force for different rake angles and tool cutting edges.

Table 4.10 Maximum temperature, stress, and cutting force for coupled and uncoupled models

S (mm/min)	300			
Rake angle (deg)	0		-5	
Tool Edge	R0		R60	
	Coupled	**Uncoupled**	**Coupled**	**Uncoupled**
Max. Temp. (Celsius)	708	960	778	1025
Temp. % Difference	35.6		34.9	
Stress (Mpa)	1277	1650	1280	1641
Stress % Difference	29.2		28.2	
Cutting Force (N)	0.67	0.9	0.78	1.02
Cutting Force % Difference	34.3		30.8	

4.8 Effect of Cutting Speed, Rake Angle and Cutting Edge on Machining Responses

In this section the effects of cutting speed, tool edge geometries, and tool rake angles on the cutting performance such as von mises stress on the workpiece, temperature in the chip, and cutting force experienced by the tool are studied. The cutting speeds used in this study are 100

mm/min and 300 mm/min, tool edge geometries studied here are R0 and R60, and rake angles used here are -5^0 and 10^0, a total of eight different cutting conditions. According to Raghavendra [1], the desired micro-groove features with minimal burr formation, required tolerance, and cutting force are achieved at low depth of cut. Thus, depth of cut of 500 μm is used here. To study the effect of the cutting condition on the machining responses, two studies are conducted. In the first study, the stress, temperature distributions that are captured once the steady state condition is reached, and the cutting force time plot during machining are studied. Simulations are carried for two cutting speeds for a given rake angle of 0^o and sharp tool. Similarly, to study the effect of rake angle two rake angles are used for a given cutting speed of 300-mm/min and tool cutting edge of R60. To study the effect of tool cutting edge, two edge geometries are used for a given cutting speed of 300 mm/min and rake angle -5^o. In the second study, the maximum stress, temperature, and steady-state cutting force obtained during the steady state cutting period are selected for the study.

(a) Temperature, stress distribution, and cutting force

Cutting Speed

Figure 4.19 shows the temperature distribution on the chip for the cutting speeds of 100 mm/min and 300 mm/min. The high temperature zone occurs in the secondary shear zone next to the tool-chip interface, shown as the red area in Fig. 4.19. For a higher cutting speed, high temperature zone seems to penetrate deeper into the chip indicated by the red circled areas in the figure. As the tool moves faster, the rate of the failure for the cut-chip and the rate of frictional shearing become higher and hence the strain rate becomes higher, resulting in a higher maximum

temperature for the higher cutting speed, as shown in Fig. 4.19 (590 degree celsius for 100 mm/min vs. 609 degree celsius for 300 mm/min).

Figure 4.20 shows the cutting force variation with respect to time for the two cutting speeds. The oscillations of the cutting force shown in the plots are resulted from discrete finite element failure in the 3D FEA model during chip separation sequence and are not expected in the actual cutting process [1]. Apparently, the process with a slower moving cutting tool takes longer time to reach the steady state of 1.3 ms than the process with faster moving tool of 0.46 ms.

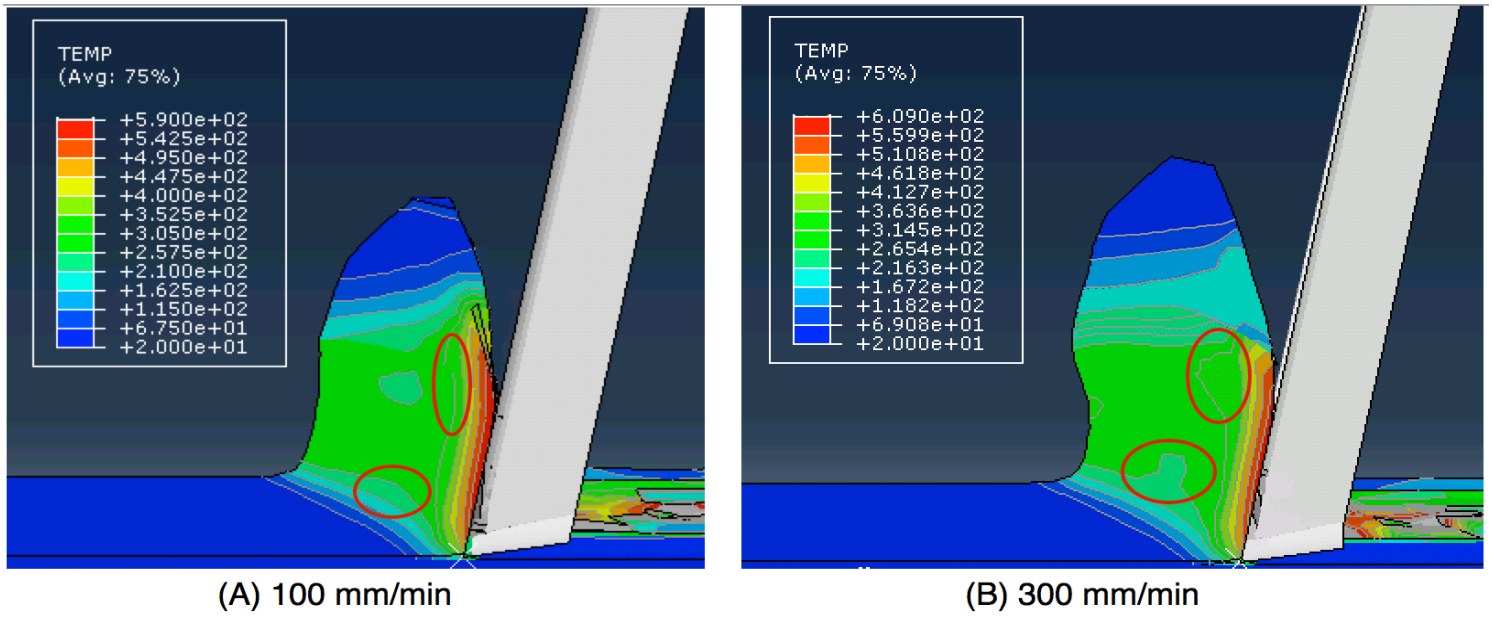

(A) 100 mm/min (B) 300 mm/min

Fig. 4.19 Temperature distribution for sharp tool and rake angle 10 degree at cutting speeds of (A) 100 mm/min; (B) 300 mm/min

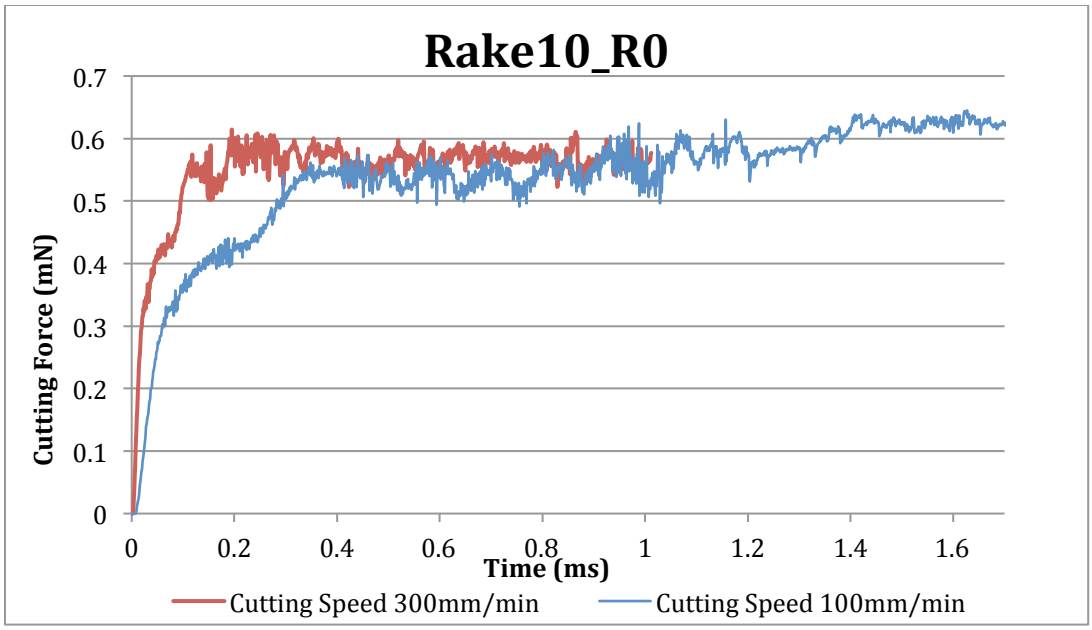

Fig. 4.20 Cutting force vs. time for sharp tool and rake angle 10 degree at cutting speeds of 100 mm/min and 300 mm/min

Figure 4.21 shows the von mises stress distribution on the workpiece for cutting speed of 100 mm/min and 300 mm/min, respectively. Shown as the dark area in the figure, high stress zones are concentrated at the primary shear zone. It is also seen from Fig. 4.21 that the distributions of the von mises stress for the two cutting speeds are similar to each other.

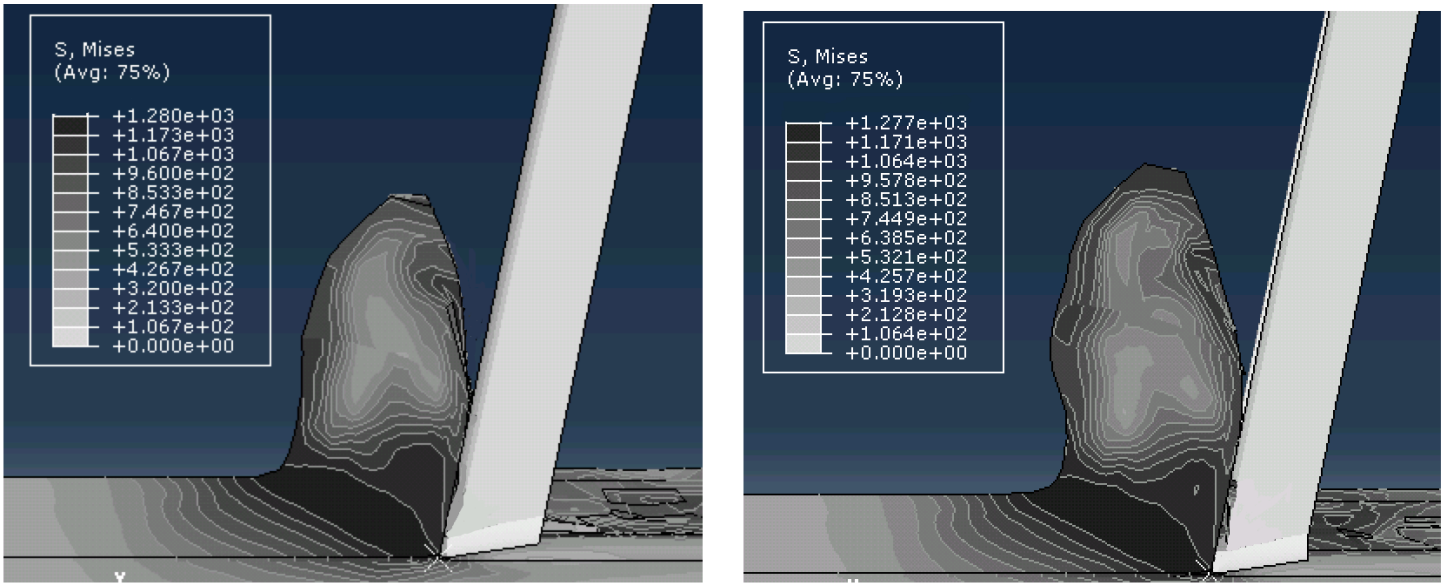

Fig. 4.21 Von mises stress distribution for sharp tool and rake angle 10 degree at cutting speeds of (A) 100 mm/min; (B) 300 mm/min

Tool Rake Angle

The rake angles investigated here are -5^{o} and 10^{o}. The other conditions are cutting speed of 300 mm/min, and tool cutting edge of R60. The temperature distributions in the chip are shown in the Fig. 4.22 for the two tool rake angles. The maximum temperature value and the high temperature zone next to the tool-chip interface tend to increase with the decrease in tool rake angle because there is more heat generated by the sliding friction due to the increased tool-chip contacting area (indicated in the red circles). Moreover, the medium temperature area (green area circled in black in the figure) next to the secondary zone becomes larger for the -5-degree rake angle as compared to the 10-degree rake angle, due to more frictional heat generation at the tool-chip interface. The maximum temperature obtained from the chip cut at -5^{0} is over 100 ^{0}C higher than the temperature from rake angle 10^{0}, as observed from Fig. 4.22.

Cutting force experienced by tool vs. time plots at rake angles of -5° and 10° are shown in Figure 4.23. The cutting force ramps up from zero and climbs up to a maximum value, then drops down slowly and stays stable after reaching the steady state. The reason of overshooting is due to the rubbing effect. The difficulty to cut the material due to more supporting matrial resulted from the larger contacting area between the tool-chip interface makes the cutting force increase. As indicated in Fig. 4.23, the tool at rake angle of -5^0 experiences a larger cutting force at the steady state condition. In addition, the cutting force for both rake angles reaches steady state at about 0.45 ms.

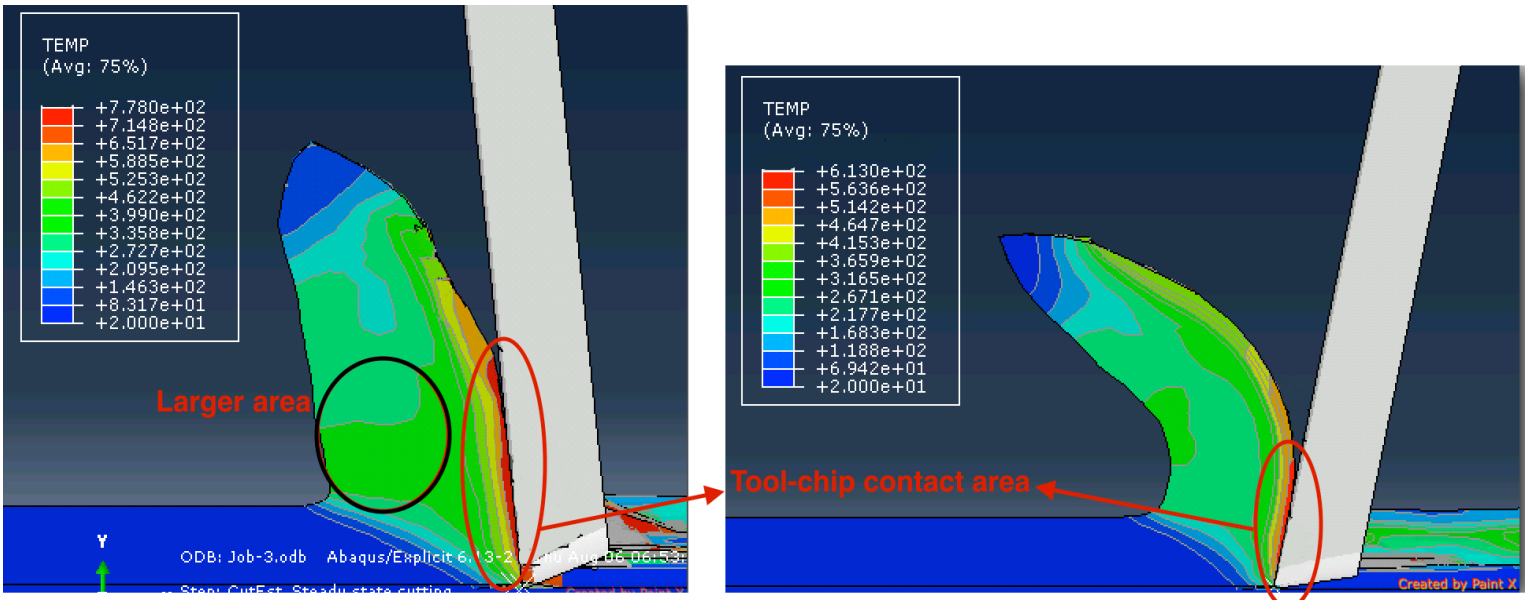

(A) Rake Angle -5 Degree (B) Rake Angle 10 Degree

Fig. 4.22 Temperature distribution at symmetry plane at rake angles of (A) -5^0, (B)10^0

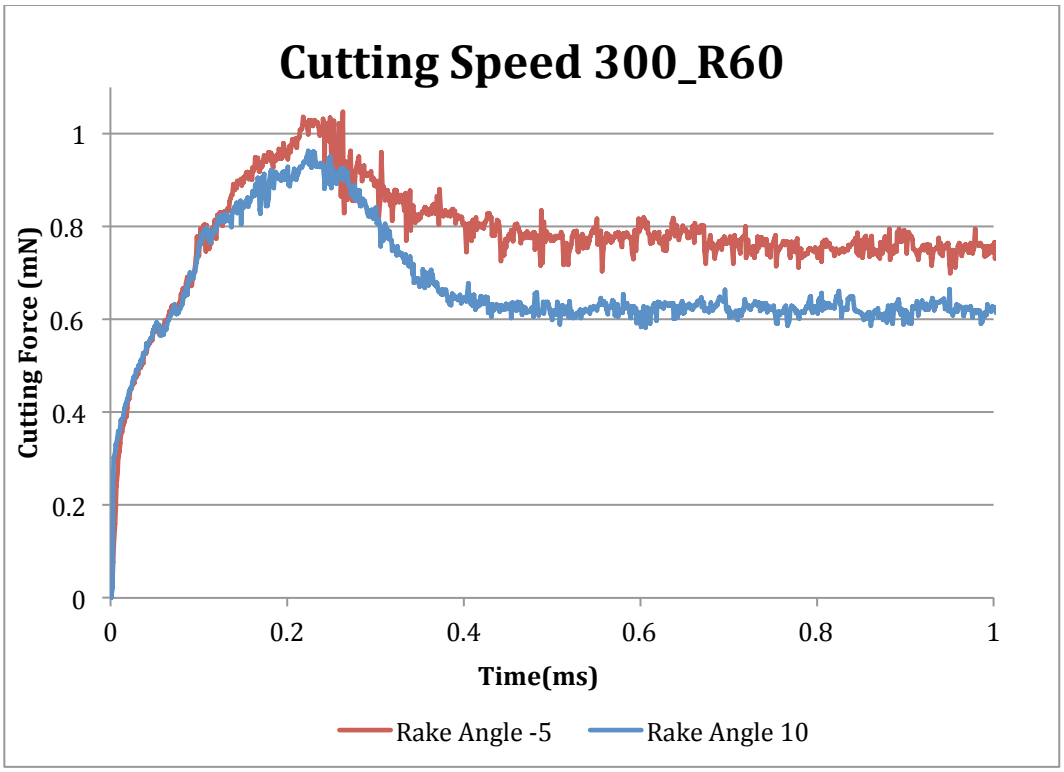

Fig. 4.23 Cutting force analysis for rake angles -5^{o} and 10^{o}

Fig. 4.24 shows the von mises stress distributions for tool rake angles of -5^{o} and 10^{o}. The maximum stresses for the two tool rake angles seem to be very close. However, high stress area tends to move towards the tool tip and penetrates deeper into the workpiece as the tool rake angle gets smaller. This is further seen from figures (A) and (B), where the distortion of meshed elements cut by the tool tip becomes higher as the tool angle decreases. The high stress area becomes larger as rake angle is decreased as shown as the red-circled area in the figure. In addition, chip shape is found to be less curly with decrease in the rake angle, resulting in a larger tool-chip contacting area for the smaller tool rake angle.

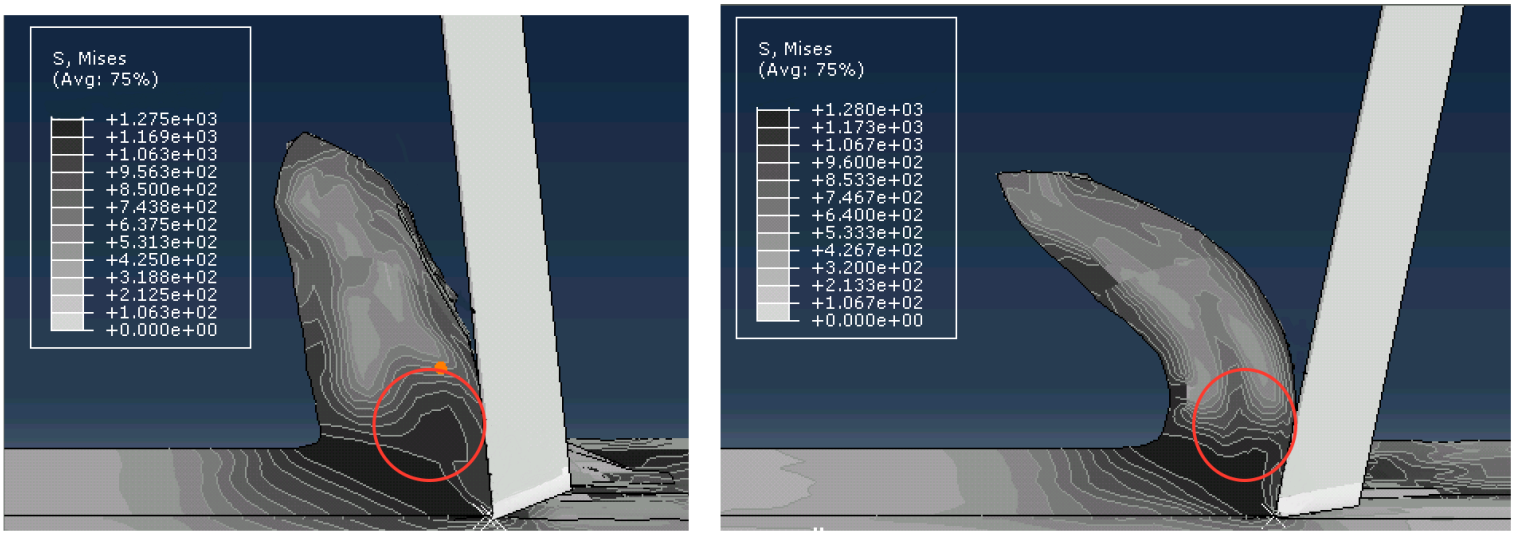

(A) Rake Angle -5 Degree (B) Rake Angle 10 Degree

Fig. 4.24 Von Mises stress analysis at symmetry plane at rake angles of (A) -5^0; (B) 10^0

Tool Cutting Edge Geometry

The comparison between tools with sharp edge (R0) and R60 is discussed here. For both tools, the simulation was run for cutting speed of 300 mm/min and rake angle of -5 degrees. Rounded tool produces more supporting area between the rounded cut tip and the workpiece as compared to sharp tool, shown in Figure 4.25. The von mises stress distributions for the two different tool edge geometries are shown in Fig. 4.26. The sharp and rounded tools result in similar maximum stress values. However, for the rounded tool, the high stress area by the primary zone is larger comparing with the sharp tool, indicated by the red circles in the figure, due to more supporting material. The temparature distributions in the chip obtained from the enhanced model for the two tool cutting edge geometries are shown in the Figure 4.27. The maximum temperature obtained using the rounded tool is slightly higher since the contact area between the tool tip and the workpiece becomes larger for the rounded tool shown in Fig. 4.25,

causing the the normal and shear pressure at the primary zone to rise, and hence the frictional heat increases.

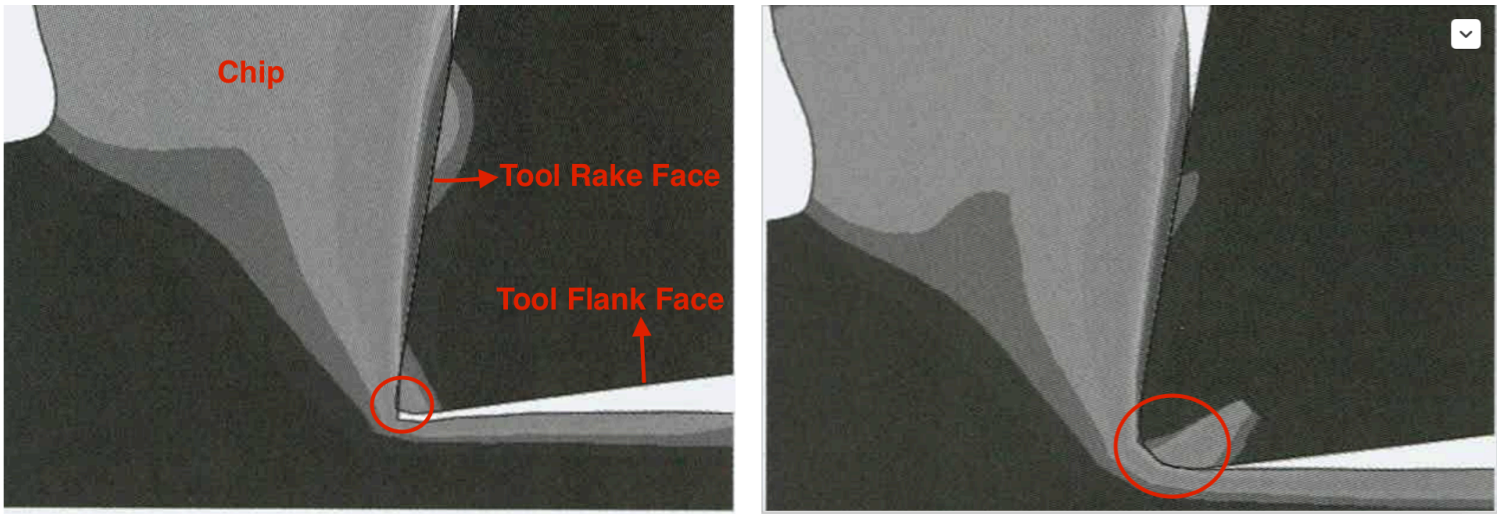

Fig. 4.25 Tool tip contacting area made with workpiece for (a) Sharp tool; (b) Rounded tool

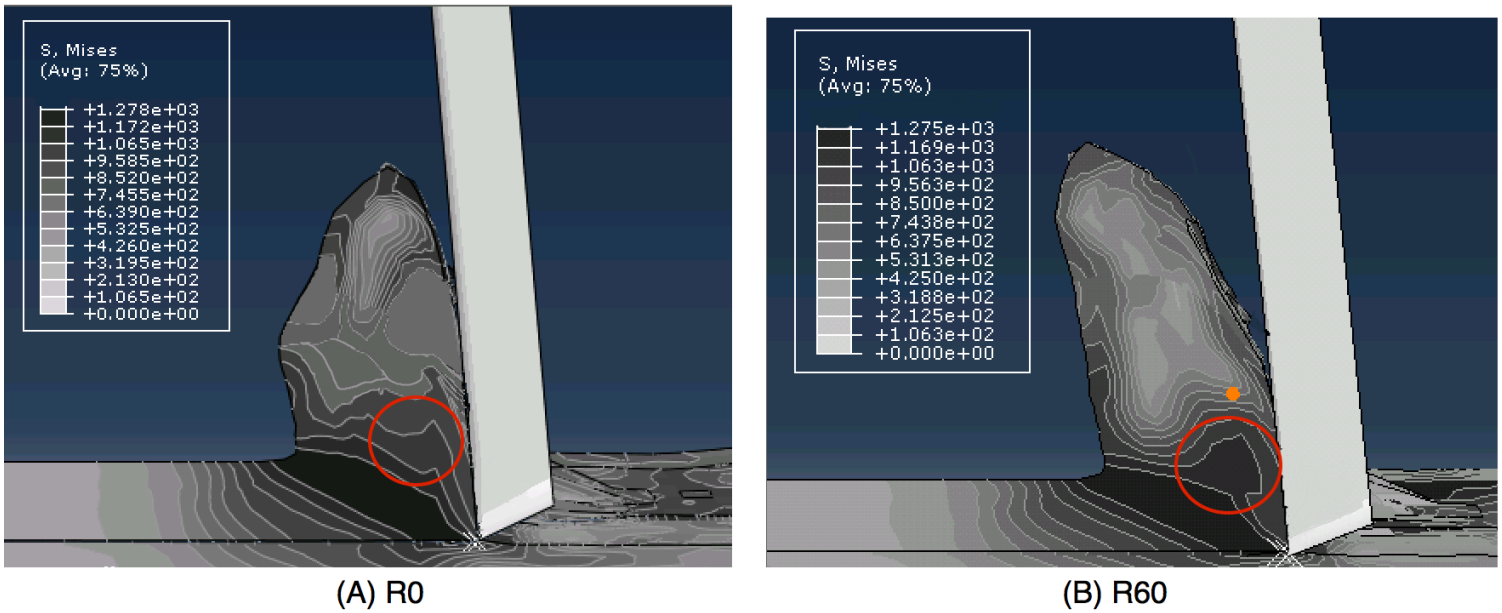

Fig. 4.26 Von Mises stress (Mpa) at steady state cutting for: (A) Sharp Tool; (B) Round tool of edge radius 60 nm

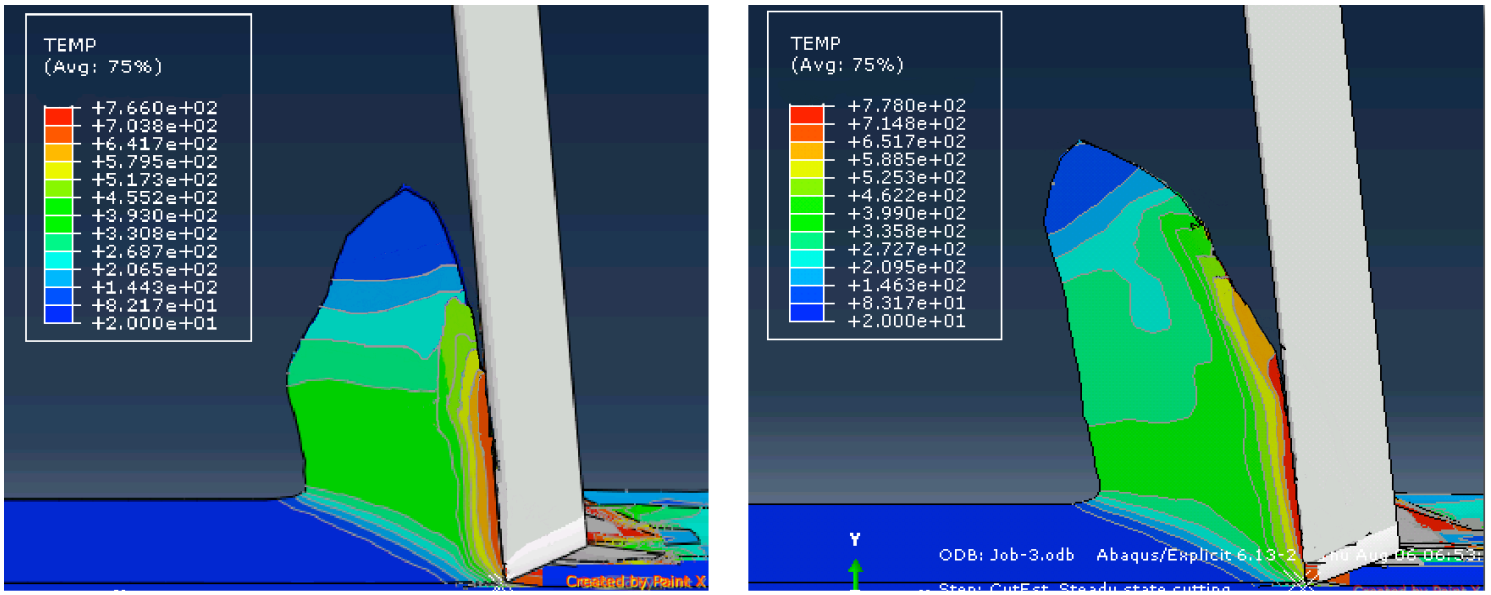

(A) R0 (B) R60

Fig. 4.27 Temperature distribution around the tool-chip interface for: (A) Sharp Tool; (B) Round tool of edge radius 60 nm

According to Figure 4.28, the tool with sharp cutting edge experiences a lower cutting force at the steady state period than the tool with rounded edge. The reason is that the bluntness of the rounded edge creates more difficulty cutting the material in comparison to the sharp tool, which requires larger material shearing and ploughing forces, hence leading to higher stress zone. In addition, there is a rise in cutting force before reaching the steady-state period while sharp tool does not show this peak. This is caused by the rubbing effect due to the bluntness of the rounded tool. Tool is pushing and deforming the material instead of cutting during the tool entry period in the beginning of the cutting.

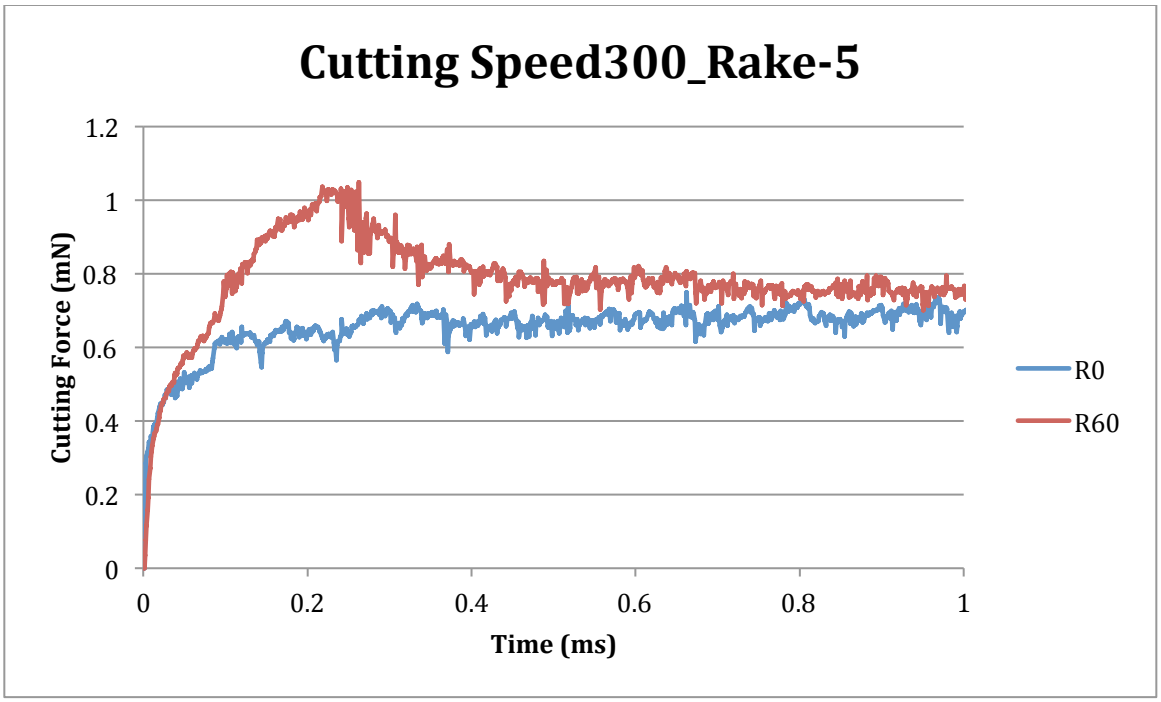

Fig. 4.28 Cutting force for different tool edge radii

(b) Parametric Analysis

The effects of cutting speed, rake angle, and edge radius on the maximum temperature and steady-state cutting force values are studied in this section by analyzing the data obtained from all eight simulations, as discussed earlier. Table 4.11 provides the maximum von mises stress, temperature, and steady-state cutting force values for all eight simulations. It is seen from Table 4.11 that, tool with edge R0 and rake angle -5^0 moving with 100 mm/min causes the smallest maximum von mises stress of 1273 Mpa. The tool with edge geometry R0 and rake angle 10^0 moving with 100 mm/min generates the lowest maximum temperature of 590 ^{0}C, while the tool with edge geometry R0 and rake angle 10^0 moving with 300 mm/min experiences the smallest steady-state cutting force of 0.57 mN. The von mises stresses obtained from all the cutting conditions are close to each other thus temperature and the cutting force are the two main

machining responses for choosing the machining condition. As seen from Table 4.11, the two machining conditions for which either the maximum temperature is the lowest or the steady state cutting force is the smallest, include a sharp tool with 10^{o} rake angle. If the goal is to maximize the material removal rate, a cutting speed 300 mm/min might be preferable.

Table 4.11 Maximum Von Mises stress, temperautre and steady-state cutting force values for all cutting conditions

Cutting Speed (mm/min)	100				300			
Rake angle (deg)	10	-5	10	-5	10	-5	10	-5
Tool Geometry	R0	R0	R60	R60	R0	R0	R60	R60
Results								
Von mises stress (Mpa)	1280	1273	1278	1278	1277	1278	1275	1280
Temperature (^{o}C)	590	754	601	768	609	766	613	778
Cutting Force (mN)	0.60	0.74	0.68	0.81	0.57	0.72	0.63	0.75

Figures 4.29 and 4.30 show the maximum temperature and steady-state cutting force, respectively, vs. cutting speed plots for four different cutting conditions. The amounts of increase in maximum temperature and decrease in cutting froce caused by the increase in cutting speed seem to be insignificant for the four cutting conditions since the lines are almost horizontal. The variation for the slop of the lines is due to the tool with different geomertries used. On the other hand, there is a big jump in the temperature plot (Fig. 4.29) from a large to a small rake angle and big variation in the cutting force plot for different tool cutting geometries (rake angle and edge radius).

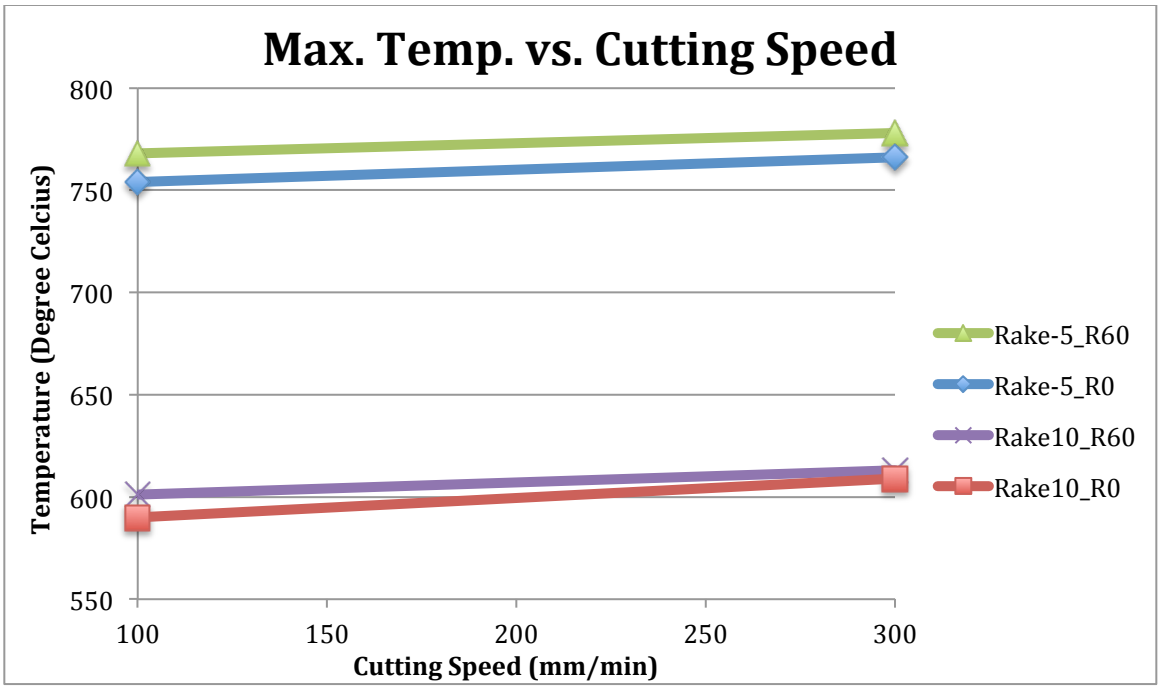

Fig. 4.29 Maximum temperature vs. cutting speed for different tool edges and rake angles

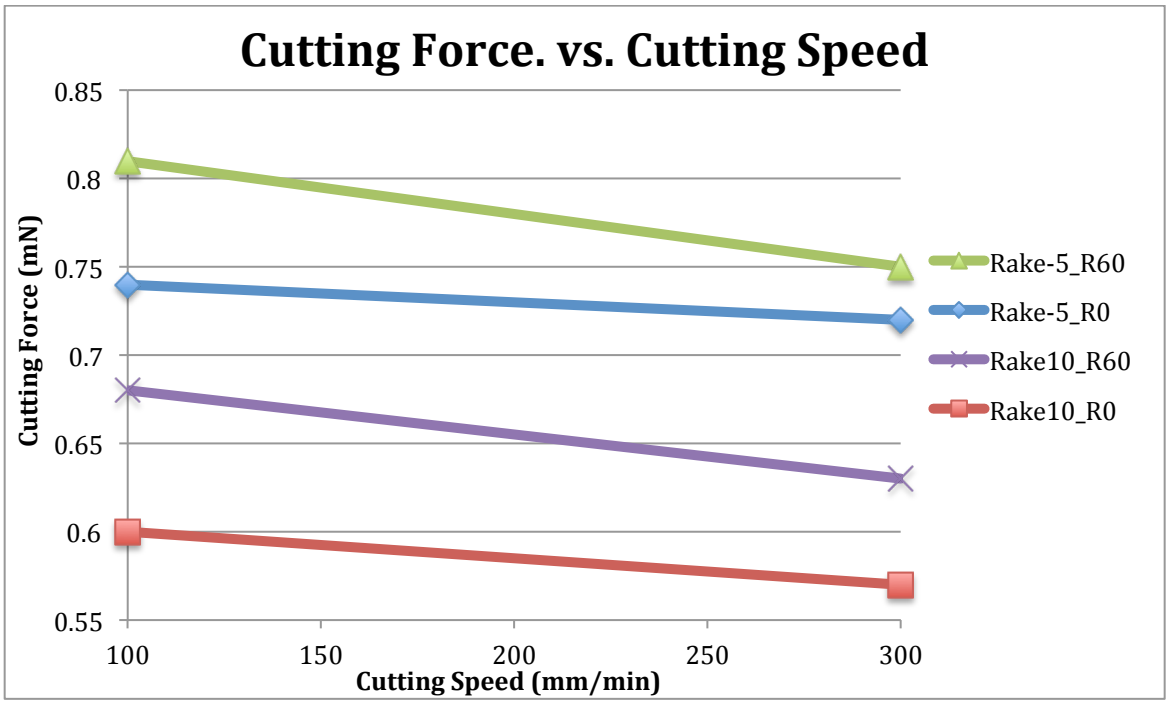

Fig. 4.30 Steady state cutting force vs. cutting speed for different tool edges and rake angles

This can also be found from the Figs 4.31 and 4.32 that display the plots of the maximum temperature and the steady-state cutting force respectively, with respect to rake angle. For all the four cutting conditions the maximum temperature and the steady-state cutting force have large and indentical drops due to the increase in rake angle, indicating that the tool with -5 degrees rake angle generates much more heat and encounters much more difficulty cutting the material than the tool with 10 degrees rake angle. The change in rake angle has bigger influence on the temperature than the change in the edge radius and cutting speed as seen by tiny gap between the steep linear lines for four different cutting conditions. In addition, the maximum temperature plots for the cutting condition of sharp tool at 300 mm/min, and the cutting condition of rounded tool at 100mm/min almost coincide with each other because each of the cutting conditions contains a factor that makes heat generation increase. These factors are faster cutting speed and rounded tool, respectively. According to Fig. 4.32, the decrease in steady-state cutting force due to the increase in the rake angle is a little larger when the sharp tool is used in comparison to the rounded tool.

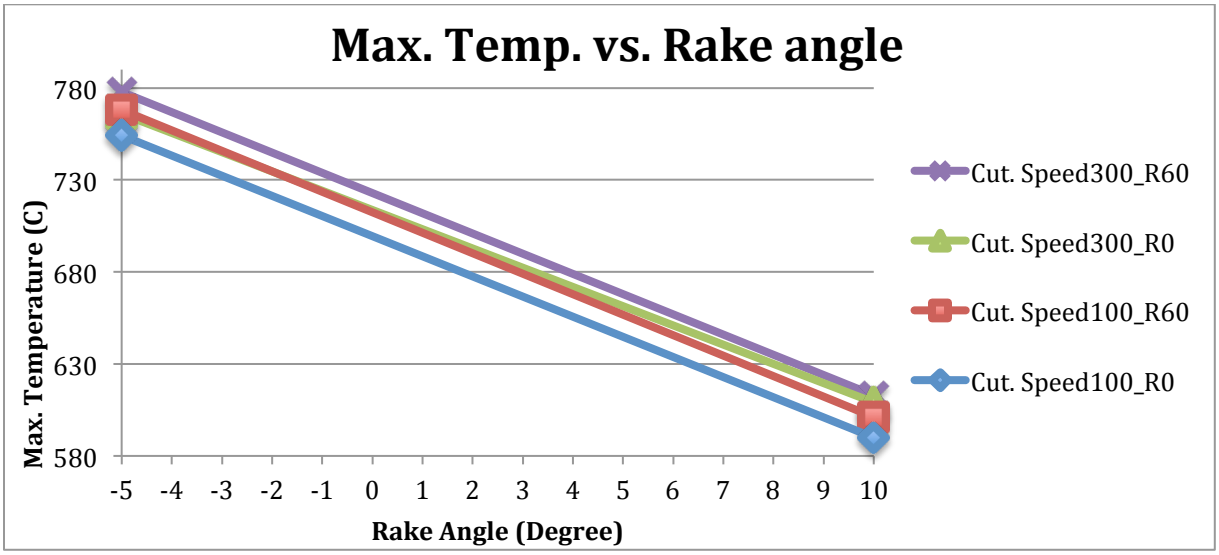

Fig. 4.31 Maximum temperature vs. rake angle for different cutting speeds and tool edges

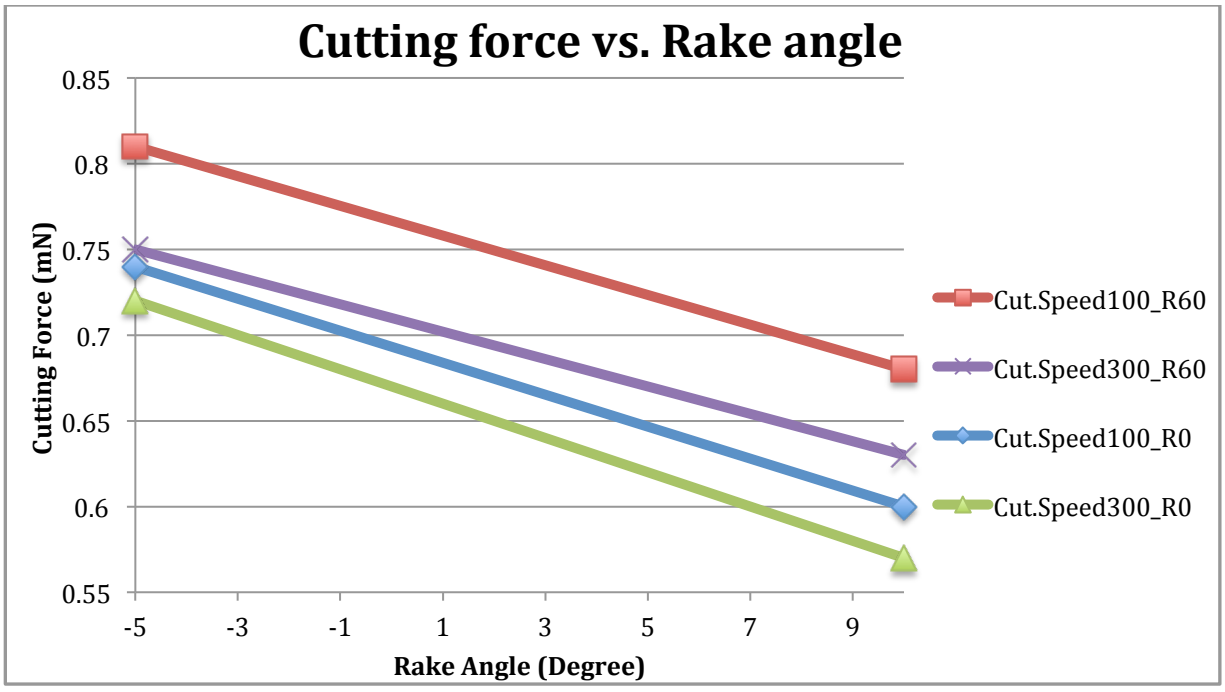

Fig. 4.32 Steady state cutting force vs. rake angle for different cutting speeds and tool-edges

The maximum tempeature and steady-state cutting force vs. cutting edge plots for four different cutting conditions are shown in Figs. 4.33 and 4.34, respectively. For a given cutting speed and tool rake angle, the edge radius does not affect the maximum temperature in the cut-chip. Moreover, for all the cutting conditions studied here, rounded tool induces a significantly higher cutting force than the sharp tool, as seen from Figure 4.34. In addition, the variation of the cutting force for the increase in tool edge radius seems to be smaller for the cutting tool moving with 300 mm/min, in comparison to 100 mm/min, shown in the figure, because the rounded tool that moves faster generates more frictional heat and hence cuts material easily.

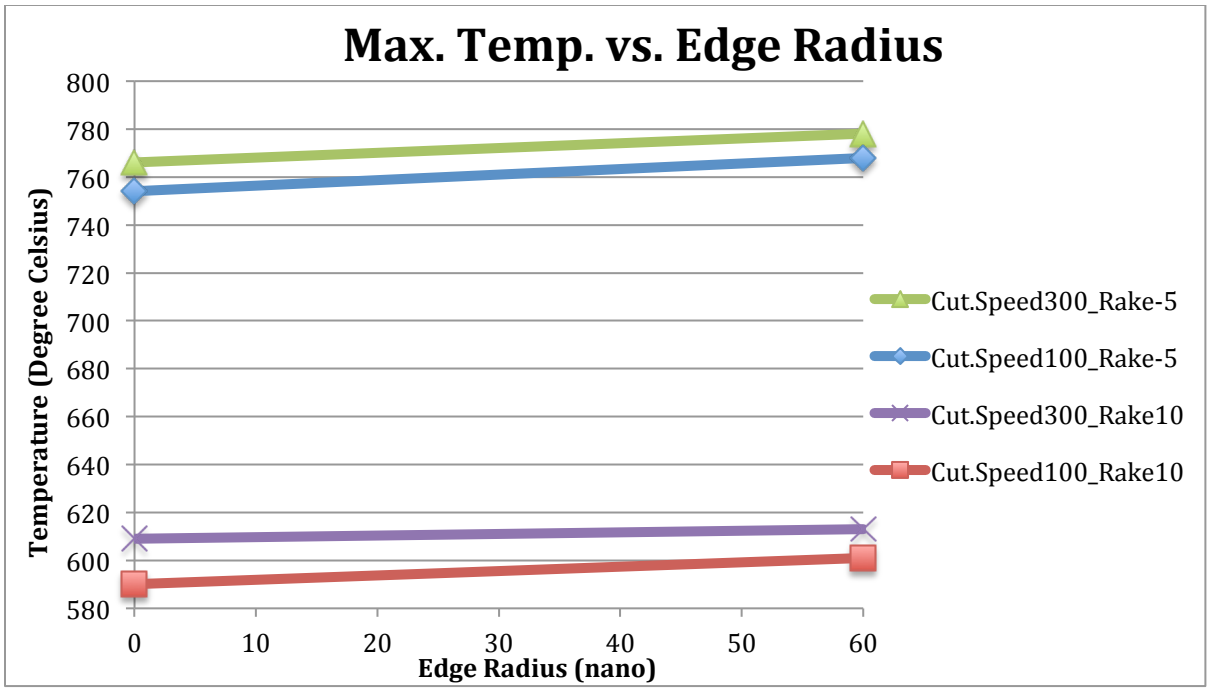

Fig. 4.33 Maximum temperature vs. edge radius for different cutting speeds and rake angles

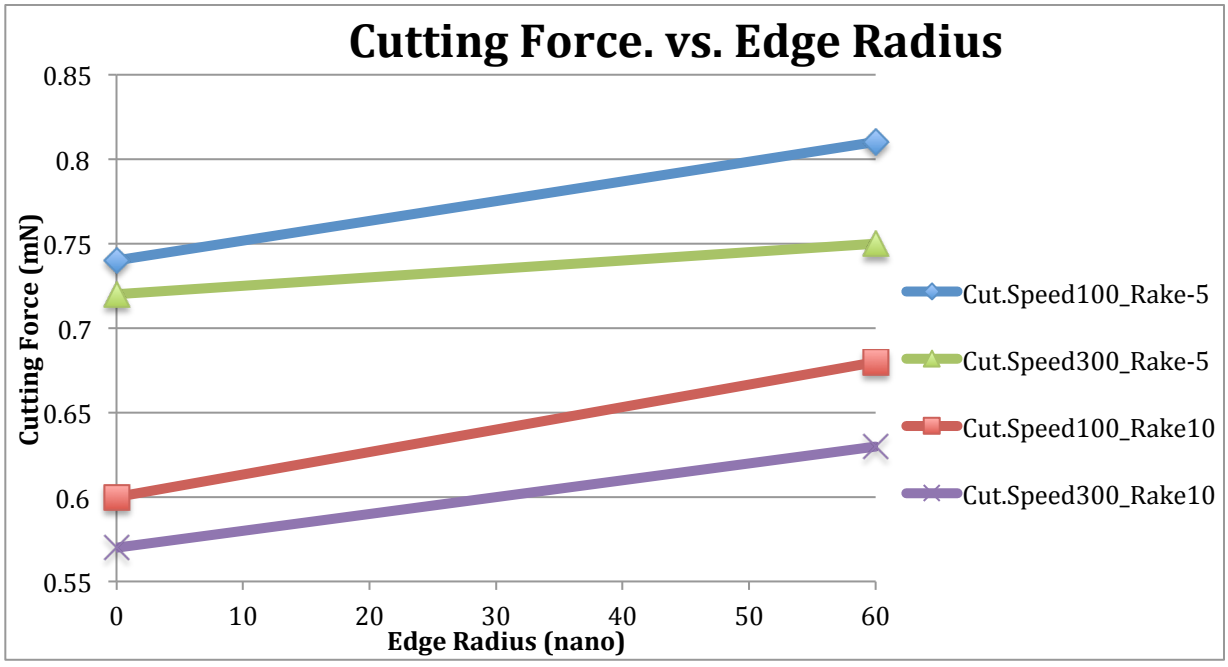

Fig. 4.34 Cutting force vs. edge radius for different cutting speeds and rake angles

Machining with different cutting condition gives different performance on the side burr height, as shown in Table 4.12. Figure 4.35 provides the side burr formation for the cutting conditions of R60 tool at cutting speed of 100 mm/min, rake angle of 10 degrees, and R60 rounded tool at cutting speed of 300 mm/min, rake angle of -5 degrees. The first cutting condition produced a side burr height of 69.5 μm, while the height obtained from the second cutting condition was found to be 122.7 μm, .

Table 4.12 Side burr heights for all cutting conditions

Cutting Speed (mm/min)	Rake Angle (degree)	Edge Radius (nm)	Side Burr Height (nm)
100	-5	R0	108.8
		R60	122.0
	10	R0	72.3
		R60	69.5
300	-5	R0	104.5
		R60	122.7
	10	R0	75.2
		R60	69.6

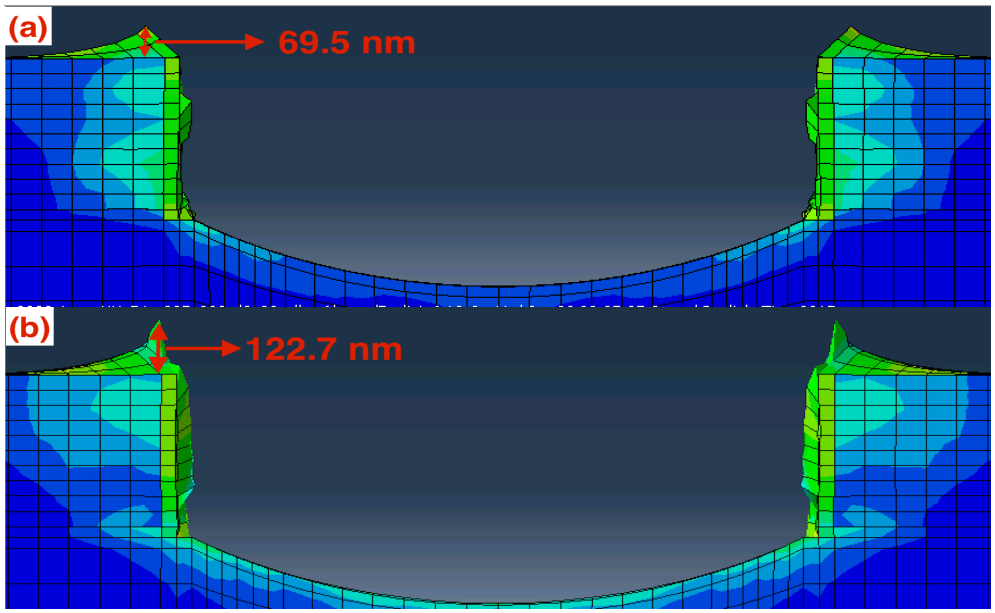

Fig. 4.35 Side burr formation for (a) R60 rounded tool at cutting speed of 100 mm/min, rake angle of 10 degrees (b) R60 rounded tool at cutting speed of 300 mm/min, rake angle of -5 degrees

4.9 Summary

In this chapter, the simulation experiements for the enhanced micro-groove cutting model are designed, and the stress, temperature induced on the workpiece, cutting force experienced by the tool are studied. The goal is to study the importance of coupling the thermal and mechanical aspects, the effect of frictional heat, and the effects of tool edge geometry, tool rake angle, depth of cut, and cutting speed on the outcomes of the process performance. The model is validated using side burr height and deformed chip thickness measurements obtained from the cutting experiments and simulation modeling, and the errors are calculated to be lower than 6.7% and 3.3%, respectively. In addition, the chip contact length increases as increase depth of cut increases. The highest stress appears at the primary shear zone while the highest strains are present in the secondary shear zone. The high temperature zone is found to be at the secondary shear zone as well by the tool-chip interface. Besides, the chip thickness and side bur height increase with increase in depth of cut.

A coupled thermo-mechanical model that also includes friction heat is found to be important for the prediction of microgroove machining performance. Decoupling the two aspects causes an overprediction of the temperature, cutting force, and von mises stress. Disabling the friction heat in the FEA model results in a larger drop in cutting force with an increase in cutting speed, underpredicts the maximum temperature and overpredicts the cutting force with rounded tool cutting edge. The model underpredicts the maximum temperature and overpredicts the cutting force with low rake angle. The rounded tool results in a higher maximum temperature and a larger cutting force in comparison to the sharp tools. Decrease in tool rake angle increases the maximum temperature and cutting force. The maximum von mises stress is not influenced significantly by these three parameters, i.e. cutting speed, rake angle, and edge radius.

Considering temperature and cutting force as responses, the tools with sharp cutting edge and rake angle of 10^0 result in the best machining performance comparing to other tool conditions studied. The side burr height is affected by the cutting condition chosen, and the tool with sharp edge, cutting speed of 300 mm/min, and rake angle of 10 degrees produces side burr height almost twice as small as with R60 rounded edge, cutting speed of 100 mm/min, and rake angle of -5 degrees, respectively.

Chapter 5

Conclusions and Recommendations

5.1 Overview of Thesis

The focus of the thesis was to enhance the 3D Finite Element (FE) model for micro-groove cutting of steel with CBN tool by including the frictional heat. The simulation results were validated by comparing them with the experimental results, and the importance of coupling the thermal and mechanical effects as well as including the friction heat was justified. The effects of various process parameters on the machining performance were also studied. The conclusions drawn from the thesis are listed below.

5.2 Conclusions

5.2.1 Heat Generation Model

1) The fully thermo-mechanical coupling model was used to couple the thermal and stress effects. The thermo-mechanical coupling was achieved by exchanging the temperature and stress data between the heat generation and flow stress equations;
2) The friction heat was included in the model by incorporating the friction heat equation into the first law of thermodynamic equation. By studying the in-depth mechanics of the tool-chip behavior, the friction heat fraction was set to be 0.9 and tool-workpiece equivalent friction

heat conversion factor was set to be 0.5. The inelastic heat fraction was chosen to be 0.8;

3) The frictional behavior at the tool-chip interface was simulated by including both normal and frictional shear stresses in the tool-chip contact model, and assigning the contacting surfaces between the tool and workpiece;
4) In order to avoid the meshing error caused by the rounded edge of the tool, the rounded surface of the tool was repartitioned into different sections.

5.2.2 Model Validation and Simulation Results

1) The simulation experiments were organized into three phases such as model simulation validation, thermo-mechanical coupling and friction heat effect studies, and process parameter effect study.
2) The simulation results obtained after the process reached steady state were used for model validation and analysis. The steady-state condition was assumed to reach when the tool-chip contact length remained unchanged. For the cutting conditions with 300 mm/min cutting speed, the cutting process reached steady state between 0.46 ms and 0.51 ms, while for cutting speed of 100 mm/min, the steady state was reached between 1.40 ms and 1.55 ms.
3) Model validation was achieved by comparing the cross-sectional cut image, side burr height, and deformed chip thickness values obtained from the enhanced model with the experimental results for two different depths of cut - 500nm and 960nm, and cutting speeds – 100 mm/min and 300 mm/min. The groove formations obtained from the simulation matched well with the ones collected from the experiment earlier by Raghavendra [1]. The prediction errors were within 6.7% for side burr height measurements and 3.3% for deformed chip thickness

measurements. For depth of cut 500 nm and cutting speed 300 mm/min, the error percentages for side burr height and chip thickness were more than 15%.

4) The enhanced model was used to study the process mechanics of micro-groove cutting during the steady-state period cutting that included surface and sub-surface stress analysis, temperature distributions, cutting force predictions in the direction of cut. The simulation was performed for two different cutting speeds – 100 and 300 mm/min, two different rake angles – 10^{o} and -5^{o} and two different edge radii – 0 nm and 60 nm, respectively.

5) Considering the frictional heat in the enhanced model was vital for the machining performance prediction. Specifically,

- Disabling the friction heat in the FE model resulted in lower maximum temperature and smaller high temperature band in the secondary zone.
- The steady-state cutting force and maximum von mises stress predicted by the friction heat-disabled model became higher if the friction heat was disabled.
- Disabling the friction underpredicted the maximum temperature by 16.08% on average, overpredicted the steady-state cutting force by 11.35% on average, and overpredicted the maximam von mises stress by 0.65% on average.
- The chip thickness and side burr height predictions from the enhanced model that included friction heat were improved in comparison to Raghavendra's model [1], with 8.5% lower percentage error in chip chickness and 4.5% lower percentage error in side burr height.

6) Coupling the thermal and mechanical effects was important for the cutting performance prediction. Specifically,

- The maximum temperature induced in the chip obtained from the decoupled model is

higher than the maximum temperature obtained from the coupled model.

- The maximum von mises stress and steady-state cutting force became higher when the thermal effect was decoupled with the mechanical effect in the model.
- Decoupling thermal and mechanical effects would overpredict the maximum temperature by 35% on average, the steady-state cutting force by 32% on average, and maximum von mises stress by 28% on average.

7) Different cutting speed, rake angle, and tool cutting edge resulted in different machining performance. Specifically,

- For a higher cutting speed, high temperature zone penetrated deeper into the chip and the cutting tool took shorter time to reach the steady state (0.46 ms) in compasion to the tool that moved slower (1.3 ms). The distributions of the von mises stress for the two cutting speeds were similar to each other.
- The high temperature zone in the secondary zone increased with the decrease in tool rake angle. The tool at rake angle of -5^0 experienced a larger cutting force during the steady state condition due to more supporting matrial compared to the tool at 10^o rake angle. The high stress area moved towards the tool tip and penetrated deeper into the workpiece as the tool rake angle became smaller. The chip shape was found to be less curly with decrease in the rake angle, resulting in a larger tool-chip contacting area for the smaller tool rake angle.
- The rounded tool produced more supporting area between the rounded cut tip and the workpiece as compared to the sharp tool. Thus, for the rounded tool, the high stress area in the primary zone was larger comparing to the sharp tool. The tool with sharp cutting edge experienced a lower cutting force during the steady state period than the tool with

rounded edge. The peak in cutting force before reaching the steady-state period for the rounded tool was due to the bluntness of the tool.

- Considering the temperature and cutting force, the tool with sharp cutting edge and rake angle of 10^0 resulted in the best machining performance among all conditions studied.
- An increase in cutting speed, a decrease in tool rake angle, and an increase in tool edge radius caused an increase in the maximum temperature in the chip. Also, an decrease in cutting speed, a decrease in tool rake angle, and an increase in tool edge radius caused an increase in the steady-state cutting force experienced by the tool. The change in tool rake angle and tool edge radius had significant effect on the change in maximum temperature and steady-state cutting force.
- The side burr height was affected by the cutting condition chosen. The tool with sharp edge, cutting speed of 300 mm/min, and rake angle of 10 degrees produced side burr height twice as small as with R60 rounded edge, cutting speed of 100 mm/min, and rake angle of -5 degrees, respectively.

5.3 Recommendations

The work done in this thesis resulted in an enhanced FEA model for the micro-groove cutting process that is capable of fully coupling the thermal and mechanical aspects and taking frictional heat into consideration. Also, the model is able to generate side burr and chip formations and predict von mises stress, temperature on the workpiece, and the cutting force experienced by the tool. However, there are improvements that could be done to refine the model.

(1) The model developed in this research assumes a discrete, perfectly rigid tool based on shell elements. In other words, deformation is confined to only the workpiece during the micro-groove cutting process. The purpose is to make the simulations run in a computationally effective manner and yield quicker results. However, in order to accurately predict the tool-chip interaction and tool wear, a deformable 3D cutting edge model assigned with mechanical and thermal properties needs to be developed. Thus, the convective heat transfer between the tool and workpiece needs to be considered in the model [14, 54, 81].

(2) Different tool shape geometries should be studied, more specifically varying the clearance and flank faces. This study would provide a deeper understanding of tool geometry-related burr formation and reduction analysis [39, 40].

(3) The plastically deformable workpiece material in the current model is treated as isotropic and homogenous. This is suitable because the workpiece material consists of fine-grained pure steel. However, many other desirable workpiece materials are heterogeneous and have grain sizes large enough for the tool to only be cutting through one grain at a time. Additionally, the crystalline orientation of materials that makes up individual grains can vary, which can result in different flow stress values depending on the direction of material deformation. Therefore, useful additions to the model would be explicit handing of grain structure, implementation of different material properties for different gains, and the ability to implement anisotropic yielding within a grain when necessary. [42-44, 85]

References

[1] Raghavendra R. H., 2012, “Development of a Meso-Scale CBN Flexible Cutting Tool for Micro-Groove Machining of Stainless Steel”, Thesis Mechanical Engineering in the Graduate College of the University of Illinois at Urbana-Champaign

[2] Bourne Keith, 2010, " Development of a High Speed High Precision Micro-Groove Cutting Process", PhD Thesis, University of Illinois, Urbana Champaign

[3] Strenhowski, J.S., and Carroll III, J.T., 1985, “A Finite Element Model of Orthogonal Metal Cutting”, Journal of Engineering for Industry, 107, pp. 349- 354

[4] Marusich, T.D., and Ortiz, M., 1995, “Modelling and Simulation of High-Speed Machining”, International Journal for Numerical Methods in Engineering, 38(21), pp. 3675-3694.

[5] Bourne KA, Kapoor SG, DeVor RE. Finite Element-Based Study of the Mechanics of Microgroove Cutting. ASME. J. Manuf. Sci. Eng.2013;135(3)

[6] Subbiah, S., and Melkote, S.N., 2007, “Evidence of ductile tearing ahead of the cutting tool and modeling the energy consumed in material separation in micro- cutting”, Journal of Engineering Materials and Technology, 129, pp. 321-331.

[7] Park, I.W., and Dornfeld D.A., 2000, “A study of burr formation processes using the finite element method: Part I”, Journal of Mechanical Engineering Materials and Technology, 122, pp. 221-228.

[8] Marusich, T.D., Usui, S., Ma, J., and Stephenson, D.A., 2008, “Finite element modeling of drilling processes with solid and indexable tooling in metals and stack- ups”, Third Wave Systems, Inc., http://www.thirdwavesys.com/news/published_papers.htm, pp. 1-7.

[9] Barge, M., Hamdi, H., Rech, J., and Bergheau, J.-M., 2005, “Numerical modeling of orthogonal cutting: influence of numerical parameters”, Journal of Materials Possessing Technology, 164-165, pp. 1148-1153.

[10] Akarca, S.S., Song, X., Altenhof, W.J., and Alpas, A.T., 2008, “Deformation behavior of aluminum during machining: modeling by Eulerian and smoothed-particle hydrodynamics methods”, Part L: Journal of Design and Applications, 222, pp. 209-221.

[11] Mabrouki T., Rigal J.-F., 2006, "A contribution to a qualitative understanding of thermo-mechanical effects during chip formation in hard turning", Journal of Materials Processing Technology, Vol. 176, Issues 1–3, pp. 214–221

[12] Akbar, F., Mativenga, P.T., 2010, “An experimental and coupled thermo-mechanical finite element study of heat partition effects in machining”, International Journal of Advanced Manufacturing Technology, Vol 46, n 5-8, pp 75-91

[13] Llanos, I.. "Finite element modeling of oblique machining using an arbitrary Lagrangian-Eulerian formulation." Machining science and technology 13.3 (2009):385-406.

[14] Sulaiman, Shamsuddin, Mohd K.A.Ariffin, and A.Roshan. "Finite Element Modeling of the Effect of Tool Rake Angle on Cutting Force and Tool Temperature during High Speed Machining of AISI 1045 Steel." Advanced materials research 939(2014):194-200.

[15] Kopalinsky, E.M., and Oxley P.L.B., 1984, “Size Effects in Metal Removal Processes”, Proceedings of the 3rd Conference on Mechanical Properties of Materials at High Rates of Strain, pp. 389-396.

[16] Dassault Systèmes Simulia Corp., 2013, “Abaqus 6.13 Analysis User’s Manual”.

[17] Chandrakanth Shet, and Xiaomin Deng, 2000, “Finite element analysis of the orthogonal metal cutting process”, Journal of Materials Processing Technology, Vol. 105, Issues 1-2, pp. 95-109

[18] Guoqin Shi, Xiaomin Deng, and Chandrakanth Shet, 2002, “A finite element study of the effect of friction in orthogonal metal cutting”, Finite Elements in Analysis and Design, Vol. 38, Issues 9, pp. 863–883

[19] Hibbit, Karlsson and Sorenson Inc., 2003, ABAQUS Analysis User’s Manual, Version 6.4

[20] Johnson, W.K., Cook, R., 1983, A Constitutive Model and Data for Metals Subjected to Large Strains, High Strain Rates and High Temperatures. Proc. 7th Inter. Symp. on Ballistics, pp.541-547.

[21] Ng, E., El-Wardany, T.I., Dumitrescu, M., and Elbestawi, M.A., 2002, "Physics Based Simulation of High Speed Machining" Proceedings of the 5th CIRP International Workshop on Modeling of Machining Operations, pp. 1 - 19.

[22] Ng EG, Aspinwall DK (2002) Modelling of hard part machining. J Mater Process Technol 127:222–229. doi:10.1016/S0924-0136 (02)00146-2

[23] Shih AJ (1995) Finite element simulation of orthogonal metal cutting. J Eng Ind 11:84–93. doi:10.1115/1.2803283

[24] Mirza, M.S., Barton, D.C., Church, P., 1996. "The effect of stress triaxiality and strain-rate on the fracture characteristics of ductile materials." J. Materials Sci. 31, 453–46

[25] Yingbin Bao, Tomasz Wierzbicki, 2005, "On the cut-off value of negative triaxiality for fracture", Engineering Fracture Mechanics 72 (2005) 1049–1069

[26] Akbar, F.. "An evaluation of heat partition in the high-speed turning of AISI/SAE 4140 steel with uncoated and TiN-coated tools." Proceedings of the Institution of Mechanical Engineers. Part B, Journal of engineering manufacture 222.7 (2008):759-771.

[27] M.B. Da Silva, J. Wallbank, 1999, " Cutting temperature: prediction and measurement methods-a review ", J. Mater. Process. Technol. 88 195–202

[28] Wan S., Martin L. D., Shawn J. C.,and David T. R ., 1999, “Elastic moduli, strength, and fracture initiation at sharp notches in etched single crystal silicon microstructures”, Journal of Applied Physics, vol. 85(7), 3519

[29] “Why Use FEA.” http://www.feacomp.com/why-use-fea. Web

[30] Ma, Jianfeng. "3D numerical investigation of the performance of microgroove textured cutting tool in dry machining of Ti-6Al-4V." The international journal of advanced manufacturing technology (2015)

[31] Waldorf, D.J., DeVor, R.E., and Kapoor, S.G., 1998, “A slip-line field for ploughing during orthogonal cutting”, Journal of Manufacturing Science and Engineering, 120, pp. 693-699.

[32] Liu, X., DeVor, R.E., and Kapoor, S.G., 2006, “An analytical model for the prediction of minimum chip thickness in micromachining”, Journal of Manufacturing Science and Engineering, 128(2), pp. 474-491.

[33] Vogler, M.P., DeVor, R.E., and Kapoor, S.G., 2003, “Microstructure-level force prediction model for micro-milling of multi-phase materials”, Journal of Manufacturing Science and Engineering, 125, pp. 202-209.

[34] Zhang, Z.G., Fang, F.Z., Hu, X.T., and Sun, C.K., 2009, "Molecular dynamics study on various nanometric cutting boundary conditions", Journal of Vacuum Science and Technology B, 27(3), pp. 1355-1360.

[35] Zhu, P., Hu, Y., Ma, T., and Wang, H., 2010, "Study of AFM-based nanometric cutting process using molecular dynamics" Applied Surface Science, 256, pp. 7160-7165.

[36] Komanduri, R., Chandrasekaran, N., and Raff, L.M., 2000, “M.D. simulation of nanometric cutting of single crystal aluminum – effect of crystal orientation and direction of cutting”, 240(1-2), pp. 113-143.

[37] Shih, A.J., 1996, “Finite element analysis of the rake angle effects in orthogonal metal cutting”, International Journal of Mechanical Sciences, 38(1), pp. 1-17.

[38] Marusich, T.D., 2001, "Effects of friction and cutting speed on cutting force", Proceedings of IMECE (ASME), MED-23313, pp. 1 – 9.

[39] Liu, K., Shreyes, N., and Melkote, N., 2007, "Finite element analysis of the influence of tool edge radius on size effect in orthogonal micro-cutting processes", International Journal of Mechanical Sciences, 49, pp. 650-660.

[40] Subbiah, S., and Melkote, S.N., 2008, "Effect of finite edge radius on ductile fracture ahead of the cutting tool edge in micro-cutting of Al 2024-T3", Material Science and Engineering A, 474, pp. 283 – 300.

[41] Liu, K., and Melkote, S.N., 2006, "Material strengthening mechanisms and their contribution of size effect in micro-cutting", Journal of Manufacturing Science and Engineering", 128, pp. 730-738.

[42] Chuzhoy, L., DeVor, R.E., Kapoor, S.G., and Bammann, D.J., 2002, "Microstructure-level modeling of ductile iron machining", Journal of Manufacturing Science and Engineering, 124, pp. 162-169.

[43] Chuzhoy, L, DeVor, R.E., Kapoor, S.G., Beaudoin, A.J., and Dammann, D.J., 2003, "Machining simulations of ductile iron and its constituents, Part I: estimation of material model parameters and their validation", Journal of Manufacturing Science and Engineering, 125, pp. 181-191.

[44] Chuzhoy, L, DeVor, R.E., and Kapoor, S.G., 2003, "Machining simulations of ductile iron and its constituents, Part 2: numerical simulation and experimental

validation of machining", Journal of Manufacturing Science and Engineering, 125, pp. 192-201.

[45] Marusich, T.D., Brand, C.D., and Thiele, J.D., 2002, "A methodology for simulaton of chip breakage in turning processes using an orthogonal finite element model", Proceedings of the 5th CIRP International Workshop on Modeling of Machining Operations, pp. 139-148.

[46] Marusich, T.D., and Askari, E., 2001, "modeling residual stress and workpiece quality in machined surface", Third Wave Systems, Inc., http://www.thirdwavesys.com/news/published_papers.htm, pp. 1-5.

[47] Guo, Y.B., and Dornfeld, D.A., 2000, "Finite element modeling of burr formation process in drilling 304 stainless steel", Journal of Manufacturing Science and Engineering, 122, pp. 612-619.

[48] Min, S., Dornfeld, D.A, Kim, J., and Shyu B., 2001, "Finite element modeling of burr formation in metal cutting", Machining Science and Technology, 5(3), pp. 307-322.

[49] Sartkulvanich, P., Sahlan, H., and Altan, T., 2007, "A finite element analysis of burr formation in face milling of a cast aluminum alloy", Machining Science and Technology, 11, pp. 157-181.

[50] Third Wave Systems, Inc., 2010, http://www.thirdwavesys.com.

[51] Scientific Forming Technologies Corporation, 2010, "DEFORM",

http://www.deform.com/.

[52] Kishawy, H.A.. "Arbitrary Lagrangian Eulerian analysis on cutting with a honed tool." Proceedings of the Institution of Mechanical Engineers. Part B, Journal of engineering manufacture 222.2 (2008):155-162.

[53] Sulaiman, S.. "Finite element modeling of the effect of tool rake angle on cutting force and tool temperature during high speed machining of AISI 1045 steel." Advances in Materials and Processing Technologies XVI. Trans Tech Publications, (2014). :194-200.

[54] Umbrello, D.. "On the evaluation of the global heat transfer coefficient in cutting." International journal of machine tools & manufacture 47.11 (2007):1738-1743.

[55] Arrazola, P.J.. "A new approach for the friction identification during machining through the use of finite element modeling." Internatonal journal of machine tools & manufacture 48.2 (2008):173-183.

[56] M.E.S. Abdelmonein, R.F. Scrutton, Tool edge roundness and stable build-up formation in finish machining, Journal of Engineering for Industry 96 (1974) 1258–1267.

[57] E. Merchant, Basic mechanics of the metal-cutting process, Transaction of the ASME, Journal of Applied Mechanics 66 (1944) 168–175.

[58] P. Albrecht, New developments in the theory of the metal-cutting process, Part 1, Journal of Engineering for Industry (1960) 348–358.

[59] Alkbar, F., Mativenga, P.T., and Sheikh, M.A., 2010, "An experimental and coupled thermo-mechanical finite element study of heat partition effects in machining", International Journal of Advanced Manufacturing Technology, 46, pp. 491-507.

[60] Bacaria, J-L., Dalverny, O., and Caperaa, S., 2001, "A three-dimensional transient mumerical model of milling", Proceedings of the Institution of Mechanical Engineering, Part B: Journal of Engineering Manufacture, 215, pp. 2041-2975.

[61] Liu, X., DeVor, R.E., and Kapoor, S.G., 2006, "An analytical model for the prediction of minimum chip thickness in micromachining", Journal of Manufacturing Science and Engineering, 128(2), pp. 474-491.

[62] Ng EG, Aspinwall DK (2002) Modelling of hard part machining. J Mater Process Technol 127:222–229. doi:10.1016/S0924-0136 (02)00146-2

[63] Liu CR, Guo YB (2000) FEM analysis of residual stresses on the sequential machined surface. J Mech Sci 42:1069–1089. doi:10.1016/S0020-7403(99)00042-9 59.

[64] Shih AJ (1995) Finite element simulation of orthogonal metal cutting. J Eng Ind 11:84–93. doi:10.1115/1.2803283

[65] Reginaldo TC, Ng E-G, Elbestawi MA (2007) Tool wear when turning hardened AISI 4340 with coated PCBN tools using finishing cutting conditions. Int J Mach Tools Manuf 47:263–272. doi:10.1016/j.ijmachtools.2006.03.020

[66] Shi J, Liu CR (2005) On predicting softening effects in hard turned surfaces—part II: finite element modeling and verification. Trans ASME 127:484–491.

doi:10.1115/1.1843166

[67] Kai L, Melkote SN (2006) Material strengthening mechanisms and their contribution to size effect in micro-cutting. Trans ASME 128:730–738

[68] Shi J, Liu CR (2004) The influence of material models on finite element simulation of machining. J Manuf Sci Eng 126:849–857. doi:10.1115/1.1813473

[69] Ng, E.-G.. "Modelling of temperature and forces when orthogonally machining hardened steel." International journal of machine tools & manufacture 39.6 (1999):885-903.

[70] http://people.virginia.edu/~lz2n/mse209/Chapter19c.pdf

[71] Jones, William; March, Norman H. (1985). Theoretical Solid State Physics. Courier Dover Publications. ISBN 0-486-65016-2.

[72] https://en.wikipedia.org/wiki/Thermal_conductivity#Temperature

[73] Quinney, H, and G I I Taylor. "The Latent Energy Remaining in a Metal after Cold Working." Proceedings - Royal Society. Mathematical, physical and engineering sciences 143.A849 (1934): 307-326. Web.

[74] Mason, J J. "On the strain and strain rate dependence of the fraction of plastic work converted to heat: an experimental study using high speed infrared detectors and the Kolsky bar." Mechanics of materials 17.2 (1994): 135-45. Web.

[75] Pottier, T, et al. "Inelastic heat fraction estimation from two successive mechanical

and thermal analyses and full-field measurements." European journal of mechanics. A, Solids 38(2013):1-11. Web.

[76] Knysh, Paul, and Yannis P Korkolis. "Determination of the fraction of plastic work converted into heat in metals." Mechanics of materials 86(2015): 71-80. Web.

[77] Chen, Q, and D Y Y Li. "A computational study of frictional heating and energy conversion during sliding processes." Wear 259.7-12 (2005):1382-1391. Web.

[78] Li, D.Y.; Elalem, K.; Anderson, M.J.; Chiovelli, S. A micro-scale dynamical model for wear simulation, Wear 1999, 225, 380–386.

[79] Elalem, K.; Li, D.Y.; Anderson M.J.; Chiovelli, S. Modeling abrasive wear of homogeneous and heterogeneous materials. ASTM STP 1339, 2001, 90–104.

[80] A.J.R. Smith, J.A. Armarego, Temperature prediction in orthogonal cutting with a finite difference approach, Annals of CIRP, 1981.

[81] Augustine, Uzorh, and Nwufo Olisaemeka. "Thermal Aspect of Machining: Evaluation of Tool and Chip Temperature during Machining Process Using Numerical Method." The International Journal Of Engineering And Science (IJES) 2, no. 4 (2013): 66-79.

[82] Tay, A. O. 1974. USING THE FINITE ELEMENT METHOD TO DETERMINE TEMPERATURE DISTRIBUTIONS IN ORTHOGONAL MACHINING. Inst Mech Eng (Lond) Proc 188 (55): 627-638.

[82] Özel, Tugrul. 2006. The influence of friction models on finite element simulations of machining. International journal of machine tools & manufacture 46 (5): 518-530.2

[83] Arrazola, Pedro J, and Tugrul Özel. 2010. Investigations on the effects of friction modeling in finite element simulation of machining. International journal of mechanical sciences 52 (1): 31-42.

[84] N.N. Zorev, Inter-relationship between shear processes occurring along tool face and shear plane in metal cutting International Research in Production Engineering, ASME, New York, 1963. pp. 42–49.

[85] Kota, N., and Ozdoganlar, B., 2010, "Machining force and surface finish variation across grains during orthogonal micromachining of aluminum", 5th International Conference on MicroManufacturing, pp. 133-137.

[86] Özel, Tuğrul, and Taylan Altan. 2000. Determination of workpiece flow stress and friction at the chip–tool contact for high-speed cutting. International journal of machine tools & manufacture 40 (1): 133-152.

[87] Groover, Mikell P. 1996. Fundamentals of modern manufacturing: materials, processes, and systems. Upper Saddle River, N.J.: Prentice Hall, pp503-508.